THE UNIVERSITY
of LIVERPOOL

From complex metallic alloys to quasicrystals - Structure, epitaxy and properties

Thesis submitted in accordance with the requirements of
the University of Liverpool for the degree of Doctor in Philosophy

by

Joseph Parle

Contents

Acknowledgements

All of the experiments completed for this thesis would not have been possible without the help and support of the Quasicrystal group and the rest of the Surface Science Research Centre. All of the work has been a team effort. It has been a fantastic experience learning from such talented and dedicated scientists. I would like to thank Prof. Ronan McGrath for the opportunity to do this PhD, and for his continued help and guidance. A special thanks to Dr. Joe Smerdon for all his help and expertise, and for teaching me the skills of surface science with exceptional talent and patience, especially the 'dark art' of getting a Scanning Tunnelling Microscope to work properly. The long hours would not have been so enjoyable without the rest of the Quasicrystal group, Dr. Lisa Wearing, Pete Nugent, Kirsty Young and Dr. Hemraj Sharma. It has been great to work with Dr Vin Dhanak, whose help with XPS has been greatly appreciated. I would also like to thank the rest of the Surface Science Research Centre, especially Dr. Sam Haq, without whom I'm sure the whole centre would fall apart, John Ledward for fixing everything that ever broke.

I must also thank the scientists I have worked with on external collaborations, Dr. Tim Noakes of STFC Daresbury Laboratory for all his expertise with MEIS, Dr. MG Barthes-Labrousse and Micheline ward, of Universit Paris Sud Orsay, and Dr. Alessandra Beni of EMPA Switzerland for all their help with XPS and oxidation experiments. The UK Engineering and Physical Sciences Research Council (EPSRC) and the European Union Network of Excellence Complex metallic alloys are thanked for financial support.

Thanks again to everybody!

Abstract

The aim of this study is to explore the fundamental properties of quasicrystals and complex metallic alloys, using various surface science techniques to investigate both the clean surfaces and the growth of thin films on these surfaces.

Low-energy electron diffraction (LEED) and scanning tunneling microscopy (STM) are used to study the orthorhombic quasicrystal approximant Al_4(Cr, Fe) (Chapter 4). X-ray Photoemission Spectroscopy (XPS) is used simultaneously with STM to study the oxidation of the (1 0 0) surface of Al_4(Cr, Fe) (Chapter 5). Data indicates that the initial oxidation is highly ordered. STM data shows that oxygen preferentially adsorbs onto the surface of terraces, and the XPS data shows that only Al is oxidised. The combination of techniques helps to relate the STM images to the structural model.

The surface oxidation of the Al_4(Cr, Fe) approximant is studied in a detailed quantitative manner, using XPS to measure differences in oxidation rates between different faces of the crystal (Chapter 6). The structural model reveals layers of high chromium content in the (001) plane, and its effectiveness as an oxidation barrier is investigated.

The formation of a Bi monolayer deposited on the five-fold surface of i-$Al_{70}Pd_{21}Mn_9$, has been studied by STM (Chapter 7). The growth of 5 atom pentagons, with edge length 4.9 ± 0.2 Å, is observed. The pentagons have a common orientation leading to a film with five-fold symmetry. By inspection of images where both the underlying surface and the Bi atoms are resolved, the pentagonal clusters are found to nucleate on pseudo-Mackay clusters truncated such that a Mn atom lies centrally in the surface plane. In this way the nucleation and growth mechanism of a single element quasicrystalline monolayer are revealed.

The room temperature thin film growth of Fe deposited on the 5-fold surface of i-$Al_{70}Pd_{21}Mn_9$ has been studied using medium energy ion scattering (MEIS) (Chapter 8). Previous Auger electron spectroscopy (AES) results show contradictory results, one study rules out intermixing [1], while another finds that Fe atoms do intermix with substrate [2]. The MEIS technique reveals both structural information and elemental composition as a function of depth, allowing the question of intermixing to be answered.

Chapter 1

Understanding Quasicrystals

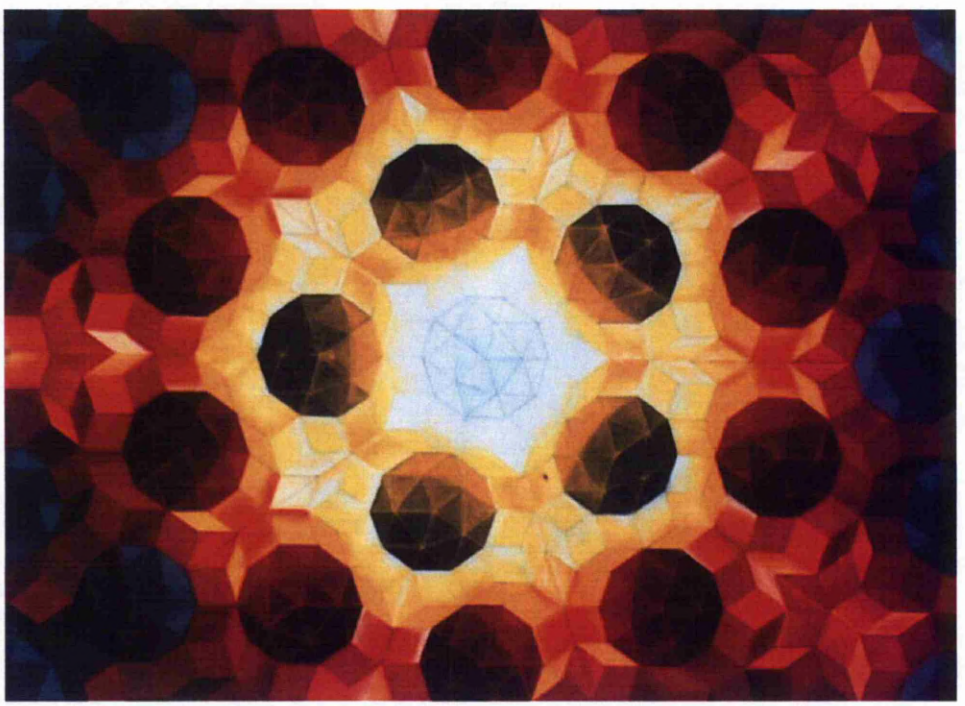

Figure 1.1: Penrose tiling inspired artwork, by Kachelstruktur

In 1982 Danny Shechtman and co-workers discovered an unusual diffraction pattern (Fig. 1.2) while studying fast quenched aluminium manganese alloys. It was over two years before a paper was published [3], due to their reluctance to unleash a shock wave into the world of crystallography, without

first double checking they were right. Their discovery was a 10-fold diffraction pattern, not allowed under the accepted rules of crystal structure. By the end of the decade, their discovery opened up a whole new field in material science, and led to the redefinition of the word crystal itself [4].

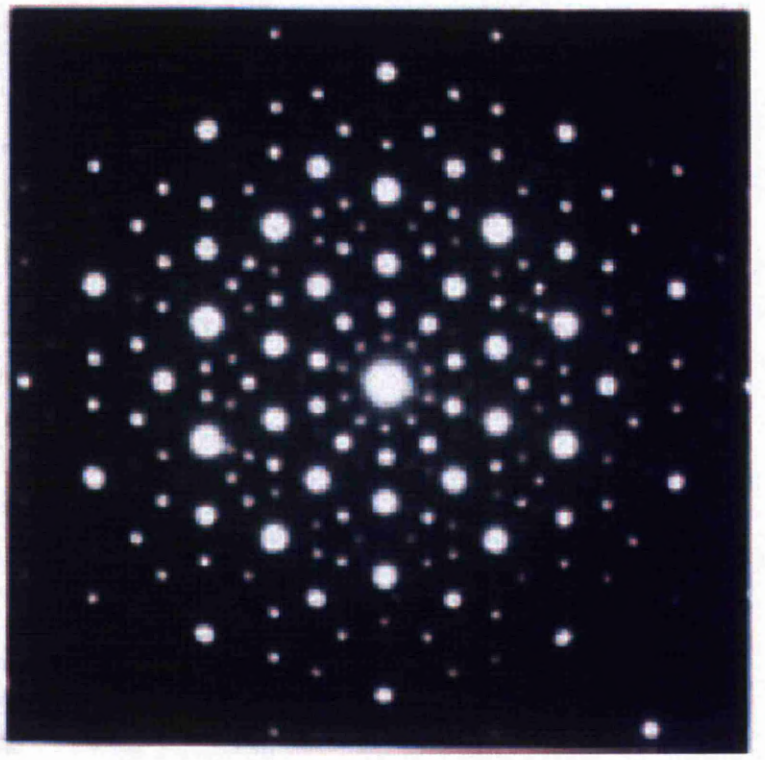

Figure 1.2: The 10-fold diffraction pattern discovered by Shechtman [3]

1.1 Categorizing Solids

For many years it has been understood that a solid is an arrangement of atoms held together by the attractive and repulsive interatomic forces. The atomic separation is such that the atoms try to sit at the minimum of potential (Fig. 1.3). In a solid, the thermal energy allows the atoms to vibrate about this mean position in a similar fashion to simple harmonic motion. The bulk retains the same overall structure and mean interatomic separation. Except for some thermal expansion, due to the asymmetry of the potential curve, the atoms are effectively locked in place. Consider a monatomic solid being formed from a liquid. The final geometric arrangement depends on various factors including the type(s) of atoms involved, type of bonding, etc. However, altering the rate of cooling can result in the same material adopting a totally different structure.

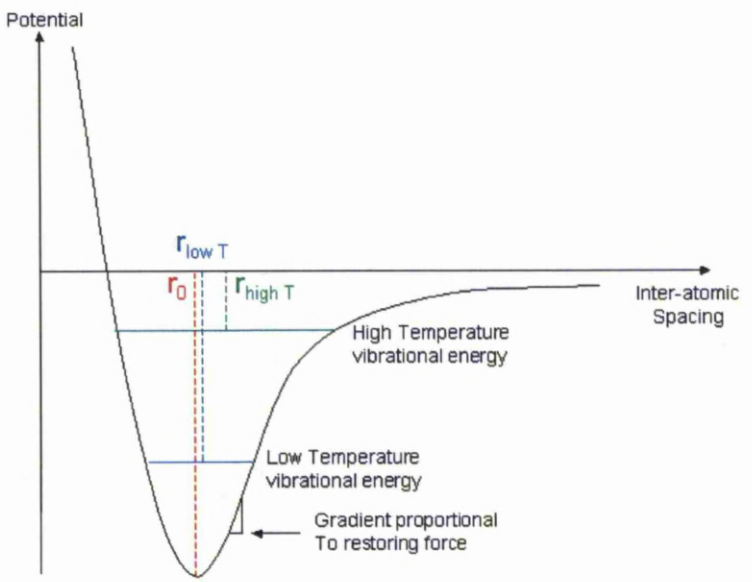

Figure 1.3: The interatomic potential energy curve, known as the Lennard-Jones potential.

Each atom would like to be at the exact optimum distance to its nearest neighbour. However, to move there requires both time and energy. This must happen before energy is lost as the material cools down into a solid, freezing the atoms into position. Depending on the rate of energy loss, as the material moves below the melting point, there can be only two broad

outcomes to this process.

Firstly, if the solid is formed in such a way that the individual atoms do not have time to move into optimum positions, the individual atoms are frozen into place at random locations (Fig. 1.4). The average interatomic separation will be near to the optimum, but no two atoms will be exactly the same distance apart or have the same number of nearest neighbours. No repeated patterns can be seen in the structure, as there is no long-range and minimal short-range order. This type of disordered solid is known as amorphous, or more commonly a glass.

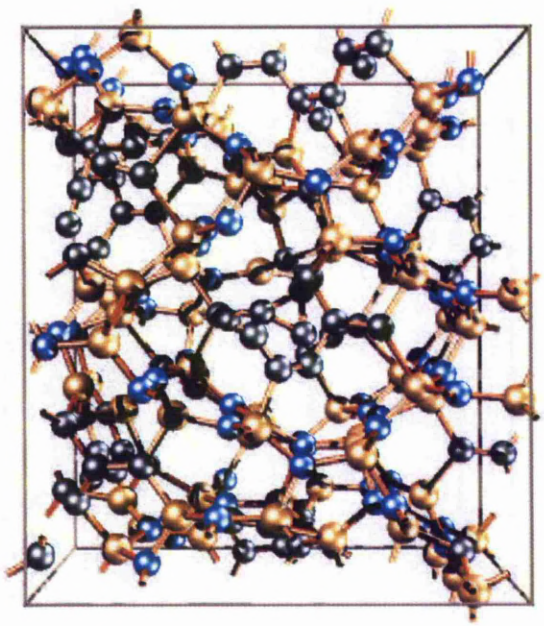

Figure 1.4: An example of an amorphous structure, with atoms frozen at random positions. SiCN is shown here, image from www.bccms.uni-bremen.de

Secondly, if the conditions are right then the atoms can move into their optimum positions. To be in the most energy efficient arrangement, they need to release the most lattice potential energy. This is done by a combination of maximising the number of nearest neighbour interactions, and keeping most of the atomic separations at their optimum distance, so they sit at or near the potential energy minimum (Fig. 1.3). In effect atoms try to fill space with the minimum volume of empty space. Due to their 'spherical' nature, it is impossible to fill all space completely, as it would be with cubes. But there are several structural solutions to this problem. Under the same

thermal conditions, this happens in an identical way throughout the material, leaving a highly ordered structure with repeated geometric patterns. This type of material is known as a crystal. A crystalline structure has highly coherent atomic order.

1.2 Classic Crystallography

Consider the layer by layer growth of a solid. In the first layer formed the atoms align in a 2-d plane arranged like the squares on a chess board. The next layer has a choice of positions. The atoms can sit exactly above the atoms in the first layer, arranged like the segments in a Rubik's cube®, forming a simple cubic structure. This whole structure can be completely described by defining a unit cell (the smallest repeated volume of atoms (Fig. 1.5)) and a translation operation. By defining a lattice point as an origin in a unit cell, a translation of the form given in Equation 1.1 gives the position of another lattice point. In this way a lattice framework can be constructed, in which every lattice point is the origin of an identical unit cell. In this way the structure is described by cubes which fill all space perfectly, but each with an identical amount of internal empty space. The exact proportion depends on how the atoms are packed within the unit cell.

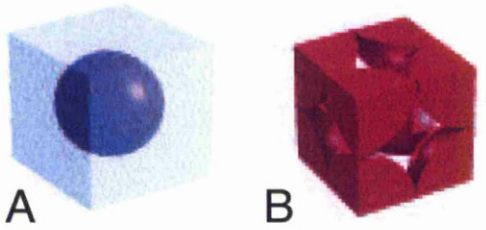

Figure 1.5: Two equivalent ways of defining the unit cell of a simple cubic crystal. **A** One atom at the centre. **B** 1/8 of an atom at each corner of a cube. Both ways give the same structure when the unit cell 'cubes' are stacked together.

The origin of the unit cell is arbitrary, but is chosen to give the most useful perspective. It contains the minimum number of atoms, for simplicity. The simple cubic structure can be chosen so that each corner contains one 1/8 of an atom. Overall this unit cell contains 2 atoms, one at the centre and, when the unit cells are assembled in a lattice, each corner point makes

up one atom from the 8 adjacent unit cells. Filling space in this way results in an atomic packing fraction of just 0.52 (48% empty space).

Different possible solutions can be acquired by considering where else the atoms could sit in subsequent layers. If rather than sitting directly on top of an atom, it can sit in the hollow between four atoms, creating a BCC (Body centered cubic) structure (Fig. 1.6), increasing the packing fraction to 0.68. Another possibility is to sit in the hollow between two atoms, creating an FCC (Face Centered Cubic) structure, increasing the packing fraction further still, to 0.74. A random packing (amorphous) gives a packing fraction of 0.64.

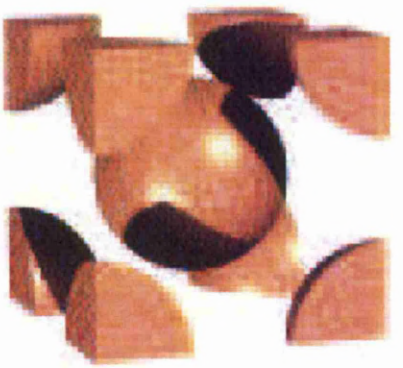

Figure 1.6: Unit cell for BCC (Body Centered Cubic)

Another possibility is to consider the first layer to form in a hexagonal pattern. The next layer forms with each atom sitting in the hollow between 3 atoms. However, there are twice as many hollows as there are atoms. If atoms in the first layer sit in position A, then position B in the second, this leaves hollows at position C. The third layer has two possibilities. They can sit at position A again, with the structure repeating A,B,A,B,A..., forming a HCP (Hexagonal Close Packed) structure (packing fraction = 0.74). The alternative is for the third layer to sit at position C, giving the stacking sequence is A,B,C,A,B,C... The final structure is in fact an FCC just rotated 45° in the x, y, and z axis.

By constructing lattices like this using mathematics, it is possible to hypothesize which atomic structures are possible. Auguste Bravais (1811-1863), a French physicist, pointed out, in 1845, that there are just 14 unique lattices in three dimensional crystalline systems (Fig. 1.7). It was internationally agreed that this was true, and they were named Bravais lattices in his honour. For nearly 140 years it was believed that these were the only possible

ordered structures in solids. This allowed a formal convention for describing crystal structure. The vectors within the unit cell can be used to define the whole lattice. The lattice points can be described by vectors relative to the origin of a unit cell. These lattice points are then repeated throughout the structure in integer multiples of the unit cell distance, described in Eq. 1.1.

$$\mathbf{R} = n_1\mathbf{a} + n_2\mathbf{b} + n_3\mathbf{c} \tag{1.1}$$

where each lattice point is given by position vector **R**, **a,b,c** are the primitive vectors, which describe the unit cell length and direction of each plane, and n_1,n_2,n_3 are integers.

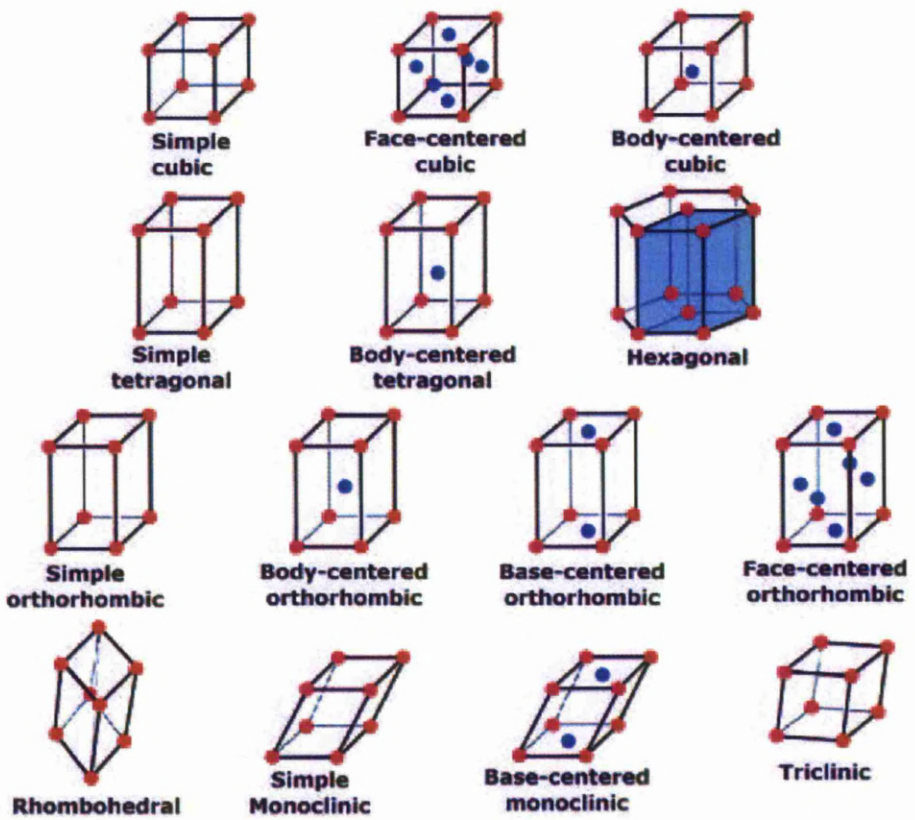

Figure 1.7: The 14 possible Bravais lattices. Image from www.seas.upenn.edu

Each lattice point then sits in an identical environment to the one it was copied from in the unit cell. The only other information required to construct a classical crystal is the *basis*. This is the number of atoms to be placed at each lattice point, usually one in the simplest cases, but it can be any number and type of atoms. Thus a crystal can be fully described with just the *lattice* and the *basis*. This method of lattice construction has inherent translational symmetry, long-range and short-range order.

1.3 Diffraction and Rotational symmetry

The proof for the Bravais lattices came later from x-ray diffraction. In 1912 Max Von Laue (1879-1960) designed the first successful experiment (Fig. 1.8 **A**). By using a wavelength comparable to interatomic spacing (1-3 Å), the x-rays reflect from each atom causing an interference pattern, a phenomenon already well known for visible light. The real space structure can then be calculated from the reciprocal space diffraction pattern (Fig. 1.8 **B**). By knowing the wavelength of the x-rays, it is possible deduce the distance between scattering centers, adding dimensions to the model.

All of the 14 Bravais lattices have either 2, 3, 4 or 6-fold rotational symmetry. This means that rotating a lattice by 180°, 120°, 90°, or 60° respectively would overlay the original identically, but no other angles are possible. This

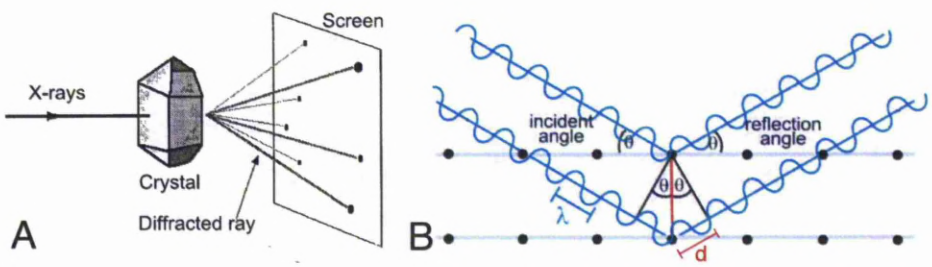

Figure 1.8: **A.** A collimated beam of monochromatic x-rays is fired at the sample. The diffraction pattern from a crystal has bright spots, corresponding to angles where constructive interference from planes of atoms occurs. Image from www.crystal.unito.it. **B.** Constructive interference from one plane of atoms. The angle between undiffracted x-ray beam and diffracted beam is 2θ. The orientation of each plane is given by this angle and the orientation of each spot. The inter-planar spacing is given by the Bragg Law ($n\lambda = 2d$ *Sin* θ). Image from www.microscopy.ethz.ch

also applies in reciprocal space - the diffraction pattern can be rotated to overlay itself in the same way, and has the same order rotational symmetry as the real space lattice. Therefore, diffraction patterns with any other order of rotational symmetry were not believed possible, hence the term forbidden symmetry.

For the next century, all materials tested fitted into this picture. They were either amorphous glasses with no diffraction pattern at all, or they were crystals with the expected rotational symmetries, which were all proven to belong to the 14 known Bravais lattices. This reinforced the view that all crystals must have long-range and short-range order, and translational symmetry, and therefore crystals must possess periodic order.

1.4 Forbidden Symmetry

Dan Shechtman, from Technion University in Jerusalem, was studying the structural phases of rapidly quenched Al-Mn alloys, at the National Bureau of standards in Washington D.C. On 8th April 1982, he discovered an electron diffraction pattern with 10-fold rotational symmetry (Fig. 1.9).

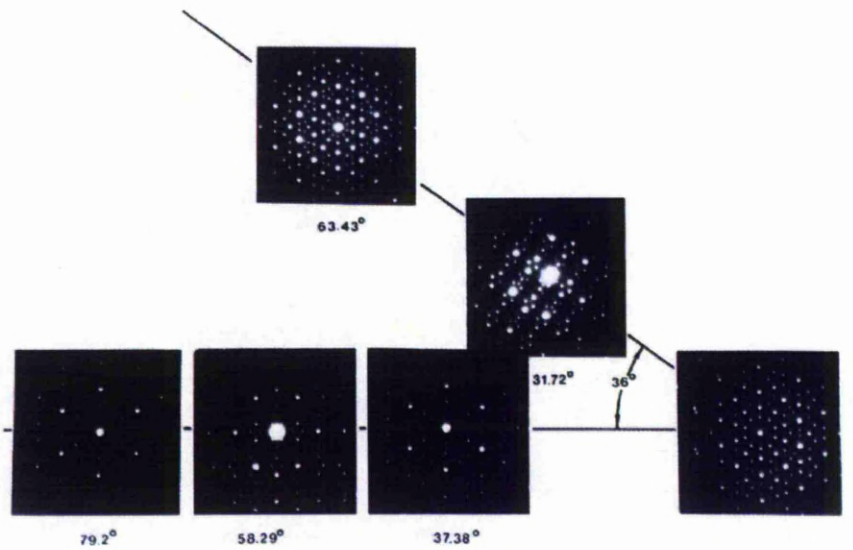

Figure 1.9: The original diffraction data from Shechtman's paper [3]. The single grain sample is rotated with respect to the incident beam revealing different axes of rotational symmetry.

It could not be a glass, as it showed sharp diffraction spots that could

only come from a well ordered atomic arrangement producing constructive interference. However, the 10-fold pattern did not fit the classical rules of crystallography. This forbidden symmetry meant it was not from a conventional lattice generated by translational symmetry. Further investigation revealed that, by rotating the crystal, planes with different rotational symmetries could be seen. The patterns obtained could not be indexed to any Bravais lattice. Shechtman deduced that it did in fact have icosahedral point group symmetry.

It was already known that Icosahedra are a common packing unit in inter-metallic crystals [5, 6], with a smaller transition element an the centre surrounded by 12 larger atoms making the corners of an icosahedron. An icosahedron (Fig. 1.10) has 20 faces of equilateral triangles. It has six fivefold axes of rotational symmetry, ten threefold axes, and fifteen twofold axes. If the specimen is rotated through the same angles as this icosahedral point group, the diffraction pattern observed had the same rotational symmetries at the same angles (Fig. 1.9). The opposite faces along axes of symmetry are inverted on an icosahedron, so looking at the 5-fold axis, the backward face is 180° out of phase. This makes the diffraction pattern look 10-fold, when it is actually two superimposed 5-fold patterns. The same applies to the 3-fold axis, which appears 6-fold. The 2-fold axis is symmetrical upon inversion, so this still appears 2-fold.

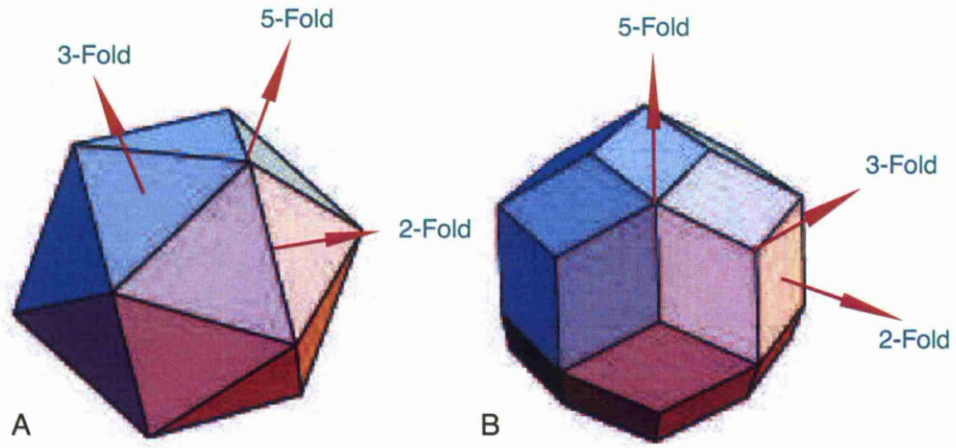

Figure 1.10: **A.** An icosahedron showing one of each rotational symmetry axis. **B.** Other polyhedra can have similar properties, such as this triacontahedron, with lozenge facets reminiscent of a Penrose P3 tiling.

Analysis of many liquid metals, metallic clusters and metallic glasses has

shown that local order is predominately tetrahedral. Tetrahedral packing is the densest known packing of spheres in Euclidean space and it is the most favourable in minimizing the Gibbs free energy. Five tetrahedra will fit almost perfectly around a common edge to form a pentagonal bi-pyramid and 20 tetrahedra can be put together sharing a common central vertex, with slight distortions, to form a regular icosahedron, Fig. 1.10. However, the icosahedron cannot be periodically packed to fill space, so an entire crystal showing icosahedral symmetry was thought to be impossible.

Data which breaks well established scientific rules is often met with ridicule, and always deep scrutiny. Crystals with apparent forbidden symmetry do occur as multiple twins [7]. Fig. 1.11 shows an example. The five classical crystalline domains arranged around the centre, would give a 5-fold diffraction pattern from the whole grain. To be sure that this was not the case for quasicrystals, Shechtman did three tests. Dark field images taken from any reflection revealed no twinning. Convergent beam diffraction, focused on any part of the grain, revealed all the reflections that were visible from the whole grain. X-ray diffraction patterns from a sample containing many grains, of various orientations, could not be indexed to any Bravais lattice, which should have been possible regardless of twinning. On the basis of these results Shechtman concluded that the phase he had discovered, what he named the icosahedral phase, did not consist of multiply twinned regular crystal structures, and did in fact have long-range orientational order and no translational symmetry. These results were published in Shechtman's paper [3], 12th November 1984, two years after the initial discovery.

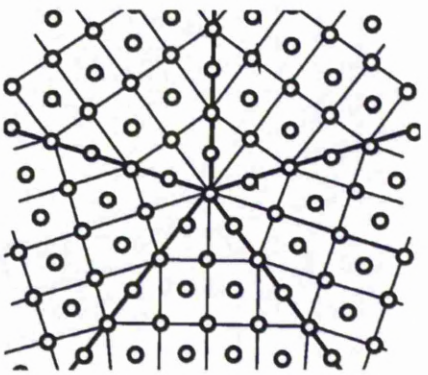

Figure 1.11: This tiling has fivefold symmetry about its centre, but is made from 5 periodic domains.

Shechtman suggested the icosahedral phase forms during rapid cooling of the melt by a first order transition, where the solid nucleates at a centre point

and grows out at the interface. The atomic rearrangements that occur at this interface results in the orientational order of the icosahedral phase. This phase differs from adjoining phases in entropy, and in composition. Melts with just 10-12 at.% Mn result in many isolated icosahedral grains separated by crystalline films of fcc Al. The growth of the icosahedral grains results in Al being rejected to the melt, and eventually the Mn deficiency limits the icosahedral growth, and results in the usual fcc structure associated with Al. Increasing the composition to 14 at.% Mn gives the ideal mixture to promote icosahedral growth. Only small amounts of fcc Al. occur at grain boundaries where icosahedral grains have grown to impingement. This is known as the icosahedral glass model, and seemed to fit initial diffraction patterns with relatively wide spots (as growing techniques improved, the pinpoint spots indicated far greater order than this, suggesting icosahedral symmetry exceeding the grain size.) Shechtman concludes that the icosahedral phase is a truly metastable phase which nucleates and grows for a range of cooling rates which are slow enough to permit its formation, but rapid enough to prevent crystallisation (e.g. to the stable Al_6Mn phase). Cooling rates of $10^5 \leftrightarrow 10^6 Ks^{-1}$ are used.

Despite his diligence, the results were denounced by many. The Nobel prize winning chemist, Linus Pauling (1901-1994), dismissed his findings as multiply twinned cubic crystals. However, as the results were successfully repeated worldwide, and new materials with forbidden symmetries were discovered, the existence of this type of material became indisputable. They were named 'quasicrystals', by Levine and Steinhardt [8], short for quasi periodic crystals.

In 1992, the International Union of Crystallography redefined a crystal as "any solid having an essentially discrete diffraction diagram" [4], to include quasicrystals. This shifted the definition of a crystal from real space to reciprocal space. Later determination of the structure of quasicrystals also revealed that the forbidden rotational symmetries are not strictly true in real space. The lack of translational symmetry, and the random nature of structural patterns, means that if the lattice is rotated in real space, it will not overlay the original identically (as is also the case for a Penrose tiling). However, the majority of lattice points will match up, giving the sharp diffraction spots. So, in effect, the definition of rotational symmetry is also shifted into reciprocal space, as these patterns will overlay exactly when rotated.

1.5 Aperiodic Order

1.5.1 Fibonacci Sequence

The diffraction patterns obtained prove that quasicrystals are highly ordered, yet their forbidden symmetries mean that they cannot possess periodic order. Therefore, they must possess aperiodic order. A simple example of aperiodic order is a 1 dimensional number sequence, called the Fibonacci sequence. It is named after the great mathematician Leonardo de Pisano Fibonacci (≈1170-1250), also famous for introducing decimal numbers to Europe in his book Liber Abaci. It is given by the rule 'the next term is given by the sum of the previous two terms', resulting in following sequence:

1
1
2
3
5
8
13
21
...

Another way of viewing this sequence is to use the terms L and S. If the same Fibonacci sequence is applied with the additional rules L→LS and S→L, the result is:

S
L
LS
LSL
LSLLS
LSLLSLSL
LSLLSLSLLSLLS
.....

The reason for this alternative form is that, by assigning the meanings L = long and S = short, this kind of Fibonacci sequence can be seen in quasicrystals as patterns of inter-planar spacings. The sequence follows a rigid set of rules and yet extends to infinity without ever repeating. However, any part of any term can be found in another term, an infinite number of times. This repetitive quality is also seen in the structural motifs of quasicrystals.

1.5.2 The Golden number

As the Fibonacci sequence progresses, the ratio of each term to the previous term approaches τ, the golden number, where $\tau = (1+\sqrt{5})/2) \approx \mathbf{1.618}$. The ratio of **L:S** in each term also approaches τ. This number, and the Fibonacci sequence are intricately connected to aperiodic order. It frequently appears in nature. Fig. 1.12 shows the pattern of spirals on a pine cone, with 8 spirals in one direction, and 13 in the other, following the terms of the Fibonacci sequence. Sunflower seeds are arranged in a similar fashion. The aperiodic order allows the most efficient packing of seeds, no matter how big the seed head grows. Many other plants follow similar patterns in the number of petals, leaves and spirals.

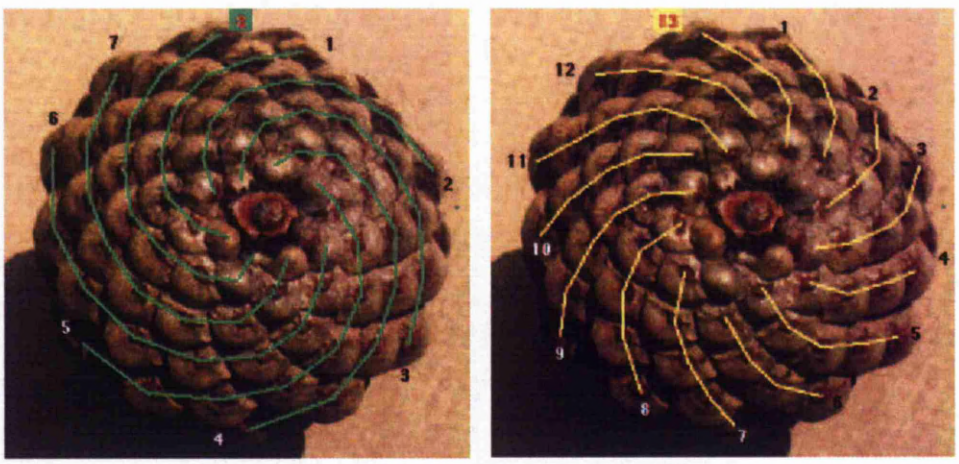

Figure 1.12: The same pine cone is highlighted in two different ways to show the spiral structure curving in opposite directions. The numbers of spirals in each direction form consecutive terms of the Fibonacci sequence.

This number appears so often in nature that it is considered to be the 'divine proportion'. It is frequently used by artists and architects to make aesthetically pleasing creations. The ancient Greeks used this divine ratio often, particularly in temple design. The ratio of the height of the Parthenon to the width is τ. The golden ratio appears frequently in fivefold symmetry; Fig. 1.13 shows some examples.

1.5.3 Cut and Project

Another method to obtain aperiodic order is the cut and project method. Projecting a subset of a periodic higher dimensional lattice into a lower di-

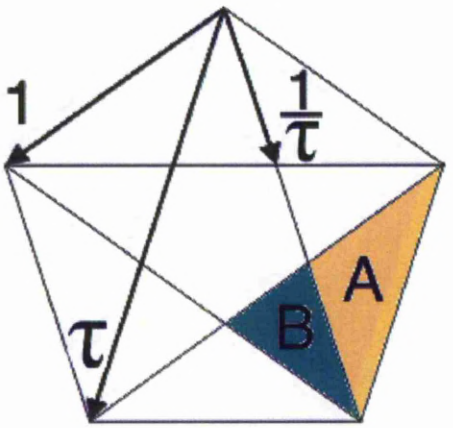

Figure 1.13: Fivefold symmetry is closely related to τ. The ratio of the side of a regular pentagon to its diagonal is τ. The diagonals also intersect each other at a point which splits them in the golden ratio. The ratio of areas **A/B** is also τ.

mensional subspace can give aperiodic order. Consider the 1-D case, Fig. 1.14. Starting with a periodic 2-d lattice, take a slice through the plane with the line **y=mx+c**, which intersects one point, and represents parallel space **E"**. Consider the strip, obtained by shifting the unit square W^2 along **E"**. By projecting the subset of points within the strip orthogonally onto **E"**, we obtain a sequence of long (**L**) and short (**S**) segments. If the gradient **m** is an irrational angle then the sequence is aperiodic. If m=arctan τ, then the resulting sequence is the Fibonacci sequence. It is worth noting that the length ratio of **L/S** is τ, and as the sequence progresses, the number of occurrences of **L** and **S** also has the ratio of τ.

Using this method, a 3 dimensional icosahedral quasicrystal can be considered as a three dimensional projection of a six-dimensional hyper-cubic lattice. If the slope is chosen to be a rational number, then the resulting sequence is periodic. By choosing a rational approximation of τ, we obtain a rational approximant. The closer this approximates the golden mean, the better the approximation of a quasiperiodic sequence. This is useful in simulation techniques requiring periodic boundary conditions, and in modelling quasicrystal approximants.

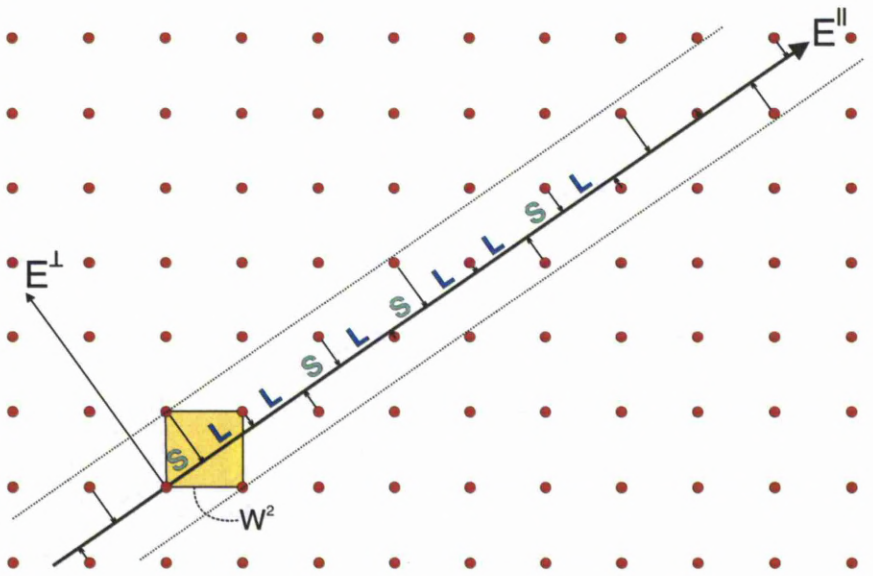

Figure 1.14: Cut and project method for obtaining periodic sequences. If the gradient is arctan τ then the resulting sequence of **SLLSL...** is the Fibonacci sequence.

1.6 Tiling Surfaces

It turned out that the problem of filling space with forbidden symmetries had already been considered and solved mathematically, before Shechtman's discovery. The problem is easier to consider first in 2-D. A tiling is a finite number of polygons, or tiles, which are arranged to fill the surface with no overlaps or gaps. The surface can be easily filled using one tile, such as rectangles, triangles, squares or hexagons, in a periodic fashion. This will always give the rotational symmetries found in classical Bravais lattices (2, 3, 4 or 6-fold). Aperiodic patterns with forbidden symmetries are less trivial. Consider the fivefold case. A surface cannot be completely covered using one pentagon tile. However, it can be done using multiple tiles.

Roger Penrose, the Emeritus Rouse Ball Professor of Mathematics at Oxford, discovered aperiodic tilings with fivefold rotational symmetry, and no translational order. The Penrose P1 tiling, Fig. 1.15, discovered in 1974, uses 4 tiles: boat, star, pentagon and rhombus. In his most famous work, the Penrose P3 tiling, Fig. 1.16, he was able to reduce the number of tiles further, to just two. This uses a fat rhombus (interior angles of 108° and 72°) and a skinny rhombus (36° and 144°), where the ratio of areas is τ. The ratio

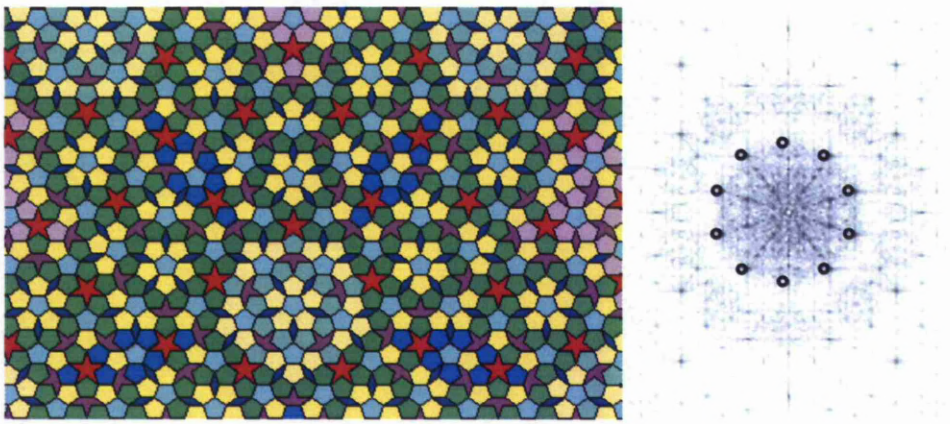

Figure 1.15: **Left** Penrose P1 Tiling **Right** FFT of this tiling, showing 10-fold symmetry.

of fat to skinny rhombus is also τ. They are arranged with matching rules (Fig. 1.17), so that no two rhombi can form a parallelogram, and to force the tiles to be assembled aperiodically. This reduces the total number of possible arrangements (to close a 360° vertex) from 54 to just 7, but this still allows options of how to place each tile. This random nature means that there is no translational symmetry, and that no two infinite Penrose tilings are the same. However, parts of the pattern will be repeated throughout. Notice the repeated motifs such as the 10 tile decagon, Fig. 1.16. Some have a perfect 5-fold symmetry, with 5 central fat rhombi making a star, and 5 outer skinny rhombi. Although this is repeated several times in this section of tiling, there are many more decagons with a more complex asymmetric structure. Even though they are not identical, and there is no translational symmetry, it is easy to see how constructive interference still occurs from most points, giving a diffraction pattern with 5-fold rotational symmetry, and 10-fold symmetry at some distances, Fig. 1.21.

Next to each tiling is a Fast Fourier Transform (FFT) of the image. An FFT is a way to simulate a diffraction pattern, using computationally efficient algorithms. This method replaces more traditional techniques such as the optical diffractometer. The Penrose tilings clearly give forbidden symmetry, with the 10-fold symmetry standing out most from these FFTs. As the FFT process involves an inversion axis, this is consistent with 5-fold symmetry. The finer detail cannot be seen because this is a crude approximation, from a very small part of the pattern. Mackay [9] has shown how these tilings can be represented as an atomic arrangement, by placing atoms at the vertices

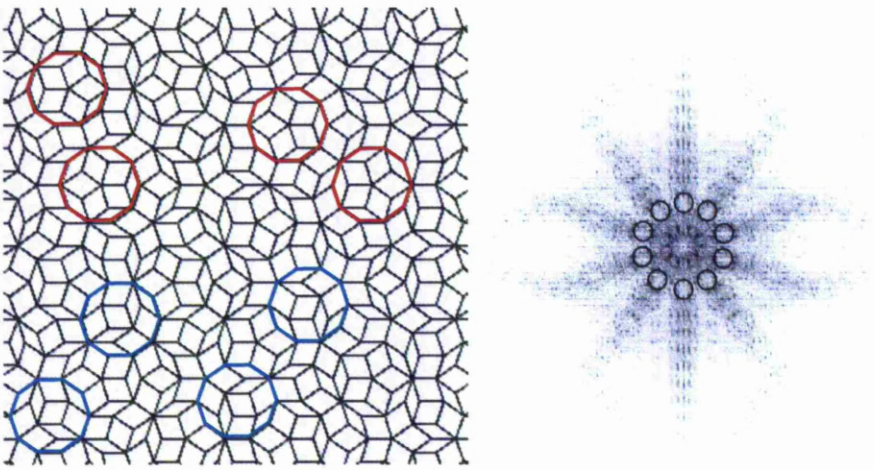

Figure 1.16: **Left** Penrose P3 Tiling, using just fat and skinny rhombi. Some decagons are highlighted to show different possible internal structures. **Right** FFT of this tiling, showing 10-fold symmetry.

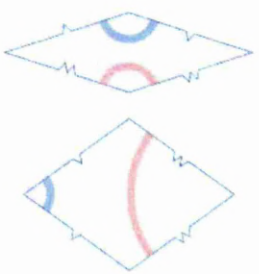

Figure 1.17: Matching rules for a P3 tiling - Tiles must be assembled so that the curves across their edges match in color and position. An equivalent condition is that tiles must be assembled so that the bumps on their edges fit together.

of tiles, which he called quasi-lattice points. Fig. 1.18 shows the original diagram using circles to represent atoms. The adjoining FFT clearly shows how the 10-fold symmetry is preserved. Fig. 1.19 shows a representation of how atomic potentials would look in this arrangement.

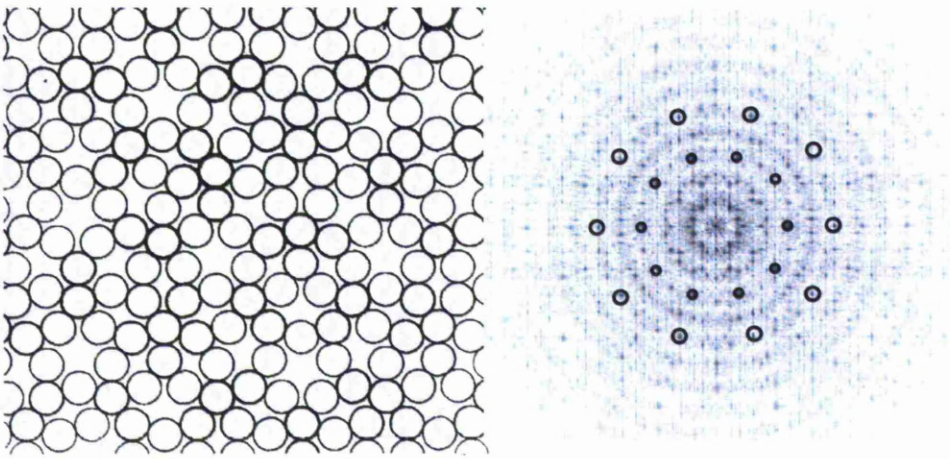

Figure 1.18: **Left** Penrose P3 Tiling, drawn with a circle at each quasi-lattice point, to simulate an atomic arrangement; from **Right** FFT shows strong 10-fold symmetry.

These 2D Penrose tilings can actually match the surface of some real quasicrystals. Fig. 1.20 shows a Penrose P1 tiling overlaying a high resolution STM image of the clean five-fold surface of the icosahedral Al-Pd-Mn (i-Al-Pd-Mn) quasicrystal. This was taken at Liverpool University [10]. The pattern is an obvious match, with atomic positions at each quasi-lattice point. The authors came to the conclusion that the i-Al-Pd-Mn surface is a termination of the bulk structure (no surface reconstruction occurs - it follows the underlying pattern of the chosen plane in the bulk). The real LEED pattern for the fivefold surface of i-Al-Pd-Mn is shown in Fig. 1.21. There is a close similarity to the FFT's from Penrose tilings, highlighting their connection. As well as the bright outer spots showing 10-fold symmetry, detailed spots showing the fivefold symmetry can also be seen. This real diffraction pattern shows more information because it is generated from a much larger section than the equivalent FFT from the tilings above. Even when using a focused electron beam, there are a huge number (in the range of Avogadro's number) of scattering centres (atoms/electrons).

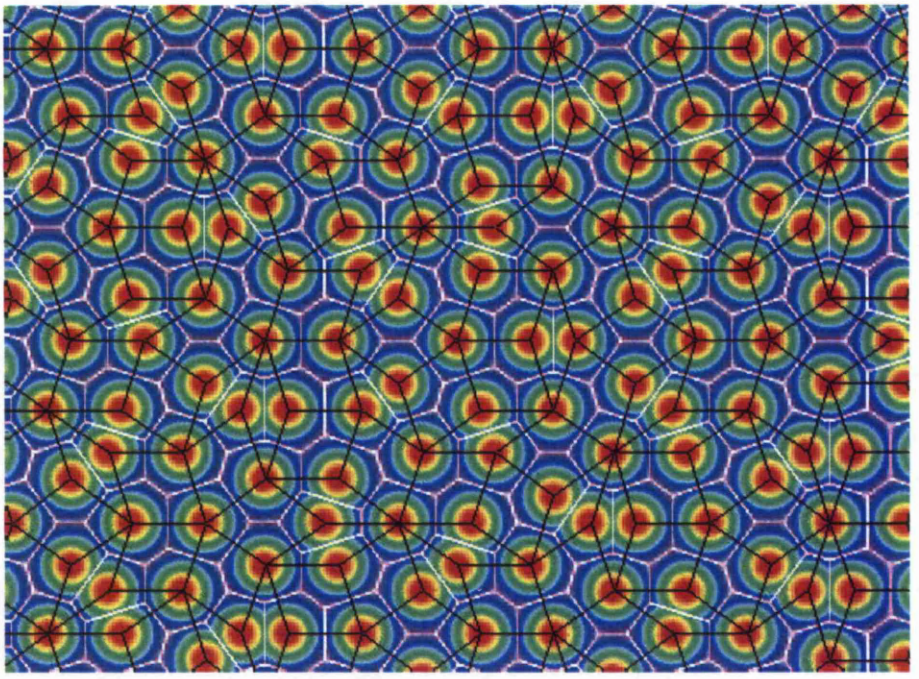

Figure 1.19: This enhanced Penrose P3 tiling gives a more realistic impression of how actual atoms would sit. Created as part of "Visualizing point sets, fractals, and quasicrystals using raster techniques", by Ned Allis, Jeff Dumont and Cliff Reiter. From: ww2.lafayette.edu

1.7 3-Dimensional Tilings

To model a real quasicrystal, these 2-D tilings must be extended to 3-D. This can be done by simply stacking aperiodic planes up, in a periodic manner. This matches the structure of some 2-dimensional quasicrystals (see Section 2.2), such as decagonal Al-Pd-Mn. However, this method cannot give a structure that is quasicrystalline in 3 dimensions. The Penrose tiling model can be extended to 3-D by replacing the rhombi with rhombohedrons [12], and assembling them with suitable face matching rules to force aperiodicity. This gives a truly icosahedral 3-D structure, giving very sharp diffraction spots, matching the patterns from high quality icosahedral quasicrystals. An alternate approach to get the same structure, is to start with a 6-dimensional face-centered hypercubic lattice, then project into 3 dimensions using the cut and project method. The structure of real quasicrystals will be looked at in more detail in the next chapter.

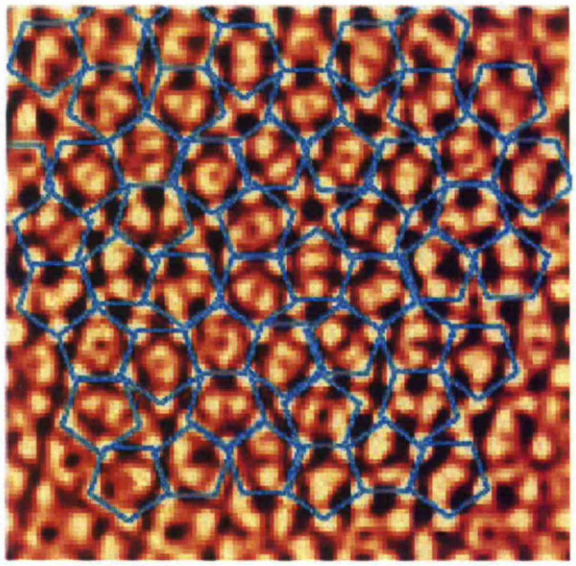

Figure 1.20: An exact patch of the P1 tiling superimposed on an enhanced high resolution STM image (100 Å x 100 Å) of *i*-Al-Pd-Mn [10].

Figure 1.21: A LEED pattern from the 5-fold surface of *i*-Al-Pd-Mn quasicrystal, showing 5-fold symmetry, taken at the University of Liverpool [11]

Chapter 2

Quasicrystal Structure

The first thermodynamically stable quasicrystal to be found was in the Al-Li-Cu system [13]. Many more stable quasicrystals were found, such as Al-Cu-Fe [14] and Al-Pd-Mn [15]. Although most of the research focused on aluminium based systems, quasicrystals are not limited to them. As the field grew, more systems were found to have quasicrystal phases, such as the Cd-Mg-RE [16] families (RE=any rare earth element) or Zn-Mg-Dy [17]. Other examples include titanium based quasicrystals such as Ti-Zr-Ni [18], and vanadium based such as V-Ni-Si [19]. As well as the initial 5-fold icosahedral phase, quasicrystals with 8-fold [19], 10-fold [20], and 12-fold [21] rotational symmetries were also discovered. Until recently, all stable quasicrystals were found in ternary systems (3 elements), with most binary systems being metastable. However, thermodynamically stable binary quasicrystals, such as icosahedral Cd-Ca and Cd-Yb, have now been found [22].

Quasicrystals can be grouped into the following categories:

2.1 3-D (Icosahedral) Quasicrystals

These have icosahedral symmetry and are truly aperiodic in all directions. The first quasicrystals discovered by Shechtman belong to this class. Other examples include the icosahedral phase of Al-Mn-Si [23], Al-Cu-Fe [24], and Al-Pd-Mn [15]. The latter was the first type to be grown to cm^2 size single quasicrystals, by conventional solidification. It is described as a typical F-type quasicrystal, whose structure can be described in terms of a face-centered six-dimensional hypercubic lattice [25], or equivalently as a 3-d Penrose tiling. The first suggestion for the structure, given by Shechtman [3], was the icosahedral glass model (see Section 1.4, page 11 for explanation). It consisted of icosahedral grains of limited size, surrounded by fcc bound-

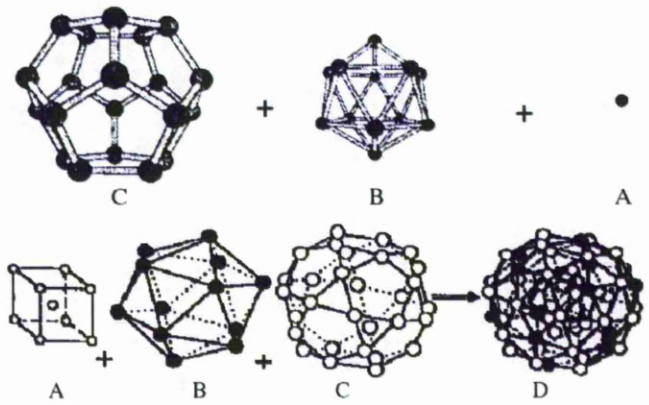

Figure 2.1: **Top:** representation of a Bergman cluster (33 atoms). The cluster is defined by a central atom **A**, a middle shell **B** (icosahedron: 12 atoms) and an outer shell **C** (dodecahedron: 20 atoms), from [26]. **Bottom:** representation of a pseudo-Mackay icosahedron **D** (51 atoms). The cluster is defined by an inner shell **A** (partially occupied dodecahedron: 9 atoms), middle shell **B** (icosahedron: 12 atoms) and an outer shell **C** (icosidodecahedron: 30 atoms), from [27].

aries that are no longer the same composition as the icosahedral region. This model gives broad diffraction spots, due to poor correlation between grains. As growing techniques improved, this picture no longer fitted. Perfecting the precise composition of the melt, so that there would be no deficiency of a particular element, enabled the icosahedral growth to continue unhindered throughout the sample, giving extremely sharp diffraction spots. This suggested icosahedral symmetry throughout the entire grain.

It has now been shown that the structure can also be described as a being built from a small number of polytopes. They are clusters of atoms arranged in a specific geometry to give icosahedral symmetry, such as the Pseudo-Mackay Icosahedron (PMI) and the Bergman cluster, shown in Fig. 2.1. Chemical interactions between clusters enforce face matching rules analogous to Penrose tilings. These clusters can vary in internal chemical arrangement, and they can overlap each other. Fig. 2.2, from [28], shows how PMI clusters are arranged in icosahedral Al-Pd-Mn. Individual PMI's form a larger PMI, where clusters occupy the positions that atoms would in the original. Each new generation in the hierarchy is found to be τ^3 larger in diameter than the previous generation. The golden number is synonymous with aperiodic order. At least three types of PMI have been found in Al-Pd-Mn,

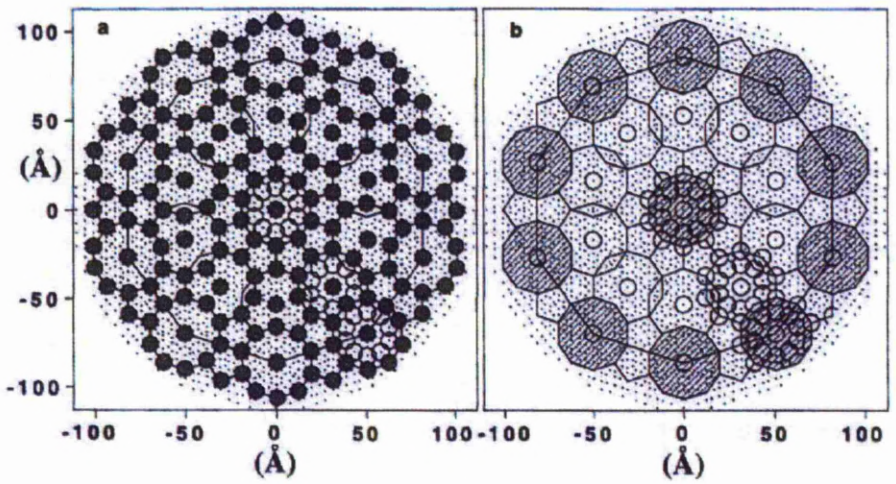

Figure 2.2: **a**. Possible configuration of the fivefold surface of Al-Pd-Mn. **b** Shows the inflationary hierarchy of clusters more clearly [28].

varying by chemical decoration. Interactions between clusters enforce face matching rules analogous to Penrose tilings. The diagram shows 3 generations of this hierarchy. In a perfect icosahedral quasicrystal this process continues throughout the entire volume. Bergman clusters also follow the same inflationary hierarchy structure, also known as *Hierarchical Recurrent Localization.*

Hierarchical inflation of aperiodic systems is also visible in nature. Romanesque broccoli/cauliflower is a prime example (Fig. 2.3). The florets are arranged in opposite spirals following the Fibonacci sequence (as with Fig. 1.12). Each floret is peaked with nodes in the same pattern, making it an identical but smaller version of the whole thing. Although too small to see in this picture, these nodes are also inflations of the previous level in the hierarchy.

There is still debate as to the exact proportions and arrangement of PMI and Bergman clusters in a quasicrystal lattice. Some models suggest that they are made from a mixture of both types of cluster, with the space in-between PMIs occupied by Bergman clusters [29], [30]. Alternatively, a study using diffraction data from both icosahedral and approximant compounds [26], suggests that PMIs form the real space atomic structure of a 6-dimensional simple cubic hyperlattice, whereas Bergman clusters relate to a 6-D face-centered cubic hyperlattice. An important observation, made

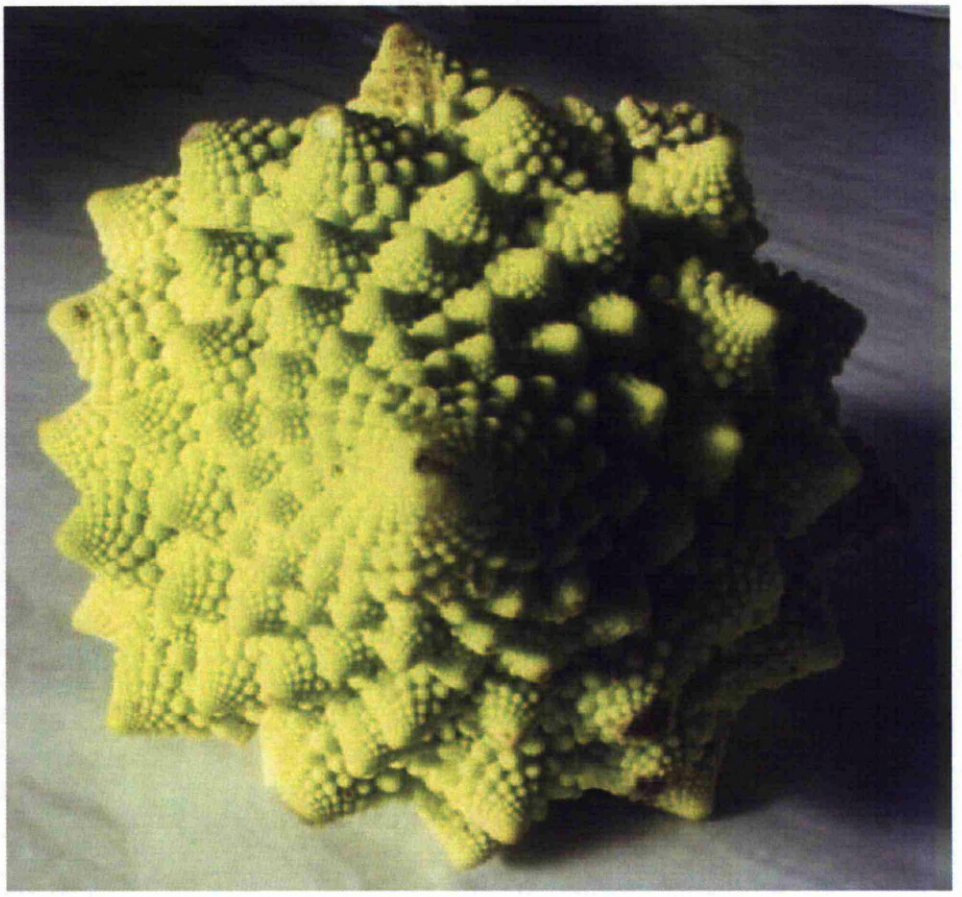

Figure 2.3: Two levels of Hierarchical inflation can be seen in the structure of Romanesque broccoli/cauliflower. Image from www.mcs.surrey.ac.uk

by Christian Janot et al. [28, 31], is the role of electron magic numbers (2,8,18,20,34...) in cluster formation. In an atom, when there is a magic number of electrons each shell is completely filled, giving a highly stable, low energy state. This is the driving force in most chemical reactions, as the atoms try to share electrons, to reduce the number of partially filled shells. In many reactions electrons are swapped directly between atoms. In metals, however, electrons are shared with the lattice in what is described as an electron gas. The number of electrons which each element contributes to the cluster is calculated, using accepted values such as Al=+3, Cu=+1, Fe=-2, Mn=-3. It has been found that the total number of shared electrons then approaches a magic number. It appears, therefore, that the individual

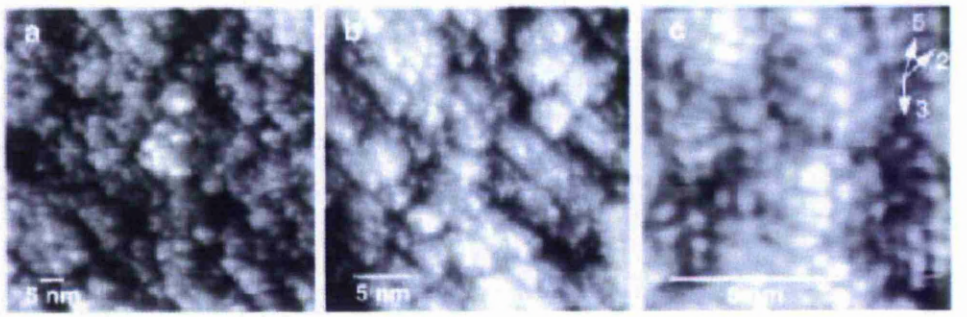

Figure 2.4: STM images of Al-Pd-Mn icosahedral single quasicrystal cleaved along a twofold plane. With increasing magnification smaller clusters appear. The diameter of about 1nm points to the Mackay-type cluster. Image from [32].

atoms are left with completely full orbits, and the cluster itself holds the extra electrons in its own stable full shell. The cluster can be viewed as a trap for a specific number of electrons that enforces localization. In effect, it behaves like an atom. There may be a small number of excess electrons in the cluster shell. These are then available for sharing between clusters in the next inflation of the hierarchy, which is reached when the excess electrons exceeds a magic number. In a truly icosahedral structure this process continues throughout the volume. If the hierarchy stops at some level, an approximant is formed, with a structure analogous to the icosahedral glass model.

The cluster nature of quasicrystals is clearly evident when a sample is cleaved , Fig. 2.4. The sample is prepared by *in-situ* cleavage in ultrahigh vacuum, and investigated using STM. This leaves a very rough surface due to the protruding clusters, which can actually be observed [32]. The hierarchical structure is also evident, with the elementary Mackay-type clusters (diameter of 1nm), first generation τ^3 inflated aggregates (diameter 5 nm), and second generation τ^3 inflated aggregates (diameter of 20 nm). The larger aggregates can be cleaved by crack propagation, revealing the subcluster structure.

The formation of stable icosahedral structures must also be viewed from its packing efficiency, as the most densely packed structure releases more lattice energy and is usually the thermodynamically stable state (neglecting extra energy released from other factors, such as magic numbers of electrons). The packing fraction of a quasicrystal is not necessarily better than a crystal, and the actual value depends upon the ratio of diameters. Example calculations for a binary quasicrystal are given in Table 2.1. The packing fraction is

only greater for a quasicrystal structure when the ratio of diameters is within a narrow range. In the 3 calculations, only at a ratio of 0.798 does the quasicrystal packing fraction exceed that of a crystal; therefore at this ratio a quasicrystal structure is thermodynamically stable. Ternary quasicrystals are more complicated, as there are three diameters to consider, and each combination will give a unique packing fraction.

Table 2.1: Quasicrystal Packing fraction. Data taken from [33].

Ratio of	Maximum Packing Fraction		
Diameters	Quasicrystal	Crystal	Disordered
0.888	0.580	0.683	0.572
0.833	0.618	0.658	0.502
0.798	0.648	0.643	0.462

2.2 2-D Quasicrystals

2-D Quasicrystals are periodic stacks of aperiodic layers, hence they are periodic in one direction and aperiodic in the other two. By altering the composition of the melt, intermediate phases, in between perfect icosahedral and classical crystal, can be observed upon solidification. For example, by increasing the proportion of Mn in Al-Mn to 18-22 at.%, the icosahedral phase is replaced by another non-crystallographic phase, the decagonal phase [20]. Layers of aperiodic 10-fold rotational symmetry, are stacked periodically on top of each other. It can be described as a 3-dimensional extension of a 2-D Penrose tiling. It has long-range orientational order, and one dimensional translational symmetry. Other decagonal quasicrystals include *d*-Al-Ni-Co, and *d*-Al-Cu-Co. Further types of 2-d quasicrystals are also possible, e.g. octagonal with 8-fold symmetry [34], and dodecagonal with 12-fold [21].

There are various structural models proposed for 2-D quasicrystals. In the Penrose tiling model, the atoms are arranged in clusters analogous to rhombic Penrose tiles. The required matching rules are provided by interactions between clusters. More recently, a different model was proposed, using a single repeating unit, the 'quasi-unit cell'. Fig. 2.5 shows the model for decagonal $Al_{72}Ni_{20}Co_8$ [35]. The unit cell is a decagonal tile. Rather than using two unit cells with matching rules to force aperiodicity, the quasi-unit cell can overlap in 2 ways, which still enforces an aperiodic Penrose tiling. Fig. 2.6 illustrates this, and shows how by decorating the tiles we still obtain a Penrose tiling.

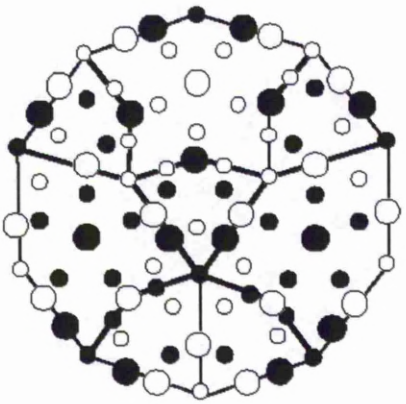

Figure 2.5: Decagonal quasi-unit-cell model for Al-Ni-Co. Large circles represent Ni and Co; small circles Al. The structure has two distinct layers along the periodic c-axis. Solid circles represent c = 0, open circles c = 1/2. From [36].

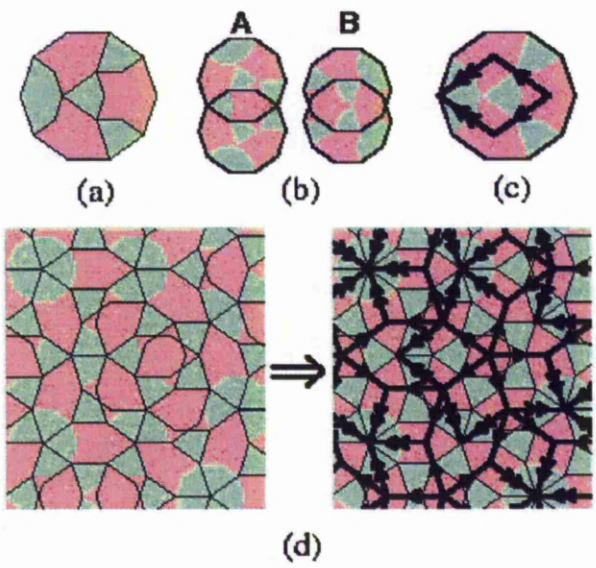

Figure 2.6: **(a)** A simplification of the quasi-unit cell from Fig. 2.5. **(b)** Two possible overlaps: **A** small area, **B** large area. **(c)** Decagon decorated with obtuse rhombi. **(d)** A tiling of overlapping decagons (left) is converted into a Penrose tiling (right) with this decoration, from [37].

2.3 1-D Quasicrystals

1-D Quasicrystals consist of quasiperiodic stacks of periodic planes (aperiodic in one direction, and periodic in the other two). For example in Al-Ni-Si [38], by reducing the proportion of Al to 68.5 at.% Al we can observe a phase in-between the decagonal 2D quasicrystal, and the crystalline CsCl type structure. In addition to the periodic translation along the 10-fold axis, one of the twofold axes normal to this becomes periodic. Fig. 2.7 shows the electron diffraction patterns for this 1D example.

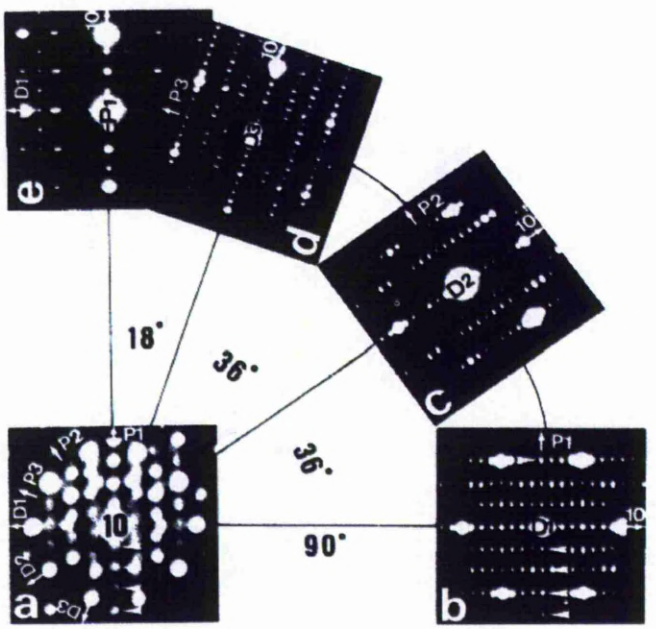

Figure 2.7: **a** shows the tenfold axis, which is stacked periodically; **b** shows the aperiodic **D1** axis perpendicular to this with the spots arranged aperiodically (as would be the case in the decagonal phase), the number of spots which correspond to a distance of 0.23 nm is 3, 5, and 13, following the Fibonacci sequence; this indicates 2D translation periodicities also associated with the Fibonacci sequence; **c** and **d** show this pattern change (not the case in the decagonal phase) as it is rotated to the **P1** axis (**e**), perpendicular to **a** and **b**; the periodic pattern of spots in **e** shows this axis is periodic. So this 1-D quasicrystal is aperiodic in the **D1** direction. From [38].

2.4 Approximants

Approximants are complex metallic alloys with large unit cells, having structures similar to the quasicrystalline phases, but arranged periodically. They can have similar properties to the quasicrystal, such as physical characteristics, structural motifs, valence electron concentration per atom and comparable lattice parameters (where comparison to 2-D or 1-D quasicrystals is possible). The Al-Cr-Fe phases are looked at in more detail in Section 2.5.

2.5 AlCrFe Literature review

2.5.1 AlCrFe

Chapters 4, 5 and 6 are investigations of the decagonal quasicrystal approximant Al_4(Cr, Fe), which is a periodic complex metallic alloy (CMA). CMAs typically have large unit cells, well-defined atomic clusters, and some inherent disorder in their ideal structure. It is thought that the cluster sub-structure may give rise to interesting physical properties resulting from the competition between the different length-scales of the clusters and the unit cell [39]. There have not been many surface science studies done on periodic CMAs, as most of the work has focused on quasicrystals [40]. ξ'-Al-Pd-Mn (0 1 0) is the most researched CMA, where the main interest has been comparison with the 5-fold icosahedral *i*-Al-Pd-Mn. In this this AlCrFe is studied as a model system to understand the structure and properties of a CMA, from a surface science perspective.

Until recently, very little research has been done into the Al rich corner of the Al-Cr-Fe ternary system. Some investigations, done before the discovery of quasicrystals, found that iron could be dissolved in the Al-Cr system, by replacing up to 25 at.% Cr with Fe in $AlCr_2$ [41], and up to 7.7% in aluminium rich $Al_{11}Cr_2$ [42]. Similarly, chromium could be dissolved in the Al-Fe system, up to 2.2% in Al_3Fe [42], replacing Fe with Cr. In all cases, there were no ternary intermetallic phases observed. By definition, an alloy is only classed as a new intermetallic phase when the new structure is different from its constituents. This means that the structure of the Al-Cr-Fe produced was identical to the original binary phase before dissolving the third element. In 1996, there was an attempt to establish a phase diagram for the Al-Cr-Fe system ([43]), based on dissolving the 3rd element at 1000°C for 100h, and quenching in ice brine. The phases determined are presented in Fig. 2.8. Despite finding higher solubility ranges (75 at.% Fe can replace Cr in Al_8Cr_5, and 6.4 at.% Cr can dissolve into Al_3Fe) there were still no new

ternary intermetallic phases discovered.

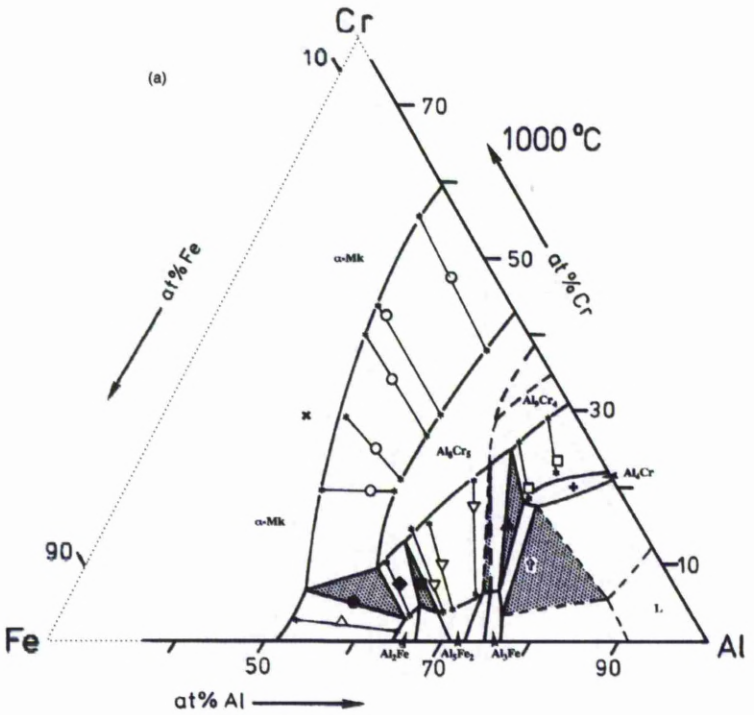

Figure 2.8: Isothermal section of the Al-Cr-Fe system at 1000°C, zoomed in on the Al rich corner. It is already a complicated system, but at this stage, the ternary intermetallic phases were not discovered. For full explanation of symbols refer to [43]

The discovery of quasicrystal phases in many similar systems, has led to a more in-depth look at the Al-Cr-Fe three-phase triangle, and intermetallic phases have now been found. The icosahedral phase was produced by heating to 1200° and rapidly solidified by centrifugal atomization [44]. Fig. 2.9 shows some electron diffraction patterns of this phase from each of the icosahedral symmetry axis [45]. These difraction patterns are similar to those obtained using LEED, but they were taken using a different technique called Transmission Electron Microscopy (TEM). However, the same information is revealed in reciprocal space about the symmetry of the crystal face.

Fig. 2.10 is a more up to date phase diagram, indicating the composition of many of the materials studied so far in this system. Several new ternary phases have been discovered so far, both quasicrystalline and large unit cell

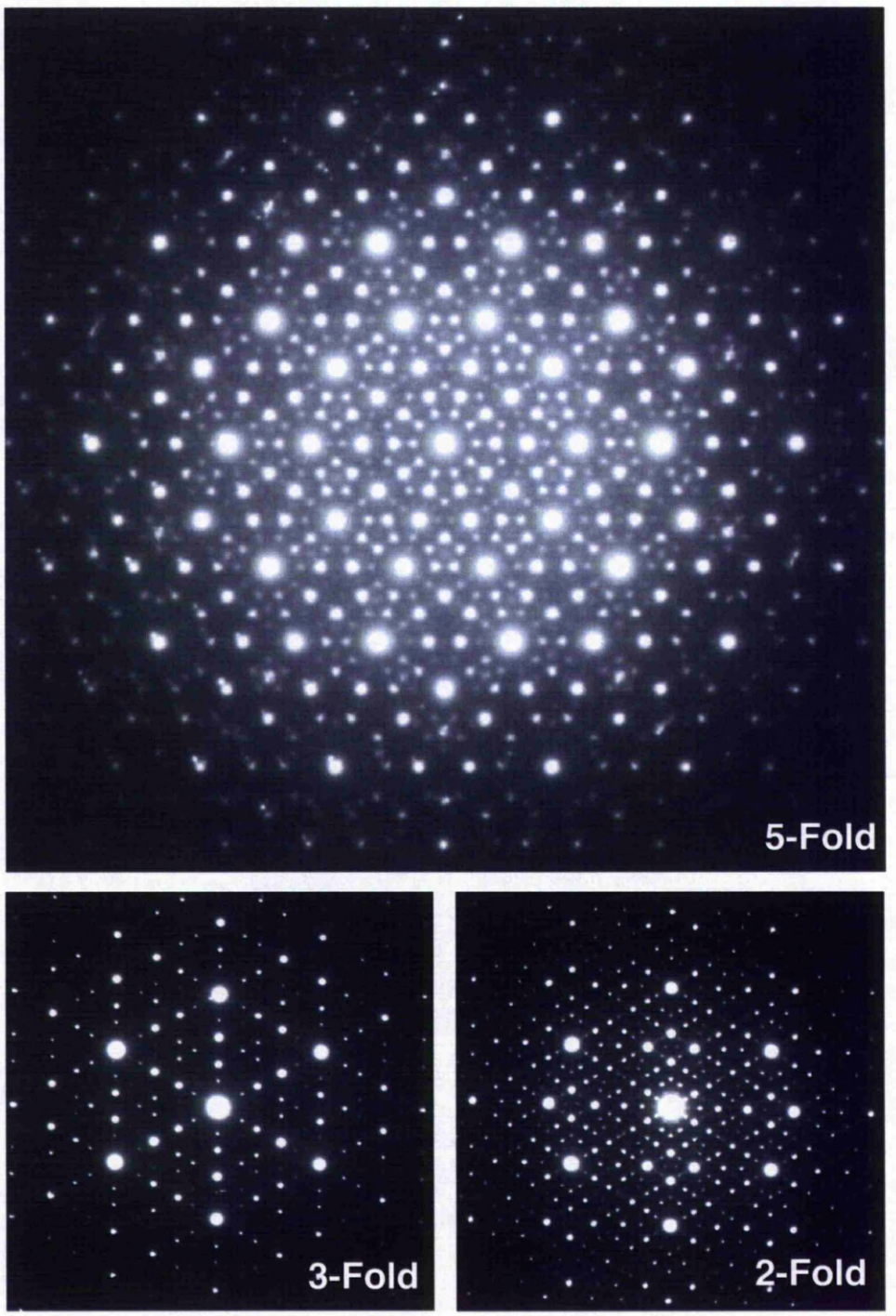

Figure 2.9: High quality electron diffraction patterns from i-Al-Cr-Fe [45], of each high symmetry axis.

phases, including hexagonal, monoclinic and orthorhombic systems, which are found split into further intermetallic phases with different lattice parameters (see caption). Most of these phases are metastable. Quasicrystalline icosahedral *i*-Al-Cr-Fe exists in a large part of this region, as well as the decagonal phase *d*-Al-Cr-Fe. Many of the phases close to the composition of these are approximants of the of the quasicrystalline phases. An extensive list of many of the Al-Cr-Fe phases are given in Table 2.2 and 2.3, indicating the many possibilities, which are too numerous to describe individually in detail.

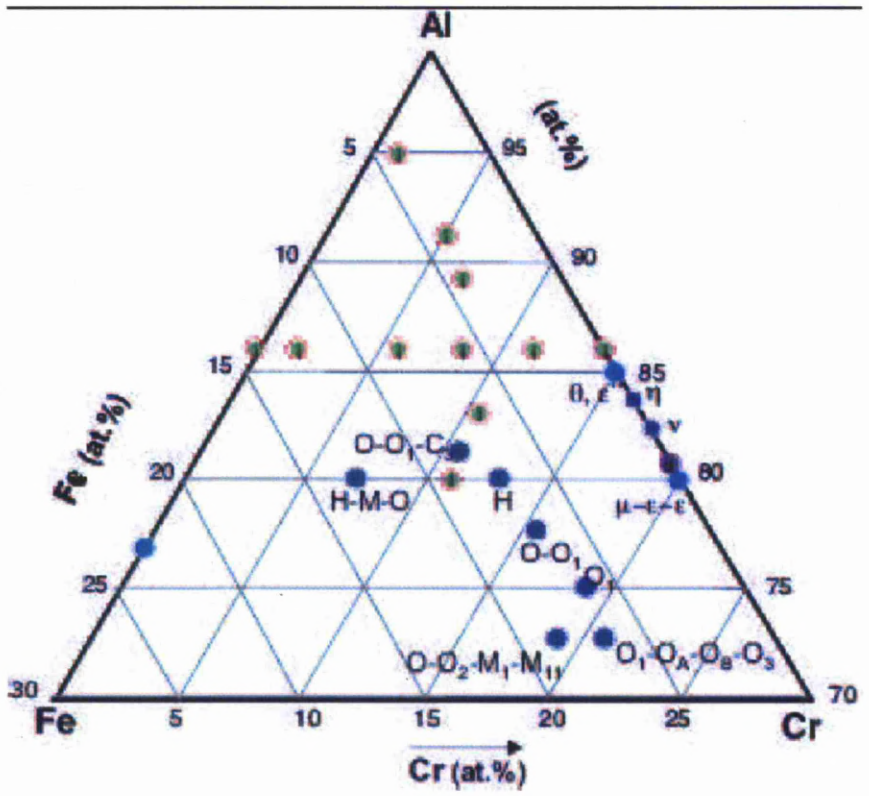

Figure 2.10: The composition and phase of materials studied in the Al-Cr-Fe system, (compiled by V. Demange, CMA Vil.D meeting, Nancy, 2007). **KEY: Quasicrystals**: (green circle) i = icosahedral, (purple circle) d = decagonal. **Ternary Phases** (Dark blue circles): H = Hexagonal; M,M_1,M_2 = Monoclinic; O, O_1, O_2, O_3, O_A, O_B, O_C, O_3.1 = Orthorhombic **Binary Phases** (light blue circles): ε''-$Al_{11}Cr_2$, ε-Al_4Cr, ε-Al_4Cr = orthorhombic; λ-$Al_{13}Fe_4$ = monoclinic

2.5.2 Focus on ε-Al_4(Cr,Fe) approximant

One particular approximant, whose structure has now been determined by x-ray diffraction [46–48], is the orthorhombic phase ε-Al_4(Cr,Fe), an approximant of the decagonal phase, with the composition $Al_{79.7}Cr_{15.4}Fe_{4.9}$. It has a large orthorhombic unit cell, with dimensions a $\approx$ 1.25 nm, b $\approx$ 1.25 nm, and c $\approx$ 3.05 nm, and a six layer structure, shown in Fig. 2.11, consisting of flat (F) and puckered layers (P). A 3-d model of this unit cell is shown in Fig. 2.12.

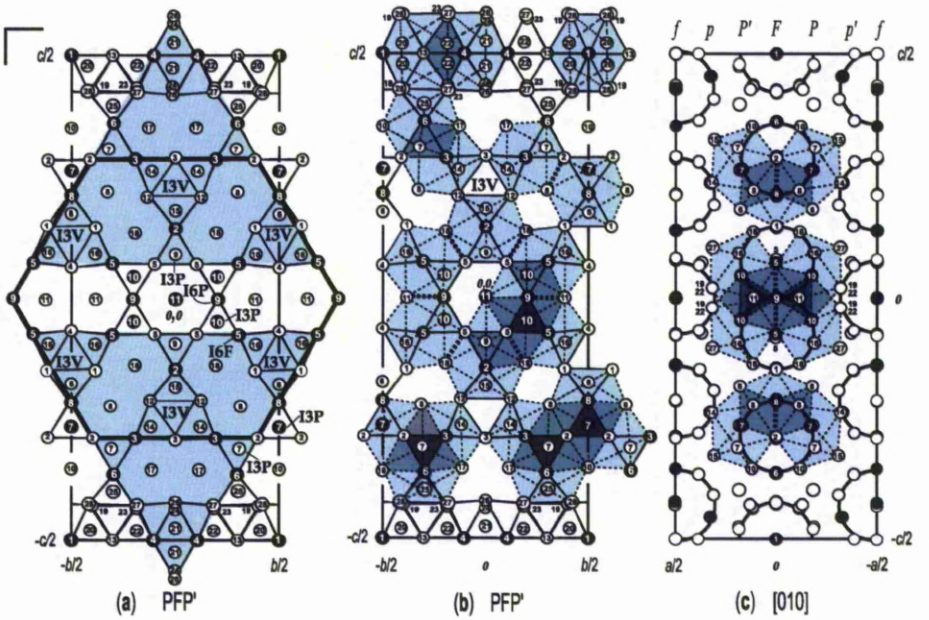

Figure 2.11: **(a), (b)** The [100] projection of the PFP' layers of the structure of Al_4(Cr, Fe) from [46]: full circles = TM (transition metal) = Cr/Fe atoms ; open circles = Al atoms. Atoms in the flat layer F are connected, whereas atoms in the puckered layers P and P' across the mirror F (superimposed) are not. **(a)** highlights the triangular (shaded) and hexagonal (bold lines) structural motifs; **(b)** highlights icosahedra (shaded) and the icosahedral clusters I3V, I3P, I6F and I6P. **(c)** The [010] projection shows the six PFP'pfp' layers and the icosahedra centred at TM7 and TM10 (i.e. the black circles, numbered 7 and 10) binding together the PFP' and pfp' layer blocks, which are related by a symmetry operation.

The internal structure has strong icosahedral symmetry. There are 28 crystallographically independent Al sites, of which 5 are icosahedrally co-

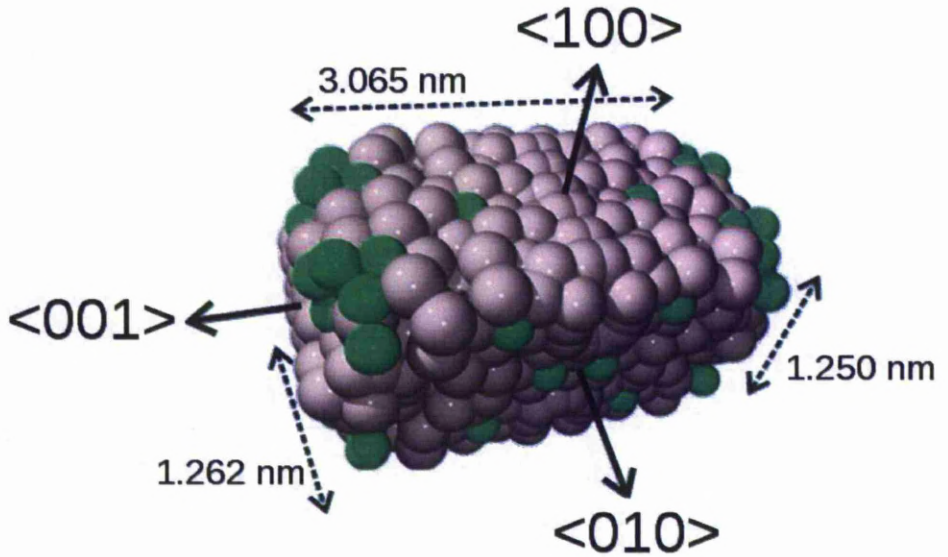

Figure 2.12: A model of the orthorhombic $Al_4(Cr,Fe)$ unit cell, built using the data from Deng et al. [46] on Diamond crystal modelling software. Al atoms are shown in white and transition metal atoms in light grey. Unit cell vectors are indicated.

ordinated. There are 11 TM (Transition Metal) sites, where Cr and Fe are interchangeable, of which 10 are icosahedrally coordinated. There are several icosahedra formed by these 15 sites, which are indicated on Fig. 2.11. They are all oriented in the same axis, and there are several notable interconnections. An I3V cluster is formed by 3 vertex sharing icosahedra; I3P cluster from 3 mutually interpenetrating icosahedra (I6P from 6); and an I6F cluster from 6 face sharing icosahedra. The bottom left of Fig. 2.11(b) shows an I3P cluster forming a triangular hexahedron. Many I3V clusters can also be seen, such as the ring of 3 icosahedra around the triangle marked I3V in Fig. 2.11(b). These clusters are common packing units in CMAs, for example I3V and I3P clusters exist in many hexagonal intermetallic phases such as ν-$Al_4(Fe,Cr)$ [49].

Fig. 2.11(c) also shows circles of 10 atoms forming icosahedral or pentagonal antiprisms, with the 5-fold axis in [010] direction. The proliferation of icosahedra, and their alignment along common axis, give the approximant strong icosahedral symmetry. However this symmetry is broken by split occupancy (2 Al sites have a 25% chance of being occupied by a TM) and partial occupancy (10 Al sites have only a 50-66 % probability of being occupied,

otherwise leaving a vacancy, and 2 TM sites have a 70% chance of occupation). This produces distorted pseudo-icosahedra. Of the 15 icosahedral positions, 7 are only pseudo-icosahedrally coordinated. A true icosahedron has 1 atom at the centre, surrounded by 12 atoms, giving it a coordination number CN=12. Due to the partial and split occupancies, these icosahedra can become distorted, and can have different coordination numbers (Fig. 2.13).

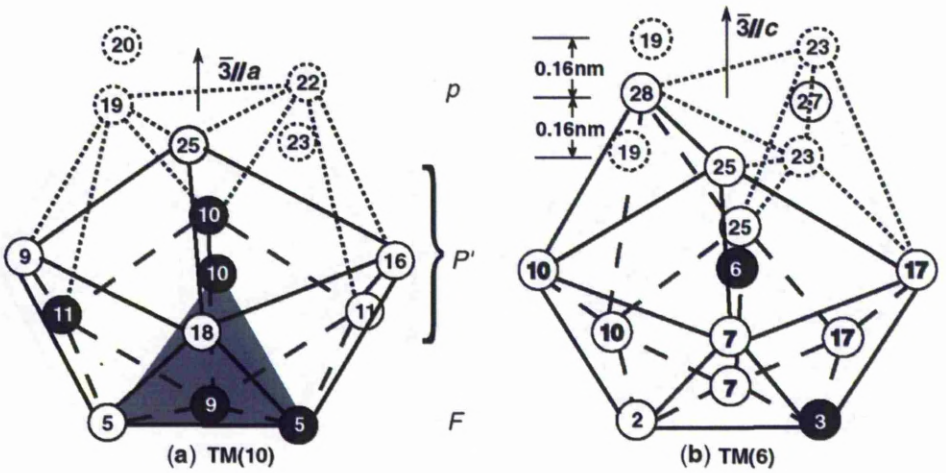

Figure 2.13: Just two examples of possible pseudo-icosahedra in the AlCrFe decagonal approximant: **(a)** centred at TM(10) in FP'p layers with the partially occupied site Al(25) in the P' layer and the split sites Al(19), Al(20), Al(22) and Al(23) in the p layer, $CN_{eff} = 11.4$. The shaded region is a tetrahedron. **(b)** centred at TM(6) in the PFP' layers with the partially occupied Al(27) and Al(28) sites in the F layer and the split sites Al(19) and Al(23) in the P and P' layers; $CN_{eff} = 11.6$. Al atoms are white, Cr/Fe are found at the black TM positions.

It can be seen from this example that the structure of the approximant is closely related to the quasicrystal, as the main structural unit is an icosahedron. However, the arrangement of these icosahedra is not the same, and they can be distorted. The small difference in atomic composition means that icosahedral growth cannot continue throughout. From the inflationary hierarchy point of view, there isn't the correct number of electrons to make a magic number. The breakdown in the icosahedral inflation leads to the growth of other stable large structures, which are closely related to adjacent intermetallic phases and have different rotational symmetry. Many other structural features, as well as the 3-fold and 6-fold clusters already men-

tioned, have this symmetry. A striking feature is the ring of 6 icosahedra (I6F) centered around the hexagonal antiprism at TM(11) in Fig. 2.11(b). This can also be viewed as having an I6P ring in between, with each icosahedron centered at TM(9) and Al(5). This chemical make-up means that this ring is only strictly 2-fold. However, the same configuration of icosahedra with real 6-fold symmetry occurs frequently as a structural motif in hexagonal intermetallic phases, such as λ-Al_4Mn [50] (which is closely related to ν-Al_4(Cr,Fe) [49]). Fig. 2.11(a) shows how this forms a larger pseudo-6-fold structural motif, indicated by the hexagon in bold line. Large triangular motifs are also shown by the shaded regions. Note the similarity to the large triangles found in the hexagonal phase ν-Al_4(Cr,Fe), highlighted in Fig. 2.14.

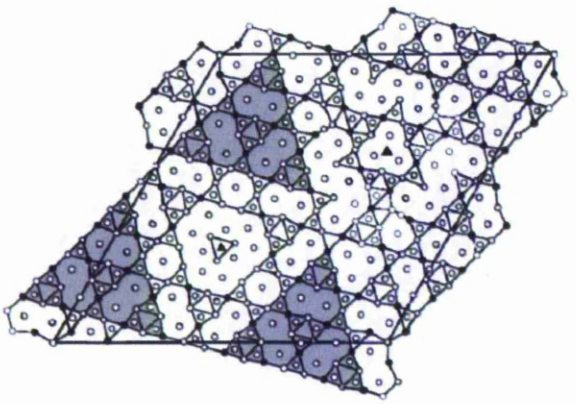

Figure 2.14: Triangular structural motif (shaded) in the PFP' layers of the hexagonal ν-Al_4(Cr, Fe) (data from [49]), isostructural to the triangular region in Fig. 2.11(a)

Fig. 2.15 shows the major surfaces of this phase, built using the unit cell from Fig. 2.12. The FFT is shown below each. The triangular and hexagonal features give the [100] surface a pseudo-6-fold diffraction pattern. The pattern is not quite perfect, hence the necessity of the prefix 'pseudo'. The similar structural motifs and 6-fold symmetry show why this phase is an approximant of the hexagonal phase. Another attribute, common with κ λ and ν hexagonal phases and this approximant, is that they all have a six layer PFP'pfp' structure, stacked in c with a period of about 1.25 nm. The decagonal arrangements on the [010] surface give it a pseudo-10-fold FFT, and indicate why this is also an approximant of the decagonal quasicrystal. Hence, this approximant phase is closely related to both the decagonal phase and the hexagonal phase, and is considered to be the phase in between quasicrystals and periodic crystals.

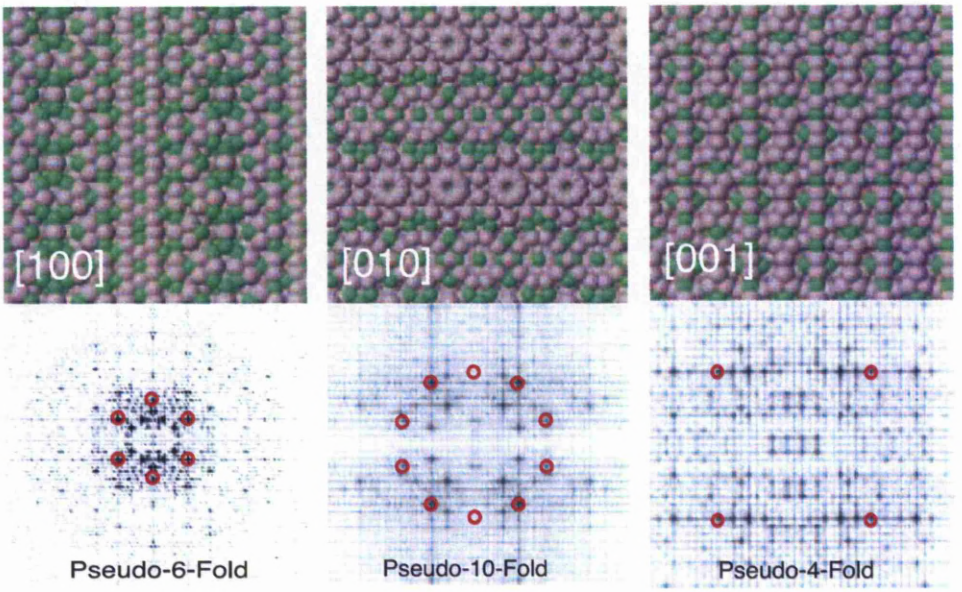

Figure 2.15: Major surfaces of AlCrFe decagonal approximant, built using data from [46] on Diamond software. The attached FFTs shows the rotational symmetry of each surface. The [100] surface has pseudo 6-fold symmetry approximating the hexagonal phase, and the [010] surface has pseudo 10-fold symmetry, approximating the decagonal quasicrystal phase.

2.5.3 γ-brass phases

As can be seen from Fig. 2.10, the icosahedral phase only occurs when the Al at.% is above 80%, and the decagonal phase occurs near this boundary. The approximant in the previous section, orthorhombic phase ε-$Al_4(Cr,Fe)$, was also close to this boundary with 80.6 at.% Al. By reducing the amount of Al, different approximant phases are observed, as the structure becomes less quasicrystalline and more like a classical periodic crystal. At $\approx$70 at.% Al we find γ-brass phases in the Al-Cr-Fe system.

γ-brass phases have often been observed in many systems at compositions close to quasicrystal phases (e.g. Al-Cu-Cr-Fe and Al-Cu [51], Al-Cu-Cr [52]) and it is suggested that the γ-brass phases are actually approximants of quasicrystals [51]. Like the approximant in the previous section, the structure can be described as a stacking of flat and puckered atomic layers, with distorted pentagrams forming channels of pentagonal antiprisms. They also have strong orientational relationships with quasicrystals, and similar diffraction patterns.

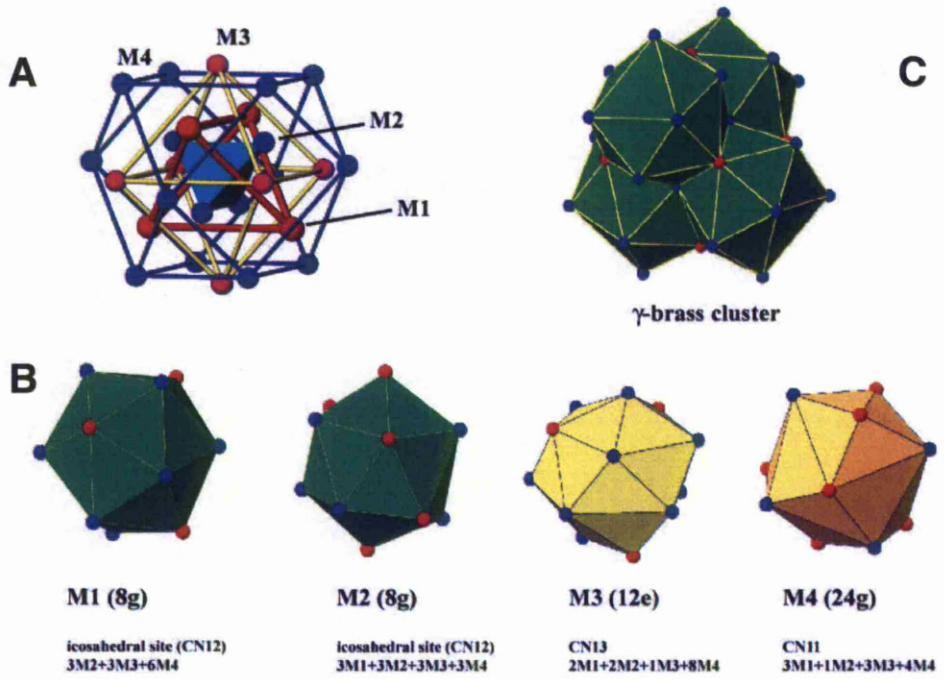

Figure 2.16: **A**. γ-brass cluster, showing the 4 layer structure: inner tetrahedron, outer tetrahedron, octahedron, surrounded by a cuboctahedron. **B**. Most sites have effective coordination numbers CN=12, forming distorted icosahedra. Other sites with different coordination numbers, form non-icosahedral closely related structures. **C** A tetrahedral network of distorted icosahedra, found in the γ-brass phase. Image courtesy of Ames Lab, Iowa.

The first definition, in 1933, of a γ-brass phase was as a specific cluster formation [53]. It is comprised of 26 atoms in 4 shells (Fig. 2.16A): an inner tetrahedron surrounded by an outer tetrahedron, then an octahedron (6 atoms), surrounded by a cuboctahedron (12 atoms). These clusters can be arranged into various ways to form different structures. The cubic γ-brass phase can be primitive CsCl type, with 2 types of γ-brass cluster, of different chemical composition, at each lattice point [54]. It could also form body centered cubic (identical clusters) [54] or face centered cubic (4 different clusters) [55]. Tetragonal [56] and hexagonal [43] lattices have also been observed. A distortion of the bcc lattice has also been observed [57] forming a rhombohedral phase.

The γ-brass phases can also be described as tetrahedral close packed

structures [58]. Many atoms in the structure are surrounded by 12 atoms, forming distorted icosahedra (Fig. 2.16B). Some icosahedra are arranged in fours, forming a tetrahedral network, by sharing the edges of one face (Fig. 2.16.C) [59]. Viewing the structure as distorted icosahedra has been an accepted definition of the γ-brass phase since 1970's, and highlights the link with quasicrystal phases.

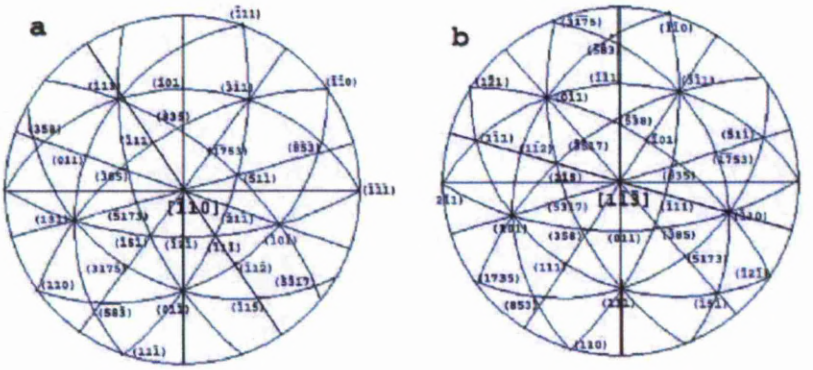

Figure 2.17: Stereographic projections along the $[\bar{1}10]$ and the $[1\bar{1}\bar{3}]$ directions of the $Al_9(Cr,Fe)_4$ γ-brass phase, showing slightly imperfect fivefold symmetry, due to distorted icosahedra.

Two examples of γ-brass phases in the Al-Cr-Fe system are given by Demange [60]. The first alloy, with a composition furthest away from quasicrystals is $Al_{67.6}Cr_{23.3}Fe_{9.1}$ (i.e. 67.6 at.% Al). It was found to be made of polygrains of a single phase, the rhombohedral γ_2-$Al_8(Cr,Fe)_5$ phase (isomorphic to rhombohedral γ-brass Al_8Cr_5). The second alloy had a composition closer to quasicrystals, $Al_{72.5}Cr_{19.5}Fe_8$ (i.e. 72.5 at.% Al). Multiple structures were found in this alloy, including the rhombohedral γ_2 phase found in the first alloy. Coexisting with this was another approximant phase, the orthorhombic O_1 approximant [61]. Several approximants of the decagonal phase also coexist in the alloy. Another γ-brass phase was also discovered in this alloy, the body centered cubic γ_1-$Al_9(Cr,Fe)_4$ phase (N.B. the rhombohedral γ_2 phase is a distortion of this). Even after many days annealing, to remove any metastable phases, there was no change in the number of diffraction peaks, indicating that this is truly an equilibrium phase. So, while the first alloy (γ_2 phase) has some quasicrystal properties, the second alloy appears a step closer to actually becoming one, suggesting the bcc γ_1 phase is also closer to the quasicrystal phases. This again highlights the strict relationship between composition and quasicrystal formation. Stereographic projections of the cubic γ_1-brass phase (Fig. 2.17) show very strong

resemblance with the stereographic projection along the 5-fold axis of an icosahedral quasicrystal (Fig. 2.18), indicating how close the structural relationship is. The structural model proposed is actually composed of distorted icosahedra Fig. 2.19.

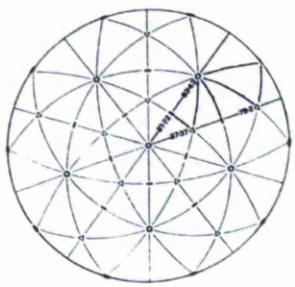

Figure 2.18: Stereographic projection along a 5-fold axis of the quasicrystalline icosahedral phase, showing perfect fivefold symmetry and a strong resemblance with Fig. 2.17

2.5.4 τ-scaling

As mentioned in Section 1.5.3, an approximant structure can be modelled, by the cut and project method, from higher dimensional space using a rational approximant of the golden mean. They also have structural motifs, reminiscent of quasicrystals, with τ-scaled relationships. One example is shown in Fig. 2.20, comparing the γ_1-brass phase with an approximant phase. The similarity of the motifs and τ-scaling relationship show the strong connection between the γ-brass phase, approximants and quasicrystals.

2.5.5 Conclusion

There are many approximants in the Al-Cr-Fe system, but a general observation is that they show the beginnings of quasicrystal formation. Alloy compositions near to quasicrystals may start to grow with icosahedral type clusters but there is a driving force towards periodicity the further the composition moves away. The incorrect ratio of different size atoms restricts the icosahedral growth and requires a different structural arrangement to fill the

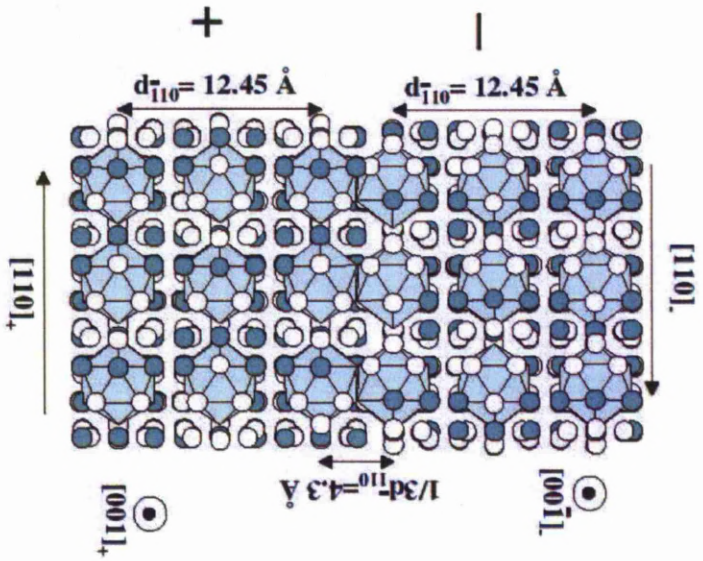

Figure 2.19: Structural model of an inversion boundary between + and - domains along the [001] direction. Distorted icosahedra belonging to the structure are represented. On each boundary side, icosahedra possess distinct orientation, due to the non-centosymmetric structure. At the boundary, icosahedra are joined side by side, sharing several atoms.

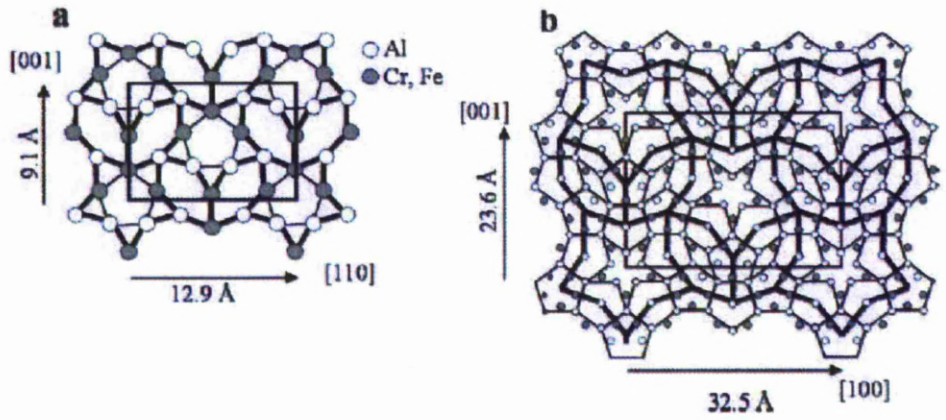

Figure 2.20: **a** Structural model of a single atomic layer for $Al_9(Cr, Fe)_4$ γ_1-brass phase along the [110] direction. **b** Structural model of the O_1-AlCrFe approximant phase along the [010] direction. Note the strong similarity in structural motifs. The increase in scale corresponds to a rational approximant of τ^2 (using $\tau \approx 1.6$, or 8/5 in the Fibonacci sequence).

space, distorting the icosahedra more and more as the composition moves away. The change from aperiodic icosahedral to classical periodic structures is complicated with many phases. The unit cell changes from infinite (perfect quasicrystal) to smaller and smaller finite numbers as we move towards the well known Bravais lattices of the surrounding binary phases. This picture also fits the magic number theory of hierarchical inflation - as the icosahedral clusters start to grow, the clusters no longer have a magic number of electrons limiting the growth of the next stage. If the number is only slightly out there can be some growth, leading to large unit cells with internal icosahedral (or pseudo-icosahedral) symmetry, but themselves arranged periodically. The farther away it is from a magic number, the smaller the number of possible inflations, and therefore the smaller the unit cell.

Table 2.2: Al-Cr-Fe Phases, part 1

Phase	Structure	Lattice parameters	References .
θ-Al_7(Cr,Fe)	monoclinic	a = 25.2 Å, b = 7.6 Å, c =10.9 Å, β =128°	Zoller. Arch. Ang. Wiss. U. Techn. 26 (1960)
η-Al_{11}(Cr,Fe)$_2$ (ε)	orthorhombic	a = 12.4 Å, b = 34.6 Å, c = 20.2 Å	Pratt *et al* J. Inst. Metals 80 (1951)
μ-Al_4(Cr,Fe)	hexagonal	a = 21.6 Å, c = 16.4 Å	Palm. J. All. Comp. 252 (1997)
H-AlCrFe (ν)	hexagonal	a = 40.7 Å, c = 12.4 Å	Sui *et al* Phil. Mag. Lett. 79 (1999), Mo *et al* Mat. Sci. Eng. 294-296 (2000)
O-AlCrFe	orthorhombic	a = 12.3 Å, b = 12.4 Å, c = 30.7 Å	Sui *et al* Phil. Mag Lett. 71 (1995), Sui *et al* Acta Cryst. B53 (1997)
ε-Al_4(Cr,Fe)	orthorhombic	a = 12.3 Å, b = 12.4 Å, c = 30.7 Å	Deng *et al* J. Phys.:Condens. Matter. 16 (2004)
γ_1-Al_9(Cr,Fe)$_4$	hexagonal	a =12.9 Å, b = 15.6 Å	Palm. J. All. Comp. 252, (1997)
γ_1-Al_9(Cr,Fe)$_4$	cubic	a = 9.123 Å	Demange *et al* Phil. Mag. 85 (2005)
γ_2-Al_8(Cr,Fe)$_5$	rhombohedral	a= 9.051Å, β = 89.16°	Palm. J. All. Comp. 252 (1997)
λ-Al_{13}(Cr,Fe)$_4$	monoclinic	a = 15.5 Å, b = 8.0 Å, c = 12.4 Å	Palm. J. All. Comp. 252 (1997)
M-AlCrFe	monoclinic	a = 33.1 Å, b = 12.3 Å, c = 24.8 Å, β =112°	Liao *et al* Phil. Mag. A. 1998 78

Table 2.3: Al-Cr-Fe Phases, part 2

Phase	Structure	Lattice parameters	References .
O_1-Al-Cr-Fe	orthorhombic	a = 32.5 Å, b = 12.2 Å, c = 23.6 Å	Demange *et al* Mat. Sci. Eng. 294-296 (2000)
$C_{3,I}$-Al-Cr-Fe	orthorhombic	a= 32.7 Å, b = 12.5 Å, c = 23.8 Å	Demange *et al* Mat. Sci. Eng. 294-296 (2000)
O_2-Al-Cr-Fe	orthorhombic	a = 32.5 Å, b = 12.2 Å, c = 23.6 Å	Demange *et al* Appl. Surf. Sci. 173 (2001)
O_A-Al-Cr-Fe	orthorhombic	a = 45.4 Å, b = 12.4 Å, c = 14.7 Å	Demange *et al* Phil. Mag. 86 (2006)
O_B-Al-Cr-Fe	orthorhombic	a = 70.5 Å, b = 12.4 Å, c = 14.7 Å	Demange *et al* Phil. Mag. 86 (2006)
O_E-Al-Cr-Fe	orthorhombic	a = 12.5 Å, b = 12.4 Å, c = 14.3 Å	Demange *et al* J. Mat. Res. 19 (2004)
O_F-Al-Cr-Fe	orthorhombic	a = 7.7 Å, b = 12.4 Å, c = 23.7 Å	Demange *et al* J. Mat. Res. 19 (2004)
β-AlCrFe	cubic	a = 18.24 Å	Demange et al. J. Mat. Res. 19 (2004)
O_3-Al-Cr-Fe	orthorhombic	a = 52.71 Å, b = 12.4 Å, c = 23.4 Å	Demange *et al* To be published
M_1	monoclinic	a = 21.2 Å, b = 12.4 Å, c = 27.8 Å, β = 98°	Demange *et al* To be published
M_{11}	monoclinic	a = 43.6 Å, b = 12.4 Å, c = 20.3 Å, b = 98°	Demange *et al* To be published

Chapter 3

Surface Science Techniques

3.1 Quasicrystal Surface Preparation

The growth of high quality centimetre sized quasicrystals, such as icosahedral *i*-Al-Pd-Mn and decagonal *d*-AlCuCo [62], enabled the possibility of surface studies on them. As growing techniques were perfected many more large volume quasicrystal samples followed , Fig. 3.1. They could be cut to reveal any chosen plane, particularly planes of rotational symmetry. This provided a way to investigate whether bulk terminations had the same quasicrystalline nature as the bulk structure. This was proved to be true as many quasicrystalline surfaces were imaged. Initial research results indicate that the bulk termination of many of these alloys are effectively perfect, two-dimensional slices through the bulk structure [10, 40].

Surface science is particularly useful in studying quasicrystals. Techniques for studying bulk structure, such as x-ray diffraction, reveal crystallographic information in reciprocal space. Most of the mathematical techniques, developed for extracting real space structural information, only work for periodic materials. A higher dimensional crystallographic methodology has now been developed, where periodicity is recovered in 6-dimensional space, to permit some modelling and comparison to data. However, some information for aperiodic materials is irretrievably lost in the reciprocal space approach. Surface science offers a more direct solution, with one of its most powerful tools, the scanning tunnelling microscope (STM), allowing quasicrystals to be studied in real space for the first time.

The first problem is how to image the surface. The cluster nature of quasicrystals, means that the bulk termination is very rough. Although the clusters can be imaged on STM [32], it is too rough to achieve atomic resolution. To achieve a flat surface which resembles the chosen symmetry

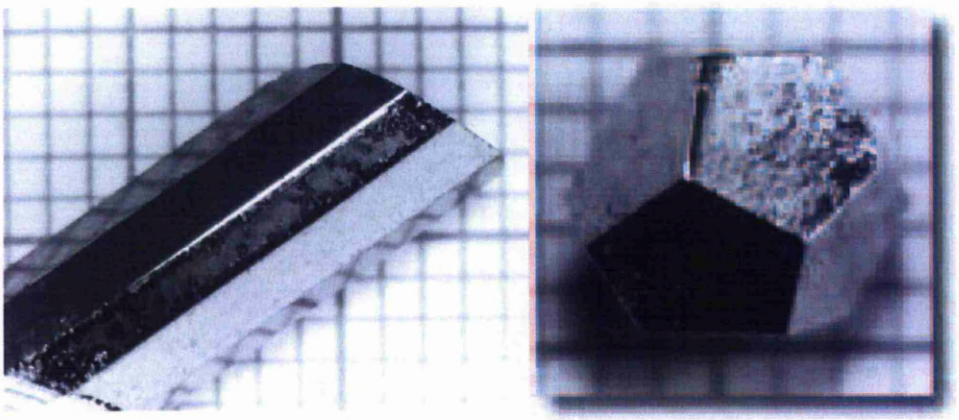

Figure 3.1: Large quasicrystals can be grown using a variety of growing techniques. **Left** - Al-Ni-Co Decagonal 2D quasicrystal. Grown using the flux growth technique, giving a large single grain, very well-ordered, strain-free, and show no evidence of secondary phases. **Right** - Ho-Mg-Zn icosahedral quasicrystal. Grown by using the self-flux method (excess Mg), and slowly cooling from 700°C to 480°C, the RE-Mg-Zn family is the first rare-earth containing quasicrystal structure, which allows the study of localized magnetic moments in a quasiperiodic environment. Images from Ames Lab, Iowa.

plane in the bulk structure, at least a layer of clusters needs to be destroyed and rearranged. This is done by first polishing the surface with diamond paste, in successively smaller grades. At Liverpool University the preparation procedure involves successive polishing using 6μm, 1μm, and $1/4\mu$m diamond paste, giving a good quality surface. The sample is then placed in a UHV chamber for the next stage, where the surface is sputtered. An inert gas, such as Argon or Helium, is ionised and accelerated towards the surface, typically with 500-1500V. The ions bombard the surface, removing the top layers of atoms. These include both the quasicrystal constituent elements, and also any surface contaminants, such as oxygen or CO. These contaminants adsorb upon exposure to air, and prevent the STM imaging the actual quasicrystal surface. This still happens in a vacuum, but the extremely low pressure reached in UHV, typically 10^{-10} mbar, means that a sample can stay clean for at least 8 hours before one monolayer forms on the surface.

After sputtering, the sample is annealed to allow the surface to reorder itself. The sample is raised to a high temperature, typically 2/3 of the bulk melting temperature. This temperature is chosen because it is estimated to be the surface melting temperature, based on the fact that the surface atoms

have lower coordination, and can therefore escape the lattice with less energy. This allows the 'melted' surface to reorder, but the bulk retains its quasicrystal structure. When the quasicrystal is cooled the surface then follows the pattern of the underlying bulk plane. The process of sputter/annealing is repeated several times to achieve a perfect quasicrystalline surface. The actual anneal temperature and duration is specific to each sample.

The correct preparation conditions are crucial to ensure that the surface is still quasicrystalline. The main difficulty is that most quasicrystals are made of three different elements. Lighter elements sputter preferentially due to the mechanics of energy and momentum transfer from the fixed mass projectile, changing the surface composition [63]. If the surface composition is different from the bulk it can restructure to a different phase. With Al-Pd-Mn, for example, Al sputters preferentially, followed by Mn, then Pd, as they have relative atomic masses of 27, 55, 106 respectively. Different elemental vapour pressures causes atoms to evaporate away at different rates during annealing. Using the Al-Pd-Mn example again, at 370°K the Mn concentration decreases due to thermal desorption; at 620°K Al concentration decreases due to thermal desorption; at 670°K Mn concentration increases due to diffusion from bulk; at 820°K Al concentration increases due to diffusion from bulk, and/or Pd concentration decreases due to thermal desorption. Above 860°K a cubic Al-Pd alloy is formed. Initially the surface appearance is shiny and metallic after cleaving. It becomes matt after annealing, due to interference effects as surface terraces grow to sizes comparable with visible light. If the cubic phase is formed it becomes shiny and metallic again.

The combined effect means that the preparation process itself can actually destroy the quasicrystalline nature of the surface, as the surface elemental composition varies from the bulk composition. However, under the right conditions, the different loss rates coincide, and a true quasicrystalline surface can be made, with the same composition as the bulk. The ratio of these elements can be checked using techniques such as Auger electron spectroscopy (AES), which reveals elemental surface composition.

3.2 LEED

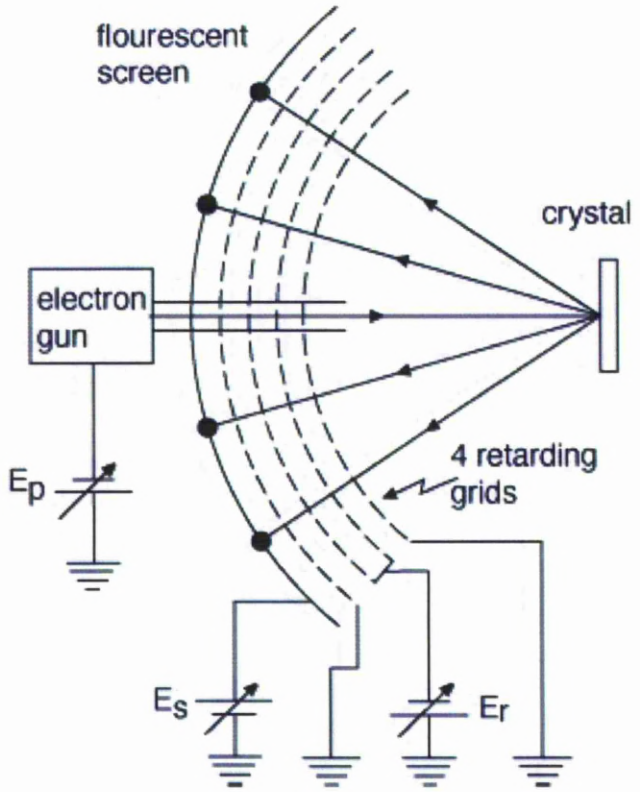

Figure 3.2: Electrons are fired at the sample and reflect back towards a fluorescent screen. The retarding voltages filter out most of the electrons, so that the image observed comes from elastically scattered electrons only. From http://whome.phys.au.dk

Low Energy Electron Diffraction uses electrons whose de Broglie wavelength is similar to atomic separations. Whereas x-rays penetrate the bulk of the sample, LEED is surface sensitive. This is because the mean free path for low energy electrons is short in solids. An electron gun fires monochromatic electrons at the sample, and some reflect back towards the fluorescent screen , Fig. 3.2. Only electrons that scatter elastically (from the surface) are allowed to hit the screen. Most electrons that are scattered inelastically (usually by penetrating the surface slightly) are stopped by a retarding voltage in front of the screen, set slightly lower than the electron gun voltage. Elastically

scattered electrons pass through the grids and are accelerated towards the screen. The data can be used in two ways. Firstly, it gives immediate information in reciprocal space about the surface order, specifically the surface symmetry and periodicities, and the quality of the surface (the sharpness of the spots indicates how well ordered the system is). The second application is quantitative structure determination, by measuring the diffraction intensities as a function of the incidence electron energy, and comparing them to multiple scattering calculations for a model system. The model is revised, mostly using educated guesses, until good agreement is achieved. This latter application is less relevant to quasicrystals, because many of the mathematical techniques developed are for periodic materials. Although, there have been a number of attempts at LEED structural solutions for quasicrystals [64,65].

3.3 STM

The Scanning Tunnelling Microscope was invented by Binnig and Rohrer at IBM in 1982. The significance of this invention was so great that they received the Nobel prize for it in 1986, and it has now become the most important tool in surface science and nanoscience. Whereas LEED only allowed a reciprocal space view of a crystal, the STM allowed a way 'to see' the atomic surface in real space. Its principle of operation is based on quantum mechanical tunnelling of electrons between the sample and an atomically sharp tip. Whereas classically electrons should not conduct across a vacuum, quantum mechanics allows them to tunnel across short distances ($\approx$1nm) when a voltage is applied. The tunnelling current (j) drops exponentially as the separation increases:

$$j = Aexp(-\phi d) \tag{3.1}$$

Whereϕ is barrier height, A is constant, d is separation.

A small change of 1Å can change the current by a factor of 10, allowing atomic resolution in the z-axis. An atomically sharp tip is moved in the x-y plane using piezoelectric crystals. These crystals have the ability to generate mechanical stress, and therefore expand, when a voltage is applied. The length of the crystal only changes by a small amount, which can be precisely controlled with the voltage. This allows the tip to be moved about in controlled steps smaller than atomic separations. An x-y raster is used to finely control the movement of the tip across the sample. The STM can be used in two modes. *Constant current* mode is the most commonly used, and gives the best resolution. A feedback loop is used to keep the current

constant, by moving the tip up and down in z. As the tip scans across the sample, the amount the tip has to move in z for each x-y position is stored. In this way, a 3D profile of the surface is built up. The STM can also be used in *constant height* mode. As the tip moves across the sample the height (z) remains constant, allowing much faster scanning speeds. The changing current allows the surface profile to be built up, using the relationship given in Equation 3.1.

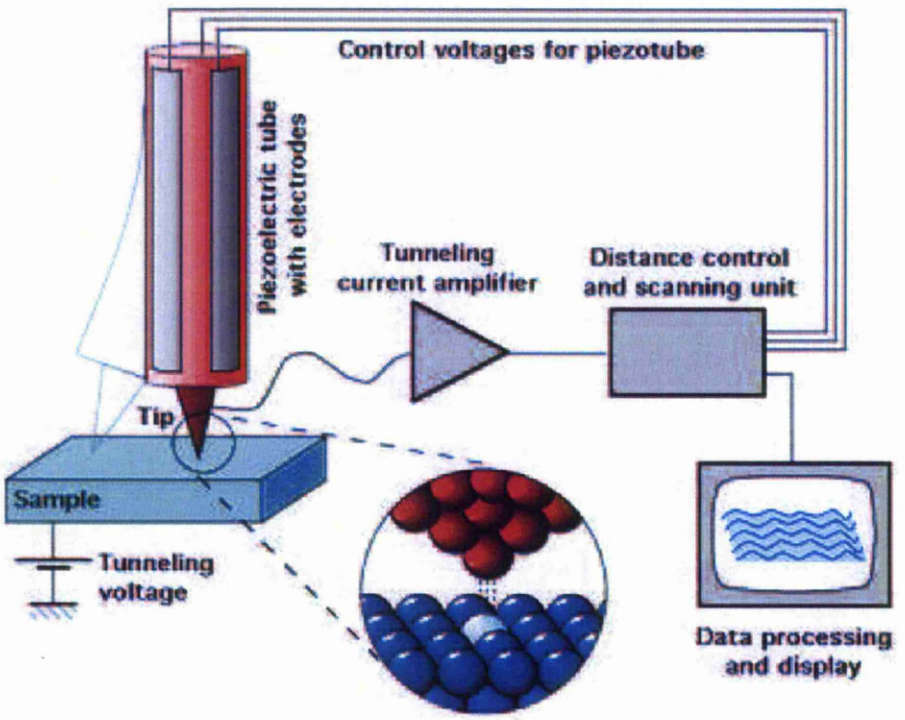

Figure 3.3: Schematic of an STM showing basic operating principles. From Institut for Allgemeine Physik TU Wien.

STM is limited to conducting (or at least semiconducting) samples. The surface must be well prepared by polishing, sputtering and annealing, under UHV conditions, in order to get a clean flat surface. To achieve atomic resolution, scanning is also done in UHV. A rough surface will make the tip crash, as it scans across and cannot move fast enough in z to prevent it hitting the surface. It must be exceptionally flat for *constant height* mode. If the surface is dirty, the tip will pick up/drop atoms/molecules as it moves across the surface. This randomly changes the conductivity and the tunnelling

distance, so the surface topography cannot be determined.

If the surface is prepared correctly, STM can achieve atomic resolution, giving a real space image of the surface. However, what is imaged is not actually atoms, but the joint Density Of States (D.O.S.) of the sample and the tip. Depending on the direction of the bias (voltage between tip and sample) the current flows in two ways. When the sample is positive relative to the tip, the current is proportional to the number of electrons leaving the tip and being accepted into available energy states nearby in the sample lattice; when negative, it is proportional to the density of electrons at a lattice position close enough to tunnel to the tip. Both methods can give different images, due to the difference in the joint D.O.S. between tip and sample at each bias.

The locations where a high D.O.S. is found, seen as the bright spots in an STM image, usually infer the position of each atom. This is because normally the regions of highest D.O.S. are found close to the atomic nuclei. Interaction between atoms can lead to overlapping wavefunctions which invalidate this assumption. A high D.O.S. can exist in-between atoms, giving rogue positions. Gaps in the D.O.S. can also exist, for example only every second atom can be seen on the surface of highly ordered pyrolytic graphite. Multi-atom samples, such as quasicrystals can be even more complex to interpret. As well as unknown overlapping effects, the change in D.O.S. between types of atoms means a direct height comparison is difficult. Despite the difficulties, the technique has proved to be the most effective way to obtain real space images of quasicrystal surfaces.

3.4 XPS

X-ray Photoelectron Spectroscopy (XPS) involves the energy analysis of electrons emitted from a surface after it has been bombarded with X-ray photons. If an electron is bound to a shell with energy E_B, the incident photon has sufficient energy hv to ionize the electronic shell if hv is greater than E_B. An electron is then ejected with kinetic energy E_K. By conservation of energy this follows Equation 3.2, neglecting the recoil of the atom.

$$E_K = hv - E_B \tag{3.2}$$

By using monochromatic incident radiation of known energy, and measuring E_K with an electron energy analyser, the binding energy can be determined. By scanning across the energy range, several peaks can be found. Figure 5.6 is a good example of of broad range survey scan. Element(s) near the sample surface can then be identified by comparing the levels observed to

calculated core level binding energies or to experimentally derived standard spectra.

The XPS chamber, used in the experiments presented in this thesis, is shown in Fig. 3.4. It has a Dual anode Al K_α source, giving as photon energy of 1487eV. These X-rays have sufficient energy for ionisation of core levels. The electrons are analysed using an electrostatic concentric hemispherical analyser (CHA). The electrons emitted from the sample surface are focused onto the entrance aperture of the analyser using cylindrical lens. Electrons of a particular energy are selected by varying the potential between the inner and outer hemisphere. As scans are being taken the potential changes in steps. While it pauses for a short time, electrons of a particular energy are focused onto the output aperture of the analyser. These electrons are then focused by output lens onto the detector. Individual electrons are counted as they arrrive, and a count rate is recorded for each channel. To achieve a good resolution scanning is repeated across the energy range several times. The counts are combined to produce the final photoelectron spectrum.

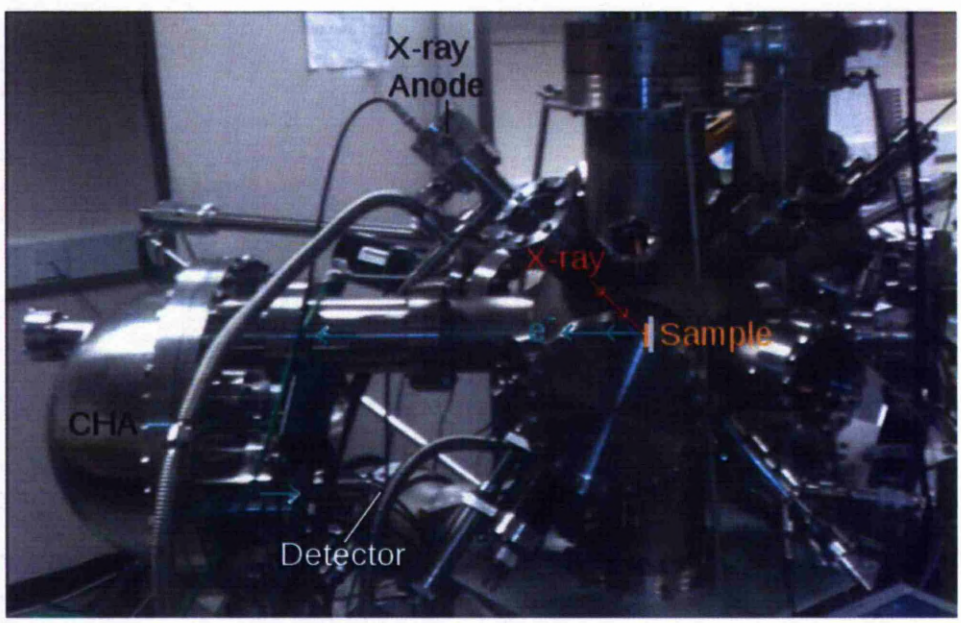

Figure 3.4: Photograph of the XPS chamber used in the experiments. The position of the X-ray source anode and the electron analyser, an electrostatic concentric hemispherical analyser (CHA), and detector are labelled. The sample is centered inside the chamber. The orientation of incoming x-rays and emitted electrons are indicated.

The width of a photoelectron peak will depend upon the intrinsic width of the level from which the photoelectron is ejected, the width of the incident radiation, and the window of the analyser. The width of incident radiation is the primary factor in our equipment, which has a resolution of 0.8-1.0eV.

The simplest way to compare peaks is to measure the peak heights, from the highest point to the background level. This method is useful for monitoring changes to a clearly defined peak, which is not convoluted with any other peak. For example, the most prominent oxygen peak is the O 1s peak between 530-533eV. By monitoring the height of this peak, and a main peak from an element in the sample, the amount of oxygen contamination can be gauged by their ratio.

When peaks are convoluted, a more detailed analysis is required to separate them. For example, the main peak in Al_4(Cr,Fe) is Al 2p peak at $\approx$73eV. The Al 2p 3/2 and Al 2p 1/2 peaks are already convoluted and indistinguishable at the resolution of the equipment (Fig. 5.7 **a**). As oxidation proceeds, electrons are transfered from the Al atoms to form the bonds with oxygen atoms, leaving Al^+ ions. This changes the potential for the remaining electrons, changing the binding energy of the electron energy levels. This is seen as a peak shift in the XPS data, with the Al 2p peak from the oxidised aluminium now seen at $\approx$75eV (Fig. 5.7 **c**). Although seperated by $\approx$2eV, the width of the peaks, seen at the resolution limit of our equipment, means that they still overlap. Therefore, to measure subtle changes in oxidation rates, the peaks are separated by modelling their shapes, and refining the model until a good fit to the data is reached. This was done with the aid of XPS analysis software called CasaXPS© [66]. The area of each peak can then be calculated, which gives a more accurate determination of the count rate from each peak, than just measuring peak heights.

The choice of lineshape to fit a peak depends on several factors. For all peaks, the intrinsic life-time broadening of the core level hole state produces a lineshape assumed to be Lorentzian in nature. However, the peaks in recorded spectra have lineshapes which deviate from this due to several instrumental and physical effects, producing Gaussian and asymmetric effects on the observed peak shape.

The standard procedure is to use a Shirley background [67] algorithm to remove the assymmetry of the peak, and therefore removing the extrinsic electrons from the data. A non-metal peak can then be fitted with a Gaussian-Lorentzian product function **GL(p)** or a Summed Gausian Lorentzian function **SGL(p)** (where **p** is the Lorentzian proportion, from 0 to 100). The proportion of each is component is altered accordingly, ranging from pure Gaussian, **SGL(0)** to pure Lorentzian, **SGL(100)**.

A metal peak has a significant additional assymetric component, due the

large amount of valence/conduction electrons, from which ejected photoelectrons scatter inelastically. These lower energy electrons are visible on the spectra as an exponentially decreasing tail on the higher binding energy side of the peak. A Doniach Sunjic Lineshape (DS) [68] is used to account for this. In CasaXPS© the **DS(a,n)** line shape is controlled with parameters **a**, the asymmetry parameter, and **n**, the convolution width. In practise, the best fit for metal peaks is a product of SGL and DS functions. See [69] for a detailed explanation of Casa XPS peak shapes and formulas.

The exact choice of lineshape for each peak can vary depending on several factors, such as background position. In metals, the amount of assymmetry taken out by the Shirley background compared to the DS lineshape can have a large effect on the measured peak area. Obtaining a best fit is not as important as producing quantification results that are meaningful for the particular situation. To compare with historical results, parameters such as FWHM may be set to be consistent with previous values. However, if the results are a sequence of experiments from which a trend is monitored, then a lineshape is chosen to best fit the whole data set.

3.5 Auger electron spectroscopy

The Auger effect was discovered in 1925 by Pierre Victor Auger. The sample surface is bombarded with low energy electrons, as with LEED, or x-rays. When an electron is knocked out from a core level of an atom, leaving a vacancy, an electron from a higher energy level falls into the vacancy, releasing a photon with an amount of energy specific to that element. Although released as a photon, the energy can also be transferred to another electron, which is ejected from the atom. The energy of this Auger electron is compared with known values of transitions between energy levels, to identify each element. The spectra of Auger electrons allows the proportions of each element to be calculated, enabling surface composition to be determined. Auger was used throughout the experiments as a tool to check for surface contamination, such as oxygen or carbon. However, XPS was used for any detailed analysis of a sample surface, as it has much greater sensitivity.

3.6 MEIS

The basic principle of ion scattering spectroscopy is to direct a beam of ions, of a known energy, towards a target material and to record the direction and energy of ions which recoil from the surface. By using the laws of conservation

of momentum and kinetic energy, the mass and position of atoms in the target material can be deduced, within the surface region. Medium Energy Ion Scattering (MEIS) typically refers to Helium or Hydrogen ions accelerated to an energy in the range of 50 KeV to 250 KeV.

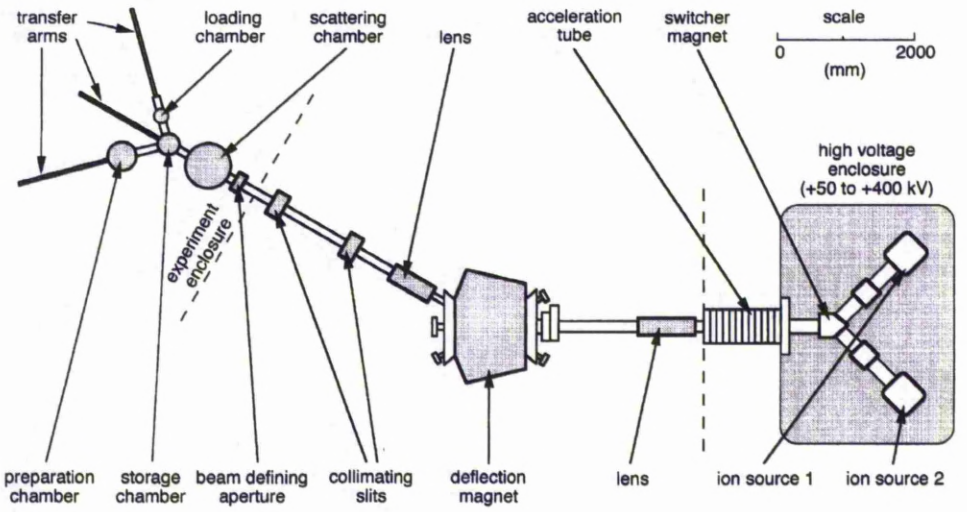

Figure 3.5: Layout of the MEIS facility at CLRC Daresbury Laboratory [70].

The MEIS facility at Daresbury Laboratory was used for the Fe/AlPdMn experiment, Chapter 8. A diagram of the setup is shown in Fig. 3.5, comprising of an accelerator, beamline and multi-chamber UHV end-station. The angle and energy of the scattered ions are determined using a toroidal electrostatic energy analyser with position-sensitive detector, Fig. 3.6. This allows the simultaneous collection of ions from a 24° range of scattering angles and with a range of energies equal to 2% of the pass energy. The raw data are thus in the form of a two-dimensional array of intensity as a function of energy and angle. The variation of backscattered ion intensity over the angular and energy range is shown by a false color map using the visible spectrum from violet to red to indicate increasing intensity.

The 2D data is manipulated using software called Midas. To understand this data 1D slices are taken for analysis. The 2D data can be sectioned to produce a 1D angle spectrum (blocking pattern) or a 1D energy spectrum. 1D energy spectra from these scans were then fitted using SIMNRA version 6.04. The energy spectra are used to calculate compositional depth profiles. The 2D data can also be processed to 'gate' a range of energies that vary with angle, so that the signal from a specific element and/or layer can be isolated from other elements or layers. The blocking dips seen in these spectra

can be attributed to known crystallographic orientations within the samples. The ratio of the intensity in blocking and non-blocking geometries (amplitude of the blocking dip) can be used as a relative measure of the degree of crystallinity within each layer [71].

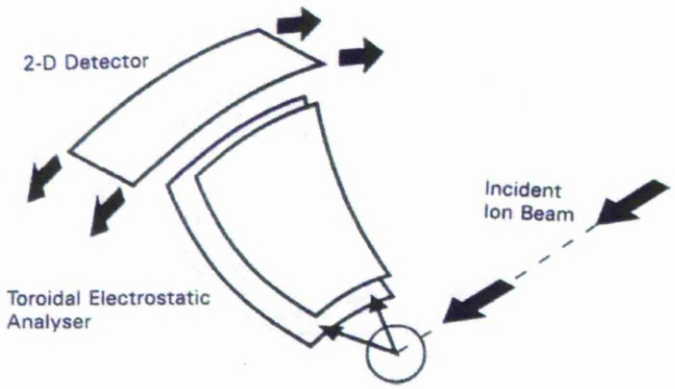

Figure 3.6: Schematic diagram of the angle-resolving toroidal-sector electrostatic ion-energy analyser and its detector [70].

Chapter 4

Surface study of the (1 0 0) and (0 1 0) faces of the decagonal quasicrystal approximant Al_4(Cr, Fe)

4.1 Introduction

The decagonal quasicrystal approximant Al_4(Cr, Fe) is a periodic complex metallic alloy (CMA). CMAs typically have large unit cells, well-defined atomic clusters, and some inherent disorder in their ideal structure. It is thought that the cluster sub-structure may give rise to interesting physical properties resulting from the competition between the different length-scales of the clusters and the unit cell [39]. There have not been many surface science studies done on periodic CMA's, as most of the work has focused on quasicrystals [40]. ξ'-Al-Pd-Mn (0 1 0) is the most researched CMA, where the main interest has been comparison with the 5-fold icosahedral *i*-Al-Pd-Mn.

A structural model for orthorhombic Al_4(Cr,Fe) was proposed [47,48] by comparing high resolution electron microscopy images with the well-known structure of μ-Al_4Mn [72]. It has since been the subject of an x-ray diffraction study by Deng et al. [46], as discussed in more detail in Section 2.5.2. The structure of the unit cell showing the (1 0 0), (0 0 1) and (0 1 0) facets is shown in Fig. 2.12. This model was refined using the x-ray diffraction data [46]. The unit cell dimensions are **a**=12.5006 nm, **b**=12.6172 nm and **c**=30.6518 nm.

Two samples, large enough for surface science experiments, were pro-

vided by Brigitta Bauer and Peter Gille, of the department für Geo- und Umweltwissen-schaften, Sektion Kristallographie, Ludwig-Maximilians Universität München. They were cut to reveal the 6-fold face (1 0 0), and the 10-fold face (0 1 0). The work published by Deng et al. [46] on the bulk structure had shown that, if the faces had bulk terminations as many quasicrystals do, the (1 0 0) face would have a pseudo 6-fold surface structure, and the (0 1 0) face would be pseudo 10-fold (see the FFTs of corresponding unit cell faces, Section 2.5.2, Fig. 2.15). The (0 1 0) face seemed particularly exciting as it could potentially show some interesting 10-fold surface structures using STM. The main aim of these experiments was to determine the preparation conditions required to achieve atomically flat surfaces, essential for UHV STM study, and to link the structure of the (1 0 0) and (0 1 0) faces to the structural model determined by x-ray diffraction [46]. However, these surfaces proved difficult to prepare for STM.

4.2 Experimental methods

The $Al_4(Cr,Fe)$ single crystals were grown by the Czochralski technique from Al-rich off-stoichiometric melts ($Al_{87}Cr_7Fe_6$ to $Al_{88}Cr_7Fe_5$) at about 1050 °C. To minimize melt surface oxidation the growth chamber was fully metal-sealed and filled with Ar at ambient pressure. Use was made of native seeds prepared from previous Czochralski experiments. The temperature of the melt is progressively decreased to maintain near-equilibrium growth conditions. The pulling rates were as low as 0.05 to 0.25 mm/h for kinetic and mass transport reasons. Precisely oriented slices were cut from the grown single crystals using a wire saw.

Two samples, with (1 0 0) and (0 1 0) faces, were then provided for UHV preparation. They were polished with 6 μm, 1 μm and 0.25 μm diamond paste to obtain a mirror-like surface, then cleaned in an ultra-sonic bath, before inserting into the UHV chamber. The typical base pressure of the system was 2×10^{-10} mbar. The samples were then sputtered and annealed under UHV. Several different preparation cycles were tried, in an effort to achieve atomic resolution with STM. LEED was used to determine the surface order.

4.3 Results and discussion

The samples proved to be very difficult to prepare. The (1 0 0) surface did eventually yield some STM data, after an extremely long set of sputter-

anneal cycles for a total duration of about 50 hours. This far exceeds the usual quasicrystal preparation cycles of 5-20 hours. The results for each surface are presented below.

4.3.1 $Al_4(Cr,Fe)(1\ 0\ 0)$

The optimum sputter-anneal preparation for this surface was found to be cycles of 45 minutes Ar ion sputtering at 500 eV followed by 5 hours annealing at 650 °C. This was repeated 8 times. After this lengthy preparation, the STM revealed a high quality surface, exhibiting step/terrace morphology over a wide length scale (Fig. 4.1(a)). The 6-fold rotational symmetry, clearly visible in these LEED images Fig. 4.1(b), is due to the hexagonal atomic arrangements on the (1 0 0) surface. The mesh of underlying spots corresponds to the 2-fold symmetry of the unit cell. The LEED patterns were of high quality, indicating that there was good long range order across the surface.

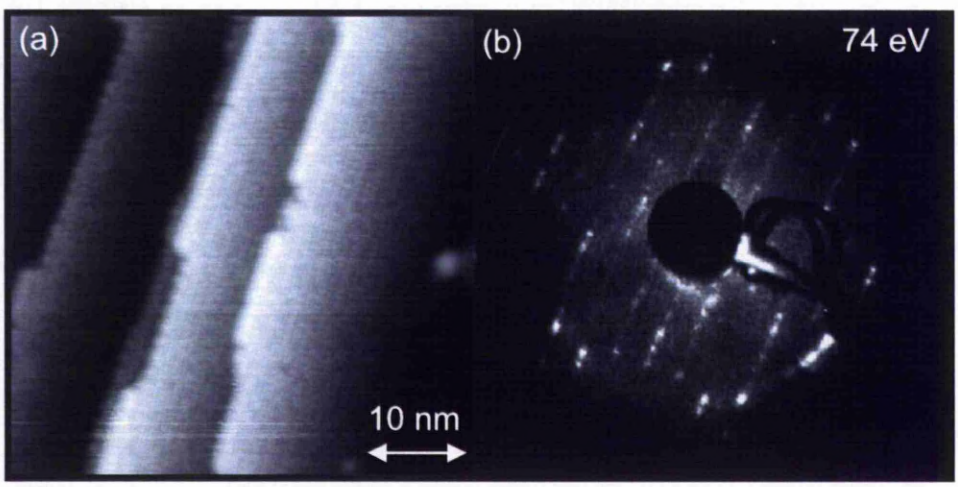

Figure 4.1: **(a)** 750 Å × 750 Å STM image of the (1 0 0) face of $Al_4(Cr,Fe)$, indicating the large terraces formed following the optimised preparation procedure. STM tunneling conditions: -1.02 V, 2.64% loop gain, scan speed 411.18 nms^{-1}, 0.635 nA feedback setpoint. **(b)** LEED pattern taken at 74 eV incident beam energy showing both the local six-fold symmetry and the underlying larger-scale two-fold symmetry of the surface.

Although the STM images were of good quality, atomic resolution was not achieved. Fig. 4.2 shows a detailed image of a smaller scan region, analogous to 'zooming in'. This is the best resolution data achieved on this surface.

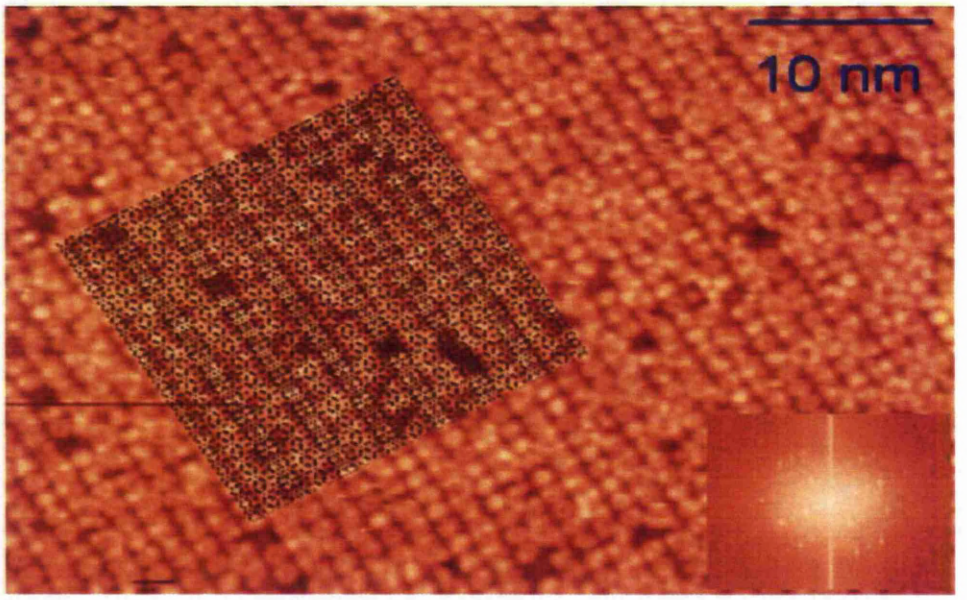

Figure 4.2: 500 × 300 Å high resolution STM image of the (1 0 0) face of $Al_4(Cr,Fe)$, clearly showing the cluster based structure in the rings of high electron probability. A 7x7 unit cell model is superimposed onto the image. Inset FFT shows the 2-fold symmetry of the unit cells. STM tunneling conditions: -1.02 V, 0.854% loop gain, scan speed 585.9 nms^{-1}, 0.39 nA feedback setpoint.

The cluster based structure is clearly visible. What appear to be bright spots on lower resolution scans can now be seen as rings. Some of these rings are broken, and some are missing. The defects show the inherent disorder in the structure, typical for approximants. No individual atoms could be distinguished within the rings, suggesting overlapping rings of localised electron cloud. This could indicate that the underlying atoms responsible for these rings are behaving as clusters, with distinct local bonding between them.

The distance between these rings is 1.5 nm in one direction, and 1.2 nm in the other, equivalent to two structures per unit cell. Without atomic resolution the location within the unit cell cannot be clearly seen in the STM data. However, comparison to a surface model of a (1 0 0) bulk termination, Fig. 4.3, reveals the most likely locations. The two positions are identified at the centre of each unit cell sized rectangle, and also marked as rings on other example positions. These two positions seem the most likely place as they are both the centre of 3 or 4 concentric rings of atoms. Exactly which

rings of atoms are visible in the STM data is unknown at this stage. From the STM images there are differences across alternate rows of rings. One row has slightly smaller well defined rings, while the next has slightly larger and more disordered rings. The larger rings often interconnect, as their diameter equals their separation. By comparison with the model, each ring type could be identified to either position. If the rings are aluminium (white atoms) then the small perfect rings are the 8 Al atom rings around position 1, and the large imperfect rings are the 12 Al atom rings around position 2. However, if the Cr/Fe content is responsible for the rings, then the positions are reversed. The small rings would then be from the ring of 6 Cr/Fe atoms surrounding 4 Cr/Fe atoms at position 2, and the large rings from the 10 Cr/Fe atoms surrounding position 1 in an imperfect circular fashion.

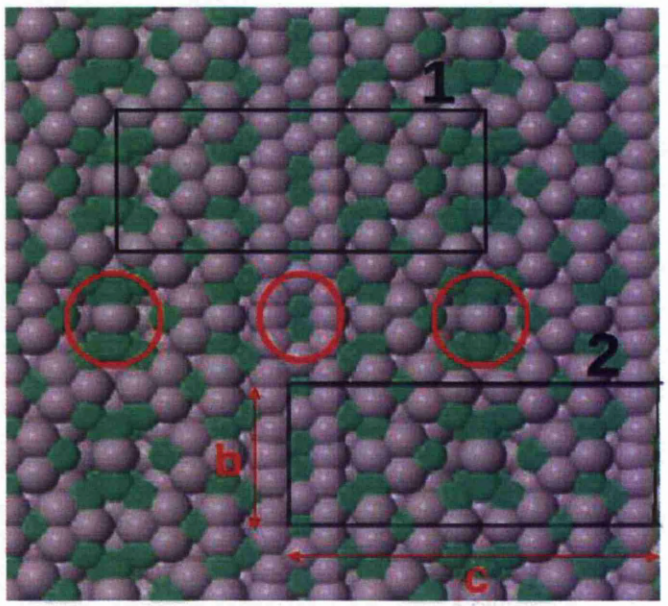

Figure 4.3: Surface model of an Al_4(Cr,Fe) (1 0 0) bulk termination, built using repeated unit cells from the x-ray determined bulk structure. 2 ring clusters per unit cell are seen in the STM images. The likely locations have been identified by each unit cell sized box, marked **1** and **2**, with dimensions $\mathbf{b} = 1.25$ nm and $\mathbf{c} = 3.05$ nm. The ring clusters centre around the centre of these boxes. Example rings are marked on identical positions across the centre of the image. The specific rings of atoms which are visible on the STM images cannot be identified from the data.

Fig. 4.4 (a) shows an STM image of a step edge. Here the individual

protrusions are clusters of atoms. A unit cell grid, overlayed on this image, shows the orientation and aspect ratio of these unit cells across two terraces. By comparison to the structural model Fig. 4.4 (b), we can see that the features seen on the STM data do correspond to the bulk terminations of the model. This model is based on a sequence of layers pfp′PFP′, where p or P indicates a puckered layer and f or F a flat layer. p′ indicates an inversion of p and PFP′ an inversion of pfp′. This indicates that there are two equivalent (1 0 0) surfaces within each cell unit, and therefore that two terminations ought to be visible in STM, each related to the other by inversion symmetry. The grid overlay on the model, clearly matches the grid overlay on the STM data. Further proof that this is the case comes from the step height, which is measured from the STM data to be 5.8 ± 0.2 Å. This is very close to the half unit cell value of 6.25 Å expected from the model. The two terminations appear to be equally favoured based the on the area coverage of alternate terraces.

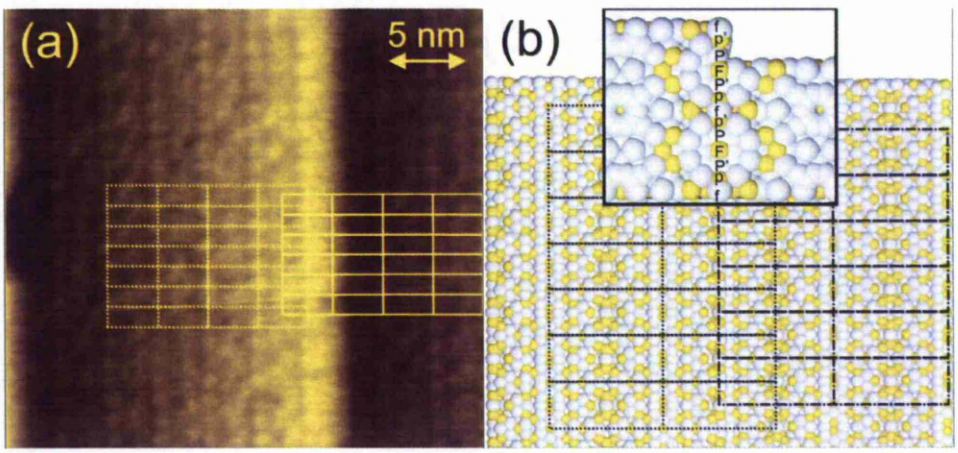

Figure 4.4: (a) 300 × 300 Å STM image of the (1 0 0) face of Al_4(Cr,Fe), showing two adjacent terraces and a step edge in more detail. The step-height as measured by STM is 5.8 ± 0.2 Å. (b) An extended part of the structural model showing corresponding surface terminations, separated by a half-unit-cell step height (6.25 Å). The model is based on a stacked sequence of flat and puckered layers, expected to terminate at either the f layer or the F layer. The inversion symmetry of adjacent terraces is demonstrated by the matching unit cell grids overlayed on (a) and (b).

4.3.2 Al_4(Cr,Fe)(0 1 0)

Several different preparation procedures were attempted for this surface. Following the most successful (1 0 0) experiments, the starting point was 8 cycles of 500 eV Ar ion sputtering followed by 5 hours annealing at 650 °C. This did not yield any successful STM results, but did give some unusual LEED patterns. The spots moved in opposite directions when the beam energy was changed, evidence of microfaceting. After several attempts on the variable temperature scanning tunnelling microscope (VT-STM), which had many other experiments running successfully, this experiment was moved onto our second chamber, the RT-STM (room temperure), for further study. This was upgraded with a Nanonis electronic control system which, as part of the procedure to help get resolution, had a line scan monitor which could compensate for the tilt of the surface. When scanning was done on a small area, of about 20 nm x 20 nm, the tilt required was in the range of 40-50°. These narrow steep planes were further evidence of microfaceting, although no atomic resolution or cluster resolution was achieved.

Similar results were found in the annealing temperature range of 460-700°C. However, there was a change seen when the temperature was lowered to 450°C; the spots on the LEED pattern stopped moving in opposite directions, suggesting microfaceting ceased. Well defined LEED patterns with sharp spots could now be seen, Fig. 4.5. The pseudo-decagonal symmetry is clearly manifested in the ten-fold rings observable in the figure, and the large unit cell is evidenced by the dense two-fold mesh. The reciprocal space vectors for these features on the LEED patterns match the real space dimensions of the corresponding features on the model from the x-ray structure solution [46].

Despite many repeated cycles no surface preparation procedure that was tried resulted in a step/terrace morphology suitable for study by STM. The microfaceted surfaces were too rough in the 460-700°C annealing temperature range. Even though there was no microfaceting in the 350-450°C temperature range, it proved to be too cool to produce a surface flat enough for STM.

4.4 Conclusions

A surface flat enough for atomic resolution was not achieved for either sample, even during experimental runs where atomic resolution was achieved on other quasicrystals. Some successful STM results, showing cluster resolution, were achieved on the (1 0 0) face. Even though STM was not very successful, the LEED results reveal that both surfaces were highly ordered; the diffrac-

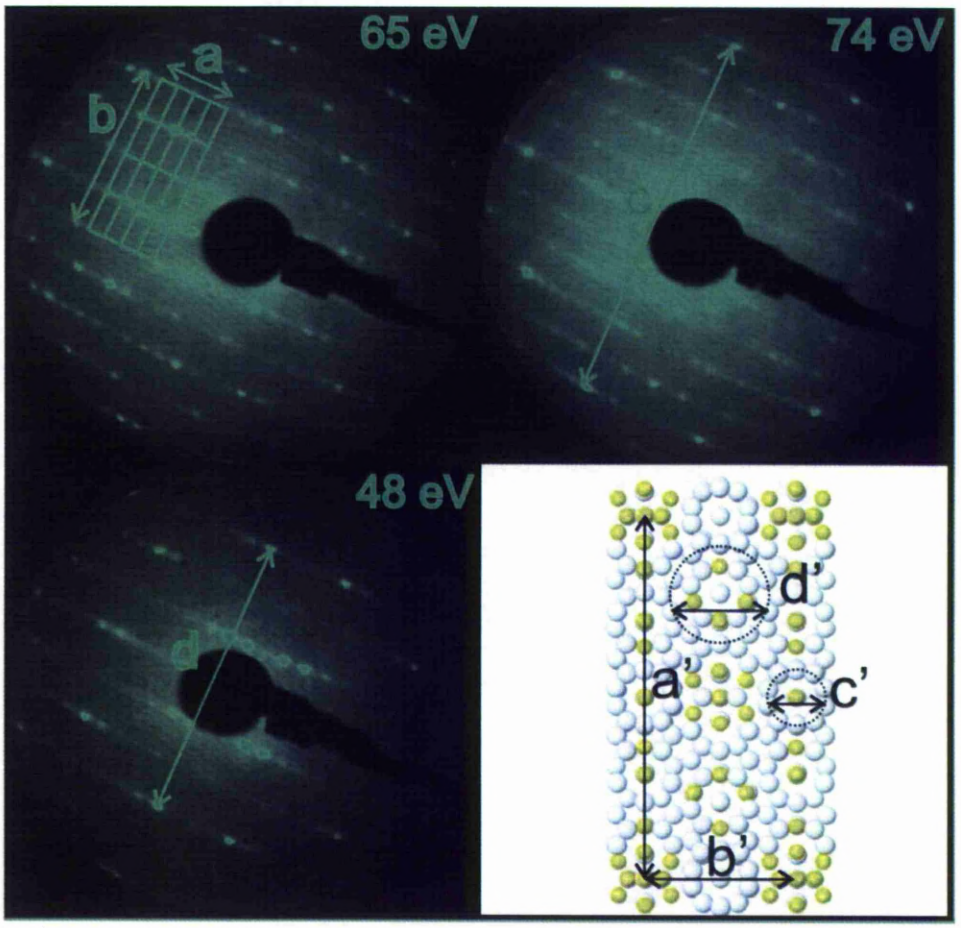

Figure 4.5: LEED patterns from the clean (0 1 0) surface at various incident beam energies showing clearly the unit cell surface mesh and the pseudo-decagonal symmetry. Certain characteristic distances are highlighted on the reciprocal space LEED images, which correspond to real space distances in the model shown bottom right. The dense mesh of underlying spots corresponds to the 2-fold symmetry of the unit cell (**a,b**). The rings of 10 spots correspond to characteristic dimensions of decagonal surface features shown on the model (**c,d**).

tion patterns revealed both the unit cell structure, and the 6-fold/10-fold structural arrangements. The symmetry of these surfaces matches that of the corresponding unit cell faces. The (1 0 0) surface is pseudo 6-fold, the (0 1 0) surface is pseudo 10-fold.

The (1 0 0) surface of the orthorhombic phase of $Al_4(Cr,Fe)$ has been studied using LEED and STM. A suitable surface preparation was found to be with repeated cycles ($\approx$8) of Ar^+ ion sputtering (45 minutes at 500eV) and annealing (5 hours at 650°C). This yields a high quality surface, with terraces large enough for STM study. This has revealed a cluster based structure, with two rings of atoms per unit cell being visible on the STM data. The most likely location of these has been identified on the model. The close match suggests the surface structure is very close to a bulk structure termination. At lower resolution the rings appear as spots. The unit cell has two terminations at the surface, which appear to be equally favoured. The step height is roughly half the unit cell height, 5.8 $\pm$ 0.2 Å from the STM data. LEED and STM results are consistent with the model proposed by Deng *et al.* [46].

Although the preparation of the (0 1 0) surface did not result in a surface suitable for STM, high-quality diffraction patterns were obtained when annealed to 450°C. The well defined LEED patterns indicate good long range order. Both the pseudo decagonal symmetry and the two fold structure of the unit cell are seen in the LEED patterns, and the dimensions match structural features of the model. This suggests that, although direct STM evidence could not be seen, the surface structure bears a very close resemblance to a bulk termination of the unit cell. Annealing to higher temperatures, from 460-700°C, produced rough surfaces with evidence of microfacetting observed in the LEED patterns and the STM calibration attempts.

Chapter 5

STM and XPS investigation of the Oxidation of the (1 0 0) surface of Al_4(Cr, Fe) quasicrystal approximant

5.1 Introduction

Quasicrystals and approximants possess useful properties such as low friction, low adhesion, high hardness and good corrosion resistance (see [73] and references therein). These properties are surface and interface phenomena. The reasons for properties such as low friction are not well understood. Many detailed STM images of their clean surfaces have been published, showing their unusual symmetries and aperiodic order. However, application in the real world rarely involves direct contact with this idealized surface as surface oxidation occurs. It is this oxide film which interacts with other surfaces, and hence dominates friction, adhesion and wear. Previous XPS studies on similar samples, such as Al-Cr-Fe, Al-Cu-Fe, Al-Cu-Fe-Cr, and Al-Pd-Mn (see [74] and references therein), have shown that oxidation results in a passivating layer of pure, or nearly pure, aluminium oxide. The aim of this work is to characterise the initial oxidation of the (1 0 0) surface of Al_4(Cr, Fe) quasicrystal approximant, using STM to see the structural changes, and XPS to see the chemical changes to each element.

5.2 Experimental methods

The sample used for this experiment was the pseudo-6-fold (1 0 0) surface of the orthorhombic $Al_4(Cr,Fe)$ approximant to the decagonal Al-Cr-Fe quasicrystal. This CMA has a large unit cell, 306.4 atoms/unit cell, and bulk composition $Al_{79.7}Cr_{15.4}Fe_{4.9}$. It is discussed in more detail in Section 2.5.2. Sample production was also discussed in Section 4.2. It was prepared for UHV by polishing with diamond paste and cleaning in an ultrasonic bath. New UHV preparation cycles were then attempted, in an effort to shorten the previous 40 hour preparation cycle. Eventually, the UHV cleaning was reduced to just 2 hours sputtering and 8 hours annealing at 650 °C. The main difference from before was that each consecutive cycle was reduced in length. The full procedure began with a 1.5 hour 2.5 KeV sputter and 4 hour anneal, then a 30 minute sputter and 2 hour anneal, followed by a lower energy 1 KeV sputter for 20 minutes and a 2 hour anneal. The logic behind this method was that the shorter sputter cycles would be just enough to remove any contaminants built up during annealing, but remove much less material from the surface. This keeps more of the benefit from one anneal cycle to the next, allowing large flat terraces to form much quicker upon the next annealing cycle. Thus an STM ready clean surface was prepared in about 10 hours.

During the experimenting with preparation cycles it was also found that a couple of short high temperature cycles, involving a 15 minute 3 KeV sputter and a 720°C flash anneal, could produce a high quality surface with an excellent LEED pattern. Cluster resolution was occasionally achieved with STM, but the resolution was quickly lost and replaced with noise. The surface was very rough, and the terraces too small for good STM imaging. Overall, despite producing a highly ordered surface, it was not suitable for this STM experiment, which required consistent STM data for the duration of the whole oxidation period. Annealing for longer times at this high temperature destroyed the surface order.

The clean surface was imaged using an Omicron RT-STM1 with Matrix control software, and determined to be clean and oxygen free using XPS with Dual anode Al K_α source, and a resolution of 0.8-1.0eV. For all results, the XPS was set to the following parameters: HV = 10KV, 12.4mA, i_{Fil} = 2.53A, Emis = 10mA, multiplier = 1.68. When the STM was producing consistent good quality images, oxidation commenced. High purity Oxygen was admitted to the chamber, with the rate being adjusted to maintain a dynamic equilibrium pressure, initially of 3.5 x 10^{-9}mbar, later increased to 1.3 x 10^{-8} mbar. A mass spectrometer was used to check the purity of the gas. Thus oxygen was continually dosed while scanning with the STM. The

STM images were time logged, allowing the oxygen dose to be calculated for each. This dose is measured in units of Langmuir, found by multiplying the pressure of the gas by the time of exposure (Equation 5.1). Thus, at constant temperature it is proportional to the total oxygen flux hitting the surface.

$$1Langmuir = 1x10^{-6}Torr for 1second = 1x10^{-8}torr for 100seconds \quad (5.1)$$

XPS data could not be taken simultaneously with STM data, so the sample was moved to the adjacent chamber and the experiment repeated as closely as possible. The oxidised sample was cleaned by sputtering and annealing, until a clean surface was determined with XPS, by taking survey scans until no contaminents like carbon or oxygen were seen. XPS parameters were set to a pass energy of 50eV, dwell time of 0.3s and a step size of 1eV for the survey scans. The energy range for each scan was then chosen to focus on the most prominent peak identified for each element. The XPS parameters were then changed to produce more detail, using a pass energy of 10eV, dwell time of 0.2s and a step size of 0.05eV. Oxidation was then repeated in stages, measuring the pressure and duration to calculate each oxygen dose. After each oxygen exposure the chamber was pumped down to avoid damaging the anode while XPS data was taken.

XPS scans were taken at several intervals in the 0 to 30 Langmuir oxidation range. As only minimal changes were seen after these small increases in oxygen dose, only the 0 and 30 Langmuir data sets are presented, corresponding to the initial and final stages shown in the STM results. The sample was later exposed to air at 10^{-3} mbar, for $\approx$ 30 minutes. This is a significantly higher oxidation level, equivalent to $\approx 10^6$ Langmuir. XPS data was then taken to see how this much higher dose affects the oxidation.

5.3 Results and Analysis

5.3.1 (i) STM

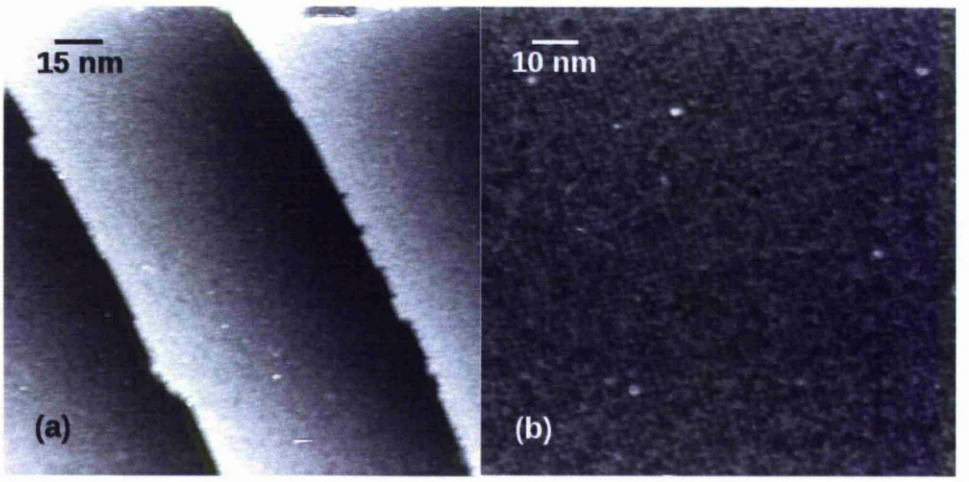

Figure 5.1: STM data from the clean (1 0 0) surface of Al_4(Cr, Fe). (a) 150 nm x 150 nm image of terraces and step edges. STM tunneling conditions: 0.9 V, 7% loop gain, XY raster 1 x 10^{-4} s, 0.5 nA feedback setpoint. (b) 100 nm x 100 nm image showing cluster resolution on a single terrace. Tunnelling conditions the same, except XY raster is 5 x 10^{-5}

The improved preparation cycle proved successful to consistently achieve cluster resolution. It reduced the preparation time from over 40 hours, to about 10 hours (2 hours sputtering and 8 hours annealing). Fig. 5.1 shows selected images of the clean surface. Reasonably large terraces are formed, with rough step edges. The surface looks almost identical to the images from the previous experiment, Fig. 4.1, proof that the shorter preparation cycle had been successful. Atomic resolution remained elusive, as the same level of cluster resolution was achieved. The cluster structure is clearly seen when zoomed in onto one terrace, Fig. 5.1(b). By measuring the distances across the STM image, the bright clusters in the 2 fold pattern are found to be 1.5 nm apart in one direction, and 1.2nm apart in the other direction. Combining two of these clusters would therefore meausure 3 nm by 1.2 nm. This corresponds with the unit cell dimensions of 3.05 nm and 1.25 nm, found by x-ray diffraction [46]. So, each unit cell produces 2 bright clusters on the STM data. These are what appear as rings on the highest resolution image that was achieved previously (Fig. 4.2). Unfortunately this resolution could

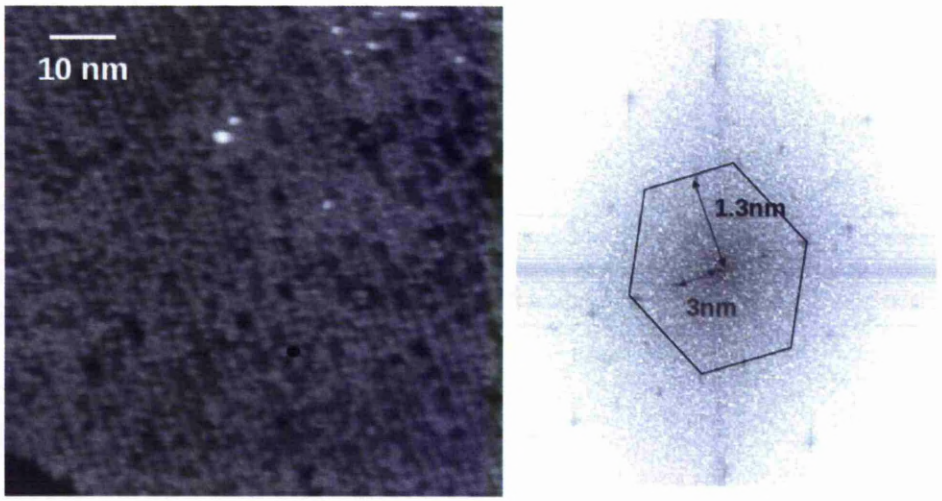

Figure 5.2: **LEFT** 75 nm x 75 nm STM data from the clean (1 0 0) surface of Al_4(Cr, Fe). The clusters are measured to be 1.5 nm apart in one direction, and 1.2 nm in the other. STM tunneling conditions: 0.9 V, 7% loop gain, XY raster 5 x 10^{-5} s, 0.5 nA feedback setpoint. **RIGHT** The FFT of this image reveals the 2-fold unit cell structure and the pseudo 6-fold hexagonal structure.

not be achieved on this experiment. The FFT of this data, Fig. 5.2, reveals the symmetry of this surface. The pseudo hexagonal arrangement of spots indicated on the FFT shows the pseudo 6-fold order. The 2-fold lattice of spots shows the periodic 2-fold unit cell structure.

Once a suitable surface was confirmed by STM, a large flat region was identified, where an area of 75 nm x 75 nm could be scanned across the surface of just one terrace. The same region was repeatedly scanned as oxidation proceeded. The results are shown as a sequence of images in Fig. 5.3. The initial stages of oxidation show that the surface is not rapidly destroyed, showing little structural change. The bright spots, attributed to two protruding clusters from each unit cell, remain for several Langmuirs. Gradually the 'fuzziness' of the image increases as oxidation progresses. At first, this just seems random, as would be expected from amorphous oxide growth, Fig. 5.3 (a) to (c). However, by comparing these to images from later stages of oxidation it is clear that this is not completely disordered. After 9 Langmuir oxygen exposure, Fig. 5.3 (d), the surface looks considerably stripy. Half of the protruding bright spots have joined up preferentially across the shortest distance between them (1.2nm), creating rows of atoms 3nm apart.

These rows are by no means structurally perfect, containing significant flaws, but they are visually obvious. This is also confirmed mathematically in Fig. 5.4, which shows an FFT taken from a clean surface image, and one from the 9 Langmuir oxygen exposed surface image. An FFT is a reciprocal space image, so the distance between a particular spot and the central spot is proportional

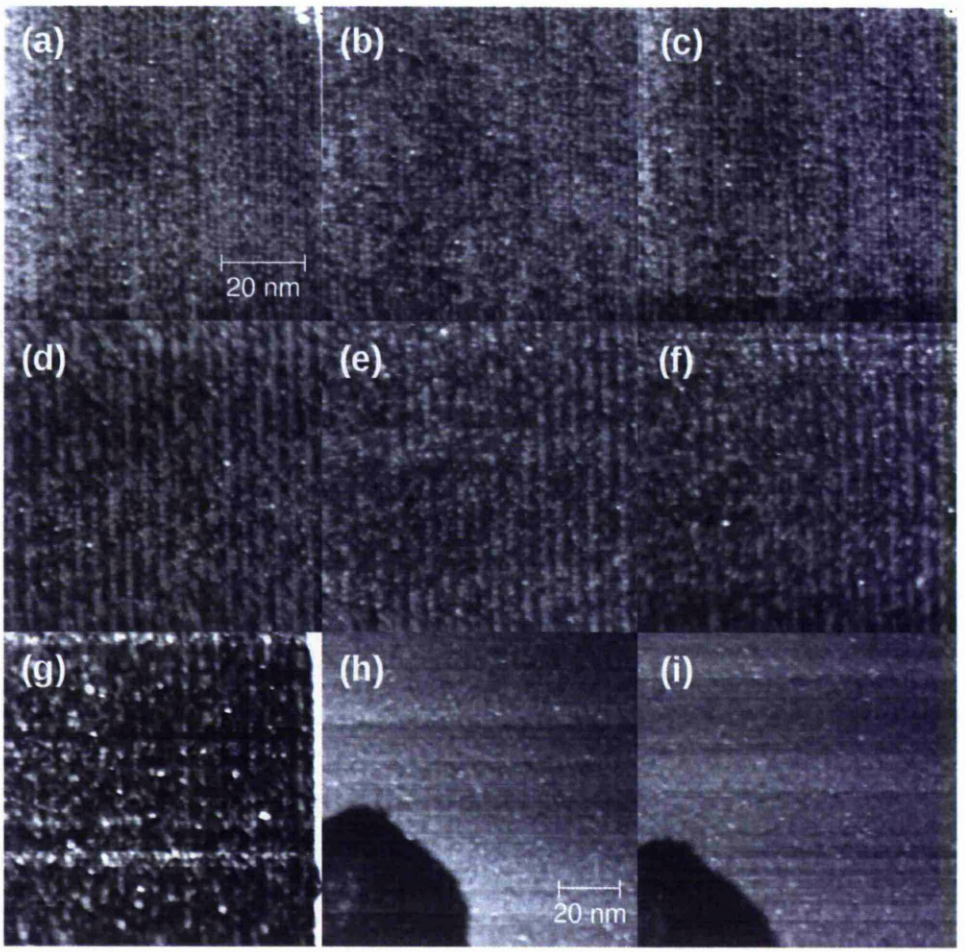

Figure 5.3: STM data progressing through stages of surface oxidation on Al_4(Cr, Fe), after exposure to increasing amounts of oxygen (measured in Langmuir): **(a)** 0L, **(b)** 0.15L, **(c)** 0.37L, **(d)** 9L, **(e)** 16L, **(f)** 18L, **(g)**21L, **(h)** 26L, and **(i)**33L. Images **(a) to (g)** are all 75 nm x 75 nm, **(h) and (i)** are 100 nm x 100 nm. STM tunneling conditions: 0.9 V, 7% loop gain, XY raster 5 x 10^{-5} s, 0.5 nA feedback setpoint.

to the inverse of the real space dimension separating the features causing the spot. This means that the largest spot separation, across the vertical in these FFT's, corresponds to the shortest real space separation in the STM image of 1.2 nm. The short horizontal separation in the FFT therefore corresponds to the 3nm unit cell separation. Evidence of a highly ordered row structure is shown by the more intense inner spots corresponding to the 3nm row separation (horizontal). 9 spots are visible horizontally across each FFT, indicated that there has been no loss of order upon oxidation across this direction. The order across the other direction, corresponding to the 1.3nm separation, is still present, but this has been reduced, as only 3 rows of spots are visible on the oxidised surface, compared to 5 rows on the clean surface.

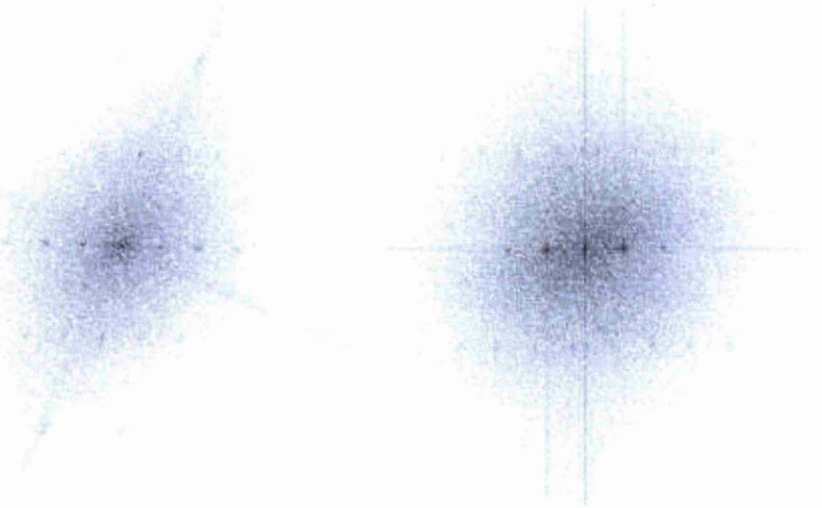

Figure 5.4: **LEFT** FFT from STM data of the clean surface of Al_4(Cr, Fe) (1 0 0). **RIGHT** FFT from STM data after 9 Langmuir oxygen exposure. The more intense inner spots correspond to the 3nm row separation.

This row structure continues to be visible until about 20 Langmuirs oxygen exposure, Fig. 5.3 (d) to (f), but the high degree of order deteriorates, and by 21 Langmuir the rows disappear. At this stage the STM starts losing resolution. Zooming out to a larger scan area allows a step edge to be seen, Fig. 5.3 (h) and (i), confirming that the STM is still working properly, and that the loss of resolution is due to increased surface roughness. At 26 Langmuir a faint hint of the vertical rows can be seen, but by 33 Langmuir this has also gone.

The enhancement of the row structure upon oxidation is evident on Fig. 5.5. Both STM images were taken under the same STM operating parame-

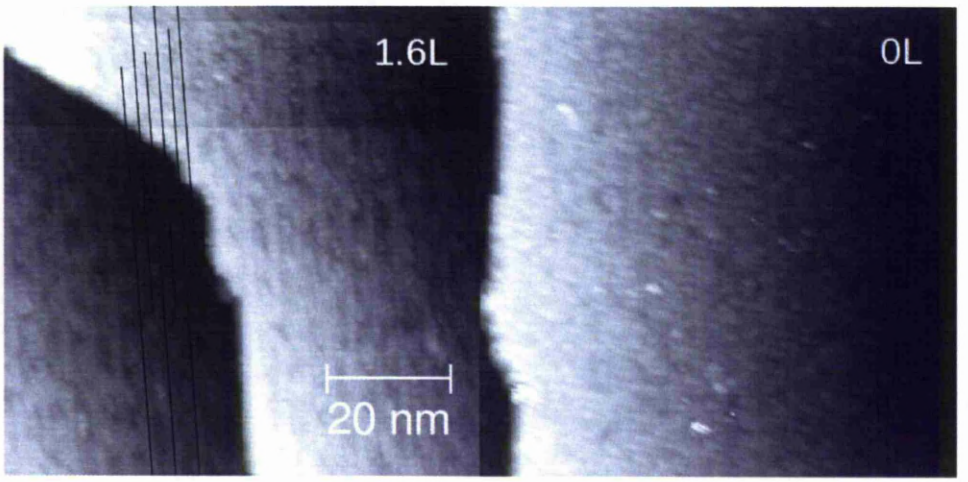

Figure 5.5: 75 nm x 75 nm STM images of Al_4(Cr, Fe) (1 0 0): **LEFT** after 1.6 Langmuir oxygen exposure, showing emphasized rows upon oxidation. The antiphase alignment of the rows on each terrace is indicated by the diagonal lines, evidence of inversion symmetry on adjacent terraces. **RIGHT** clean surface, showing no visible row structure at this scale.

ters, and no image enhancement has been performed on either image. Less detail is visible here than in Figure 5.3 because a step edge is present. The detail on the step edge is similar on both images. However, there is no row structure visible on the clean surface. As soon as oxidation begins the row structure emerges, even after just 1.6 Langmuir exposure. By comparing the alignment of these rows on each terrace, they are found to be in antiphase, further proof of the inversion symmetry of adjacent terraces expected from previous work (Section 4.3.1, Fig. 4.4, [75]). The step edge visible here is the same one that can be seen in Fig. 5.3 (h) and (i). The data shows that while the surface of the terraces changes upon oxidation, the step edges remain intact during the initial stages of oxidation.

5.3.2 (ii) XPS

An XPS survey scan of the clean surface is shown in Fig. 5.6. The surface composition is calculated from this data by choosing the most intense peak for each element, the $2p_{3/2}$ peak, and comparing the ratio of the RSF (relative sensitivity factor) corrected peak areas. The values used for the RSF are

the Scofield cross sections from the default Casa XPS library. They are calculated using Hartree-Fock theory. The values used in this analysis are: Al2p = 0.5371, $Cr2p_{3/2}$ = 7.69, $Fe2p_{3/2}$ = 10.82. The RSF value used for Al2p is for the combined area of the $Al2p_{3/2}$ and $Al2p_{1/2}$ components, which are not resolved in this data. The data shows a surface composition of $Al_{85.3}Cr_{11.5}Fe_{3.2}$. This surface is Al rich compared to the bulk composition of $Al_{79.7}Cr_{15.4}Fe_{4.9}$.

XPS scans focusing on the main peaks for each element, are presented in Figure 5.7. Peak fitting was done using Casa XPS, software designed for XPS data manipulation . Many different line shapes can be used. The exact peak

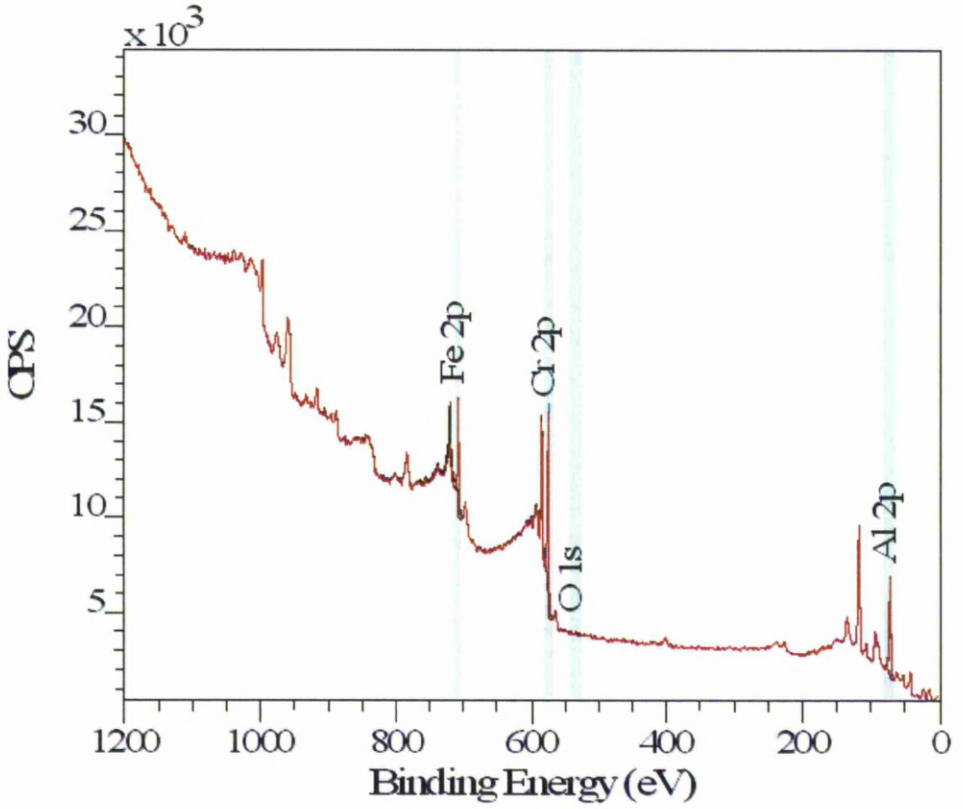

Figure 5.6: XPS survey scan of the Al_4(Cr, Fe) (1 0 0) clean surface. The strongest peaks are marked for each element, corresponding to the 2p levels for each metal, and the 1s level for oxygen. Apart from trace elements, such as Ar seen at 400eV, embedded during the sputtering process, all other peaks correspond to different electron energy levels from these same elements.

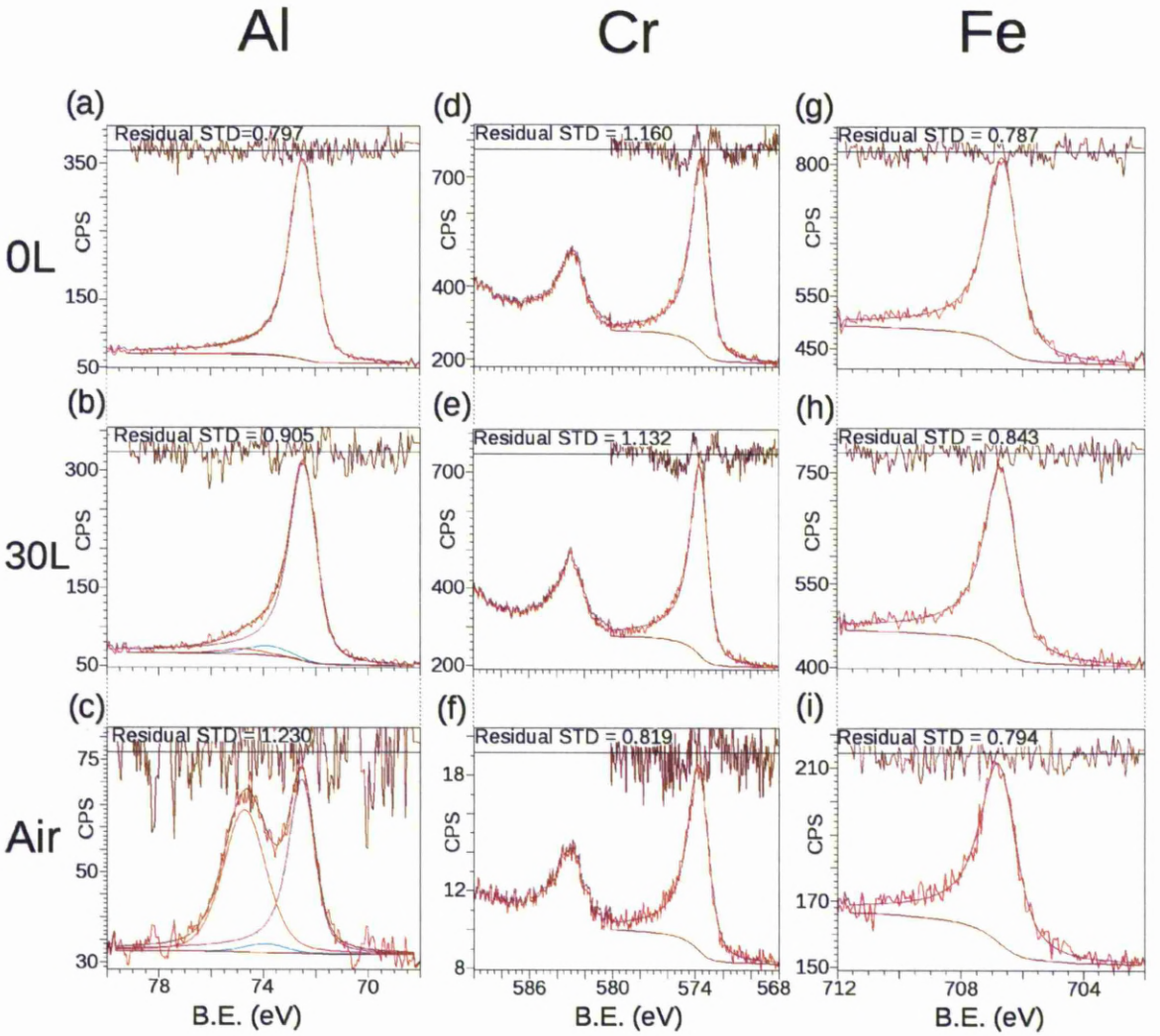

Figure 5.7: XPS scans of Al_4(Cr, Fe) (1 0 0), showing the peak fitting done using Casa XPS software. The left column is Al, after oxygen exposure of (**a**) 0L, (**b**) 30L and (**c**) exposure to air at 10^{-3} mb. The middle column is Cr after (**d**) 0L, (**e**) 30L and (**f**) air. The right column is Fe after (**g**) 0L, (**h**) 30L and (**i**) air. XPS parameters: Pass energy = 10eV, Dwell time = 0.2s, Step size = 0.05eV. The residual standard deviation is also included on each, showing the difference between the actual data and the fitted model. A STD less than 1 is an excellent fit. The red line is the data, and the lineshapes used for each peak are coloured purple for Al 2p, Cr $2p_{3/2}$, Fe $2p_{3/2}$. The main Al oxide peak grows at ≈75eV (red) upon oxidation, and a smaller peak is also found at ≈74eV (blue).

type and shape to use for the fitting of this data was altered and refined over the course of several different experiments, on two different machines. Only then was a formula found that would fit all data, where only the FWHM had to be altered in order to fit data from different machines. The main factor influencing the peak shape for metals is due to the conduction electrons in a metal. Core electrons emitted at the energy of the main peak lose energy as they pass through the material, caused by interaction with the free electrons in the conduction band, to which energy can be dissipated in a non-quantised manner. This results in a decreasing exponential tail visible on the higher binding energy side of the peak. A Doniac-Sunjic (DS) line shape is used to account for this. However, this shape is altered by the Gaussian and Lorentzian components introduced by the equipment. To account for this, the DS line shape formula is multiplied by a summed Gaussian Lorentzian (SGL) component.

The Al 2p peak was fitted using the Casa XPS line shape formula DS(0.047,125)SGL(60). The position of the Al 2p peak found here is 72.5 eV, is very close to the literature value for the pure metal 72.7 eV. The $2p_{1/2}$ and $2p_{3/2}$ contributions are unresolved. Al shows a shoulder on the higher binding energy side of 2p peak. The peak at 74.7eV, shifted by 2.2eV, which grows as oxidation proceeds, is identified as an aluminium oxide. Oxides are normally found on the higher B.E. side of the main peak when oxidising pure aluminium. Typical values are 73.7-74.1 eV for various forms of Al_2O_3, and 74.2-74.3 for hydroxy-oxides [74, 76]. Larger peak shifts, of 2.6 [77] to 2.8eV [78], are seen in the initial stages of oxidation of the the Al(1 1 1) surface. The oxidised Al peak has a different shape to the metallic peak. Aluminium oxide is not metallic and forms on the surface, so the electrons emitted are not inelastically scattered to the same extent as in a metal. Therefore it can be fitted by using only an SGL component. The Casa XPS line shape formula is SGL(30). Although not clearly resolved here, a third smaller peak is also present, convoluted with the two main peaks. It is located around 74eV. This has previously been identified as a second oxide peak, caused by Al ions located at the metal/oxide interface, on pure Al [79], and on AlCrFe [80]. However, the Cr 3s peak is also found at 74.4eV [81]. In this case the peak is a combination of both. As these cannot be resolved individually, one peak is used to account for them both, with an SGL(30) line shape.

The Cr $2p_{3/2}$ peak is fitted with the Casa XPS formula DS(0.049,35)SGL(50). It is found at 573.7eV, shifted down by 0.5eV from the position found in the pure metal of 574.2eV [82]. Oxidised states show a peak shift in the opposite direction, with Cr(III) found at 575.1-579.6eV, and Cr(IV) found at 579.5eV. As a peak shift to a higher binding energy is due

to the atom losing an electron upon oxidation, leaving it positively charged, the shift to a lower binding energy indicates the opposite, that the Cr atoms in the approximant are negatively charged. As oxidation proceeds, the peak shapes and positions remain constant, and only the signal intensity reduces in amplitude. This shows that Cr is not oxidised.

The Fe $2p_{3/2}$ peak is fitted with the Casa XPS formula DS(0.07,100)SGL(91), and found at 706.7eV. A recently published result gives the pure metallic $Fe2p_{3/2}$ peak as 706.6eV, Fe(II) as 708.2eV and Fe(III) as 710.4eV [83]. This indicates that the Fe in this approximant is in the same chemical state as in the pure metal. As with Cr, the peak shape and position remain constant, with only the amplitude reducing upon oxidation. Therefore Fe is not oxidised. As only Al is oxidised, the reduction of the Cr and Fe peak amplitude can be attributed to the signal attenuation through the aluminium oxide layer.

5.3.3 (iii) XPS Comparative Results

XPS scans within the range of the STM experiment, are compared in Fig. 5.8. The data from the 30 Langmuir oxygen exposed surface is overlayed onto the clean surface data. The data sets are normalised at the position shown, chosen to match the background levels on the lower binding energy side of the peak. The other side of the peak cannot be used as this varies when the peak amplitude changes, due to the metallic exponential tail described in Section 5.3.2.

The Al 2p Peak has changed, although not considerably. The metallic $2p_{3/2}$ peak has reduced slightly, and a shoulder is growing on the higher binding energy side of the peak. This is the first indication of the oxidised Al 2p peak. As it is so small, the exact shape and position cannot be determined from this data alone. Both Cr and Fe overlay almost identically, with only a slight reduction in amplitude, showing that neither element has been oxidised at this exposure level.

The clean surface data is then compared to the heavily oxidised surface, after exposure to air for $\approx 10^6$ Langmuir (Fig. 5.9). Even after this long exposure, there is still no change in peak shape or position for Cr and Fe, showing that neither element is oxidised. The amplitude of these peaks is now significantly reduced, due to signal attenuation through a thicker aluminium oxide layer than before. However, Al shows a significant change. Whereas the Cr and Fe peaks are reduced to roughly half the original peak height, the Al peak is reduced to about a quarter. Much of the surface Al is now

in an oxidised state. The peak on the higher binding energy side is now clearly distinguishable, and is approximately the same size as the metallic Al 2p peak. The position of this Al oxide peak can now be located more accurately. It is found to be 74.7eV.

5.4 Discussion

The improved 10 hour preparation cycle has been successful. The most likely reason for this difference is the shorter sputter cycles towards the end. The surface flattens out during annealing as the terraces grow, but, due to the high anneal temperature, the trace elements in the vacuum react with the sample after a couple of hours. The initial sputter cycles must be long because more contaminants rise from the bulk to begin with, but the sputter duration can be reduced after each cycle. A shorter sputter cycle removes less material from the surface. By using the XPS to monitor changes, the duration can be tailored so that only enough layers to remove the contaminants are sputtered away. This was possible due to the high sensitivity of XPS, when compared to our relatively insensitive Auger electron spectroscopy (AES) results. This leaves a sputtered surface that has less structural damage from the Ar^+ ions. Therefore, the terraces can reorder upon annealing much quicker than a heavily sputtered surface. The high temperature flash anneal gives the required activation energy to reorder the rough surface into terraces, and the short time minimises the effect this higher temperature has on the ratio of elements, due to the different vapour pressures of each constituent element. However, annealing at 720°C for too long destroys the clean surface as the higher temperature increases the reaction rate with the residual gas in the chamber. The longer annealing times at 650°C allow time for the terraces to grow and flatten out, while the lower temperature minimises selective evaporation and oxidation.

By combining the XPS and STM results, a clearer picture can be extracted from the previous STM data 4.2. The surface model shown in Fig. 4.3, Section 4.3.1, shows the likely locations of the centre of clusters, visible as rings on the clean surface STM data. The rings are not identical, as two types of alternate rows are seen. One row has rings that are touching, the other row has slightly smaller rings that are clearly separated. As the XPS data has shown that only Al is oxidised, and it is these rings that are oxidised, it seems likely that these are rings of Al. Therefore, the exact position of the rings can be inferred. Fig. 5.10 shows the surface model with the rings identified. The STM data has shown that the rows forming upon oxidation are seperated by 3 nm. This means that only one of the two ring clusers form

the visible rows. As they are already connected, it can be suggested that it is the orange rings that become oxidised, forming rows of Al oxide across the surface.

The formation of an aluminium oxide, favoured above chromium or iron oxide, is consistent with what is expected from the enthalpies of formation, as the energy released by forming aluminium oxide is significantly higher. The published values, at room temperature, are -1675 KJ/mol for Al_2O_3, -1140 KJ/mol for Cr_2O_3, and -824.2 KJ/mol for Fe_2O_3 [84]. This means that if any isolated Fe or Cr atom were to oxidise, it would be energetically favourable for the oxygen to then bond with the adjacent Al atom.

stm100cluster

5.5 Conclusion

The STM data indicates that the initial oxidation is highly ordered. Oxygen preferentially adsorbs onto the surface of terraces, and step edges remain intact. The STM images show ordered rows of atoms after oxidation. By comparison of adjacent terraces, these rows reveal the inversion symmetry expected from previous work [46, 75]. The XPS data shows that only Al is oxidized, with at least 2 oxidation states needed for fitting. The Cr and Fe peaks remain unchanged. The oxidation of Al, rather than Cr or Fe, is consistent with the enthalpies of formation for each oxide. Peak shapes and positions have been identified for each constituent element. The rows visible on the STM images are determined to be aluminium oxide from the XPS data. The exact position of this peak does not match any published data for a particular form of aluminium oxide, suggesting the oxide grown on this approximant has a different structure to normal aluminium oxides, or is a combination of several stoichiometries. By combining XPS and STM results, the position of the cluster rings, visible on the clean surface STM data, can now been inferred. New preparation cycles have also been identified. A high quality surface, suitable for STM can be prepared in 10 hours, by using sputter cycles with diminishing lengths. A very short cycle, where the sample is flash-annealed to 720°C, produces a high quality surface with an excellent LEED pattern, but not suitable for STM.

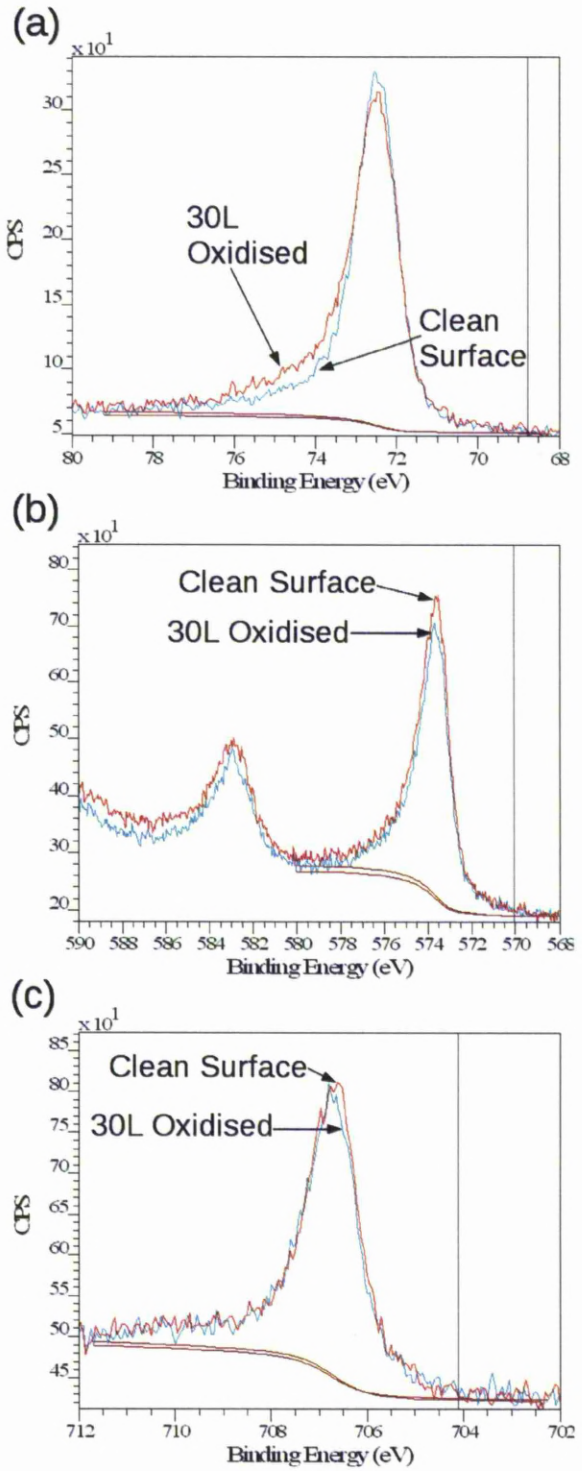

Figure 5.8: XPS scans of Al_4(Cr, Fe) (1 0 0), focusing on the (a) Al 2p, (b) Cr 2p and (c) Fe 2p peaks. Data from the 30 Langmuir exposed surface (blue) is overlayed onto the clean surface data (red). The vertical line on each graph shows the position were the two data sets are normalized to each other. A Shirley type background is shown, normally used for metallic peaks.

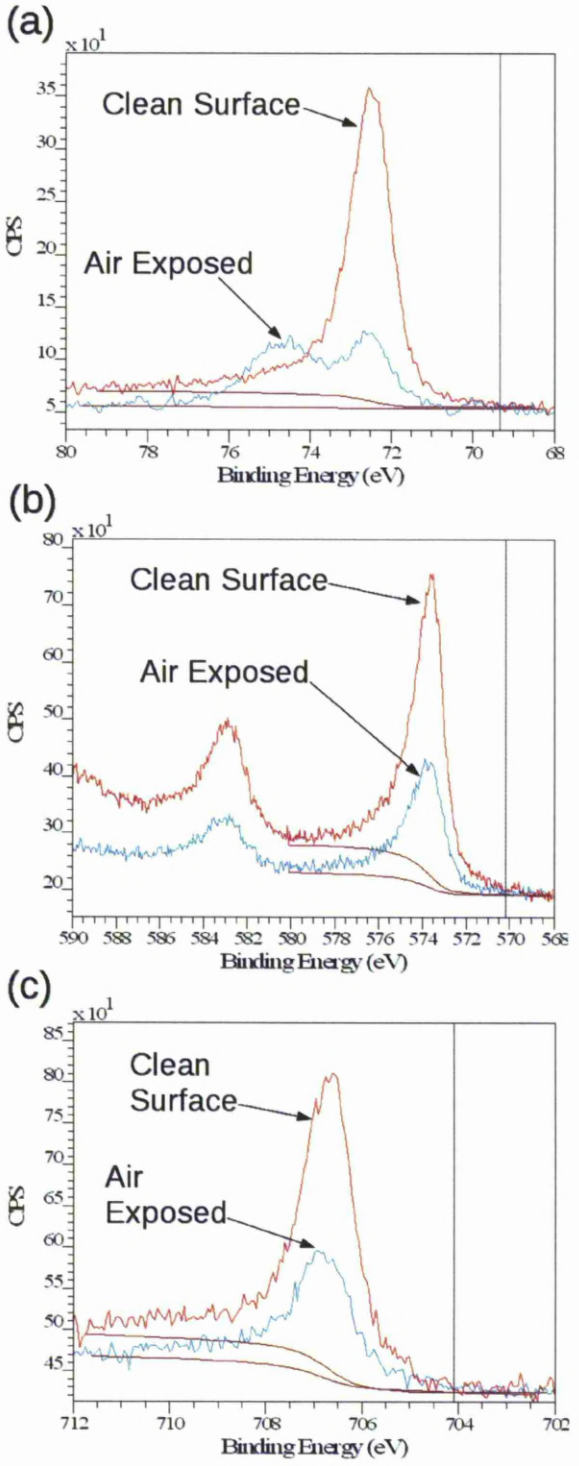

Figure 5.9: XPS scans of Al_4(Cr, Fe) (1 0 0), showing the Al 2p, Cr 2p and Fe 2p peaks. The data after exposure to air at 10^{-3} mbar (blue) is overlayed onto the clean surface data (red).

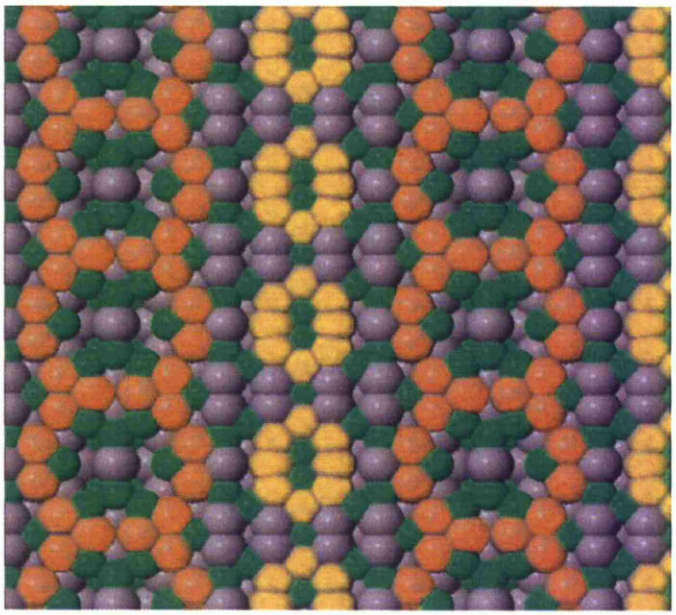

Figure 5.10: Surface model showing the rings of atoms on the Al_4(Cr,Fe) (1 0 0) surface model that have been identified, by combining the STM and XPS results, as the rings visible in the STM images. The smaller well defined Al rings are highlighted yellow, and the larger imperfect Al rings are orange. Atoms that are not seen on the STM images are grey for Al, and green for Cr/Fe.

Chapter 6

Oxide film thickness on the (1 0 0), (0 1 0) and (0 0 1) faces of Al_4(Cr, Fe) quasicrystal approximant determined by XPS

6.1 Introduction

As an extension to the XPS results in Chapter 5, an oxidation experiment was performed on the same Al_4(Cr, Fe) approximant, using XPS to compare the oxidation rates of the 3 major surfaces, (1 0 0), (0 1 0) and (0 0 1), to see how surface structure affects oxidation. Preliminary results had indicated that the (0 0 1) surface had significantly higher oxidation resistance. Examination of the structural model indicated that layers of high Cr density may be the reason for this (discussed further in Section 6.2). This warrented further investigation, as it offered the possibility of gaining the corrosion resistance of a high Cr content material, without the cost of a high overall Cr content.

Aluminium is remarkable for its low density and ability to resist corrosion due to the phenomenon of passivation. Passivation is the spontaneous formation of a hard non-reactive surface film that inhibits further corrosion. Metallic Al is very reactive with atmospheric oxygen, and a thin passivation layer of aluminium oxide (4 nm thickness) forms in about 100 picoseconds (at 1 ATM) on any exposed Al surface [85], effectively preventing further oxidation. This corrosion resistance is also often greatly reduced when many aqueous salts are present, particularly in the presence of dissimilar metals.

Aluminium may be protected further by anodizing, an electrolytic process used to increase the thickness of the natural oxide layer on the surface. The alumina generated by anodising is typically amorphous.

Aluminium oxide, Al_2O_3, is polymorphic, but occurs naturally as corundum (α-aluminium oxide). Its hardness makes it suitable for use as an abrasive and as a component in cutting tools. As a gemstone, sapphire, its hardness is only exceeded by diamond, boron nitride and silicon carbide. It is almost insoluble in water. Aluminium oxide is an electrical insulator but has a relatively high thermal conductivity (40 Wm^1K^1) for a ceramic material. Alumina also exists in other phases, namely η, χ, γ, δ and θ aluminas [86]. Each has a unique crystal structure and properties.

A major factor explaining the high oxidation resistance of Al based materials is the mass density of the passivating layer. Al_2O_3 has a density of 3.95-4.1 gcm^{-3}, 20% higher than the AlCrFe approximant, 3.43 gcm^{-3}. So the dense Al_2O_3 film acts as a physical barrier to incoming oxygen atoms. This can be quantised further by looking at the definition of a passivating layer. In 1923 Pilling and Bedworth [87] suggested that metals can be classed into two categories: those which form protective oxides, and those which cannot. They ascribed the protectiveness of the oxide to the volume which the oxide takes in comparison to the volume of the metal which is used to produce this oxide in a corrosion process in dry air. The Pilling-Bedworth ratio (P-B ratio) is the ratio of the volume of the elementary cell of a metal oxide to the volume of the elementary cell of the corresponding metal (from which the oxide is created). On the basis of the P-B ratio, it can be judged if the metal is likely to passivate in dry air by creation of a protective oxide layer. The oxide layer would be unprotective if the ratio is less than unity because the film that forms on the metal surface is porous and/or cracked. Conversely, the metals with the ratio higher than 1 tend to be protective because they form an effective barrier that prevents the gas from further oxidizing the metal [88]. The P-B ratio is defined in Equation 6.1, where R_{PB} is the Pilling-Bedworth ratio, M the atomic or molecular mass, n the number of atoms of metal per one molecule of the oxide, density, and V the molar volume. From this equation, the R_{PB} for Al_2O_3 on this Al-Cr-Fe approximant is 2.71, even higher that that of Al ($R_{PB} = 2.54$). This is calculated using the bulk properties determined by Deng [46].

$$R_{PB} = V_{oxide}/V_{metal} = M_{oxide}M_{metal}/nM_{metal}\rho_{oxide} \tag{6.1}$$

Chromating is the application of a Cr based conversion coating, applied to passivate metals such as Al [89]. The process uses various toxic Cr compounds which may include hexavalent Cr [90]. The industry is developing

less toxic alternatives in order to comply with substance restriction legislation such as RoHS [91]. It is commonly used on Al alloy parts in the aircraft industry. where it is often called chemical film, or the well known brand name Alodine [92]. Coating thickness vary from a few nanometers to a few micrometers thick [93]. The composition of Cr conversion solutions varies widely depending on the material to be coated and the desired effect. Iridite 14-2, a chromate conversion coating for aluminium, contains chromium(IV) oxide barium nitrate and sodium silico fluoride. Stacked passivation techniques are often used for protecting aluminium. For example, chromating is often used as a sealant to a previously-anodized surface, to increase resistance to salt-water exposure of Al parts by nearly a factor of 2 versus simply relying on anodizing. The oxidation resistance of this approximant is therefore of particular interest due to its chromium content.

Several preliminary oxidation experiments were performed, collecting a large volume of XPS data. The results had shown that only Al is oxidised, as was the case with the (1 0 0) surface discussed previously in Chapter 5. However, comparison to some preliminary results taken at Liverpool University on the (1 0 0) and (0 1 0) surface, and some taken at Universit Paris Sud, Orsay, on the (0 0 1) surface indicated a significant difference in oxidation rates. It suggested that the (0 0 1) surface had significantly higher oxidation resistance than the other surfaces.

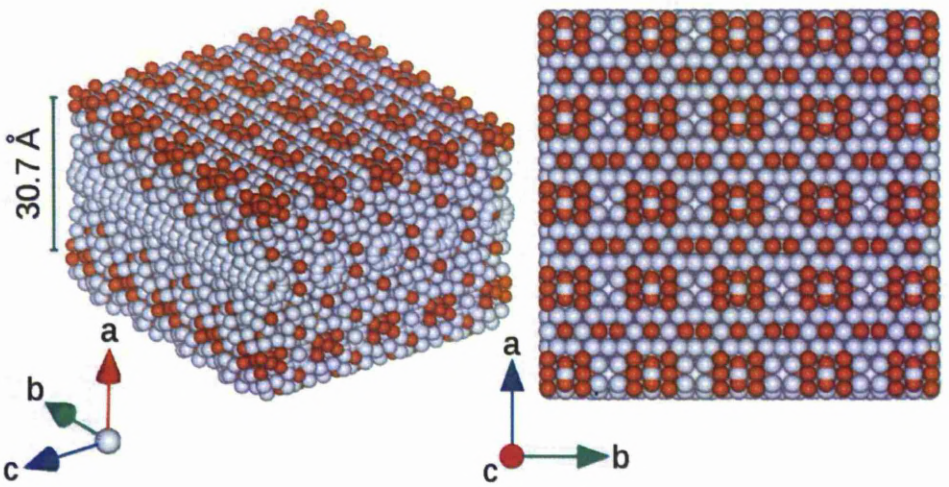

Figure 6.1: By removing layers from the (0 0 1) surface, a surface termination is reached where the Cr/Fe content is exceptionally high. From the 3-D view, the 2 atom thick Cr/Fe rich bands are clearly visible, seperated by the unit cell length.

The structural model was carefully examined to look for an explanation as to why this oxidation resistance would occur. The unit cell is 30.7 A deep (looking into the (0 0 1) surface), so initial oxide thicknesss of 2,6 and 10 A correspond to a fraction of a unit cell. Although our sample doesnt have particularly high chromium content ($\approx$ 15%), by removing layers from the model, certain terminations are reached were the density of Cr and Fe are exceptionally high. The surface shown in Fig.6.1 has double the Cr/Fe content compared to the bulk. A recent study of Al-Cr-Fe alloys [74] has found that the oxidation resistance is enhanced by increasing the Cr content. It is therefore possible that the high Cr/Fe content layer acts as a 'barrier', limiting/preventing oxygen diffusion into the bulk and/or Al diffusion out of bulk. The effectiveness of the barrier comes from the low enthalpies of formation for Cr and Fe oxide. Also, when Al_2O_3 is formed on the surface, this leaves the sub-surface region Al deficient, further increasing the Cr concentration at the hypothetical 'barrier'.

6.2 Preliminary investigation

The results from preliminary investigations are discussed in this section. Although the data is not used as part of the main experiment, its explanation is helpful to understand the development of the experimental procedure.

Analysis of the preliminary data allowed a succesful method for quantitive analysis of XPS data to be determined. As these results were taken on different chambers and at different incidence angles, the peaks on the XPS data could not be directly compared. The XPS data from each was therefore analysed in a quantitative manner, in order to extract the oxide film thickness from each. The oxidation rates of each surface could then be directly compared.

Two different methods were identified to calculate the layer thickness. The (0 0 1) data was used to work out the most suitable way. The first method uses the Beer-Lambert attenuation law (Eq. 6.2), which can be rearranged to give the thickness (z) at each stage of oxidation (Eq. 6.3). i_0 is the Al 2p metallic (73eV) peak area before any oxidation, i_z is the Al 2p metallic (73eV) peak area at the particular stage of oxidation, after being attenuated through an over-layer of thickness z, with inelastic mean free path λ, measured at an angle θ from surface normal. As the mean free path of the photoelectrons (few nm) is much smaller than that of the incident x-rays (several μm), the effect of the latter can be ignored in this approximation.

$$i_z = i_0 e^{-z\lambda Cos\theta} \tag{6.2}$$

$$z = -ln(i_z/i_0)\lambda Cos\theta \tag{6.3}$$

Based on the results it is deduced that the oxidation is forming an over-layer of Aluminium oxide. Therefore λ is chosen as the literature value for Al_2O_3. At the electron energy for the Al 2p peak, 1414eV (Source Energy 1486.6eV - Peak Energy 73eV), the NIST Database give 2 values. According to Akkerman et al. λ = 26.85 Å, whereas Chen et al. calculate it to be λ = 28.23 Å. For this thickness calculation an average value was used, making λ = 27.54 Å. For Cr 2p photoelectrons λ = 19.61 Å (average of Akkerman, 18.97 Å, and Chen, 20.25 Å), and for Fe 2p photoelectrons it is λ = 17.40 Å (average of Akkerman, 16.75 Å, and Chen, 18.04 Å).

The second method proposed by Strohmeier [94], allows the thickness of the oxide to be calculated from the ratio of the Al 2p metallic peak (73eV) and Al 2p oxidised peak (75eV). In the paper, the angle is defined as the electron take-off angle, so this formula is rearranged to match our definition of θ in Equation 6.4.

$$z = \lambda_0 Cos\theta \ln((n_m\lambda_m i_0/n_0\lambda_0 i_m) + 1) \tag{6.4}$$

Again, z is the oxide layer thickness in Å. λ_0 and λ_m are the inelastic mean free paths of the oxidic (75eV) and metallic (73eV) Al 2p photoelectrons, through the Al_2O_3 over-layer. λ_m = 27.54 Å, as with the Beer-Lambert method. λ_0 = 27.50 Å, an average of Akkerman et al. (26.81 Å) and Chen et al. (28.19). There is negligible difference between the two, as the peaks are so close together. θ is the detector angle from sample surface normal. n_m and n_0 are the atomic densities of aluminium in the metal and the oxide. n_m is calculated to be 0.0505 at./$Å^3$, using the unit cell density calculated by Deng [46], and correcting for the Al composition found in this surface region (86%). N_0 is taken as 0.043 at./$Å^3$, the literature value for γ-Al_2O_3 [74]. i_m and i_0 are the areas of the metallic (73eV) and oxidic (75eV) Al 2p peaks.

The results from the thickness calculation exercise are shown in Fig. 6.2. It is important to note that these preliminary results are only discussed as their analysis is useful for the main experiment. However there is a mistake identified in the data so the absolute thickness values should be ignored. The negligable thickness observed initially, followed by the large step increase in thickness at 5400L, was initially thought to be a property of the (0 0 1) surface. However, repeat experiments proved that below 5400L the oxygen was not hitting the sample, then it suddenly had a large oxygen dose, causing the apparent step. The experiment was of course repeated, but not scanned in this much detail, hence the reason for this discussion. This issue does not affect the ratio of Al, Cr and Fe peak areas, so the data analysis is still useful.

The Beer-Lambert method gives a lower thickness when calculated from peak areas of Cr and Fe relative to the thickness calculated from peak area of Al. This is due to an increasing signal intensity from Cr and Fe, relative to Al, as oxidation proceeds. As Al segregates from the bulk to form the Aluminium oxide on the surface, it leaves Cr and Fe rich layers underneath. This means the thickness calculated from Cr 2p and Fe 2p is under exaggerated. It also means the thickness from Al 2p peak area, is over exaggerated.

The signal intensity is also subject to fluctuations from other factors such as the x-ray source signal strength. This could vary as the X-ray source was switched off in between oxidations, and as the sample was moved between chambers for each oxidation, the angle of the sample relative to detector could only be accurate to +/-0.5 degrees. The random fluctuations across the graph in thickness calculated from peak area, are mirrored exactly for Al, Cr and Fe. Evidence that this is due to equipment related signal fluctuations, and not the oxidation changes. The fact that the Cr and Fe lines coincide almost exactly is also further evidence that only Al segregates from the bulk, as the ratio of Cr to Fe is unaffected. The actual film thickness would therefore lay inbetween the two extremes, closer to the average shown in the figure (dotted line).

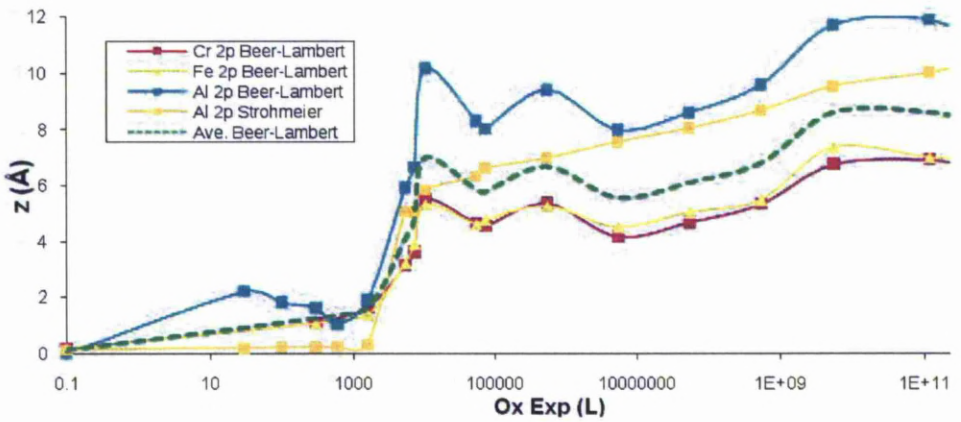

Figure 6.2: Oxide thickness curves calculated in several ways, after exposing $Al_4(Cr,Fe)$ (0 0 1) to oxygen. The top line corresponds to the thickness calculated from the peak area of the Al 2p metallic peak, using the Beer-Lambert attenuation law. The bottom two curves, which coincide, are from the Cr and Fe peak areas, again using the Beer-Lambert law. The dotted green line is an unweighted average of these 3, which is a good approximation to the thickness calculated from the Strohmeier method.

The Strohmeier method proved to be much simpler to use. The results (Fig. 6.2) show an excellent fit with no fluctuations in calculated thickness after each additional oxygen dose, as was seen when using the Beer-Lambert method. The Strohmeier method removes any errors due to random equipment fluctuations. However, it does introduce another error. The oxidised Al 2p was fitted using a Gaussian-Lorentzian (SGL) peak (non-metallic), which just includes the visible peak. The metallic Al 2p was fitted using a DS peak, which includes an exponential tail off from inelastic scattering. The area of this tail is added to the area of the visible peak to get the total Al 2p metallic peak area. This means that by using a large DS tail off, the area of the tail can be larger than the visible peak, or by using a small tail, it can be insignificant compared to the main peak. As the actual XPS data has 3 main Al 2p Peaks (metallic, oxidised, and interface) which are convoluted, it becomes possible to use a large variety of lineshapes and still achieve a reasonable fit. Hence, while the shape of the thickness curve using the Strohmeier formula is far more accurate across the range, the absolute value is less accurate. The DS lineshape was chosen by best fit to the data, not calculated. However, the close proximity of the Strohmeier curve to the average Beer-lambeth curve suggests that the Strohmeier thickness calculation is fairly accurate, and therefore the DS lineshape is correct. The Strohmeier method was therefore chosen as the preferred method to determine thickness. The data needed for the Beer-Lambert method was no longer required, reducing the total data collection and analysis time for the main experiment.

6.3 Experimental methods

The sample is an orthorhombic approximant to the decagonal phase quasicrystal, with bulk composition $Al_{79.7}Cr_{15.4}Fe_{4.9}$, grown using the Czochralski method [95]. It has a giant unit cell of 306.44 atoms with dimensions 30.5 Å x 12.5 Å x 12.5 Å, and density 3.432 gcm^{-3} [46]. The samples are cut to expose the pseudo-4-fold (0 0 1) surface, the pseudo-6-fold (1 0 0) surface, and the pseudo-10-fold (0 1 0) surface. The corresponding unit cell terminations are shown in Fig. 6.3. A 3-D model of this unit cell is also shown in Fig. 6.4. It is built from Deng's xray diffraction data [46], using VESTA (Visualization for Electronic and STructural Analysis) 3-D modelling software [96].

The experiment was carried out in an Omicron multi-technique UHV chamber, with base pressure of 2 x 10^{-10} mbar. The x-ray source is Al Kα, with a photon energy 1486.6eV. For the main experiment, all samples were studied on the same chamber, minimising any errors and differences between the data sets. Each sample was polished using diamond paste up

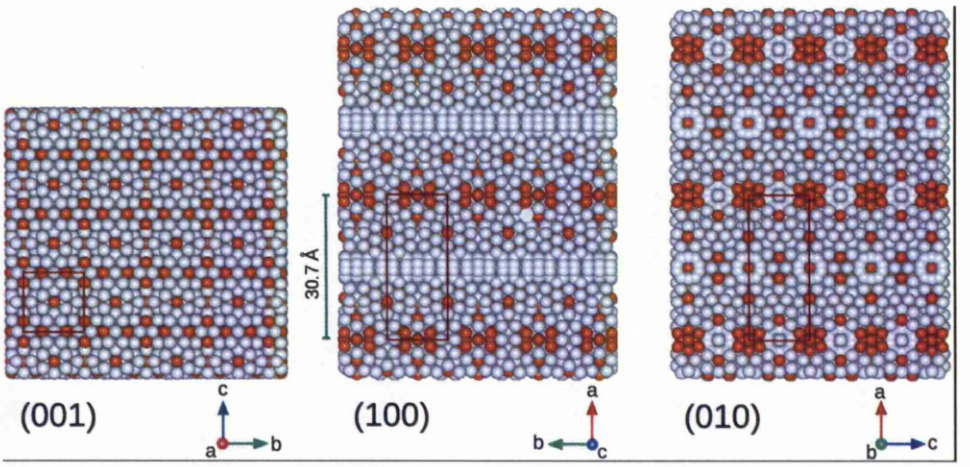

Figure 6.3: Surface models showing the major faces of the Al_4(Cr, Fe) unit cell: (0 0 1) pseudo-4-fold, (1 0 0) pseudo-6-fold, and (0 1 0) pseudo-10-fold surface. Al atoms are light grey, Cr/Fe atoms are orange. A single unit cell is indicated on each face (red box).

to 1/4 μm. The clean surface was then prepared in UHV by repeated cycles of sputtering with 2.5 KeV argon ions and annealing to 650°C, following the pattern of deceasing sputter cycle lengths described earlier (Section 5.2). XPS was used to check surface cleanliness, with the readings taken near to normal incidence (10° from sample surface normal). LEED was used to check surface quality. Each clean sample was then oxidised by admitting high purity oxygen, recording both the pressure and the exposure time, to calculate the oxygen exposure in units of Langmuirs (Equation 5.1). A mass spectrometer was used to check purity, and ensure that air was not admitted accidentally. XPS data was then taken after pumping down the chamber, focusing on the Al 2p peak, using the same parameters as in Chapter 5 (pass energy = 10eV, dwell time = 0.2s, step size = 0.05eV). To minimise error introduction, the sample was not moved in between oxygen doses and taking XPS data. The same preparation and oxidation procedure was repeated for each of the 3 samples, performed using the same equipment under the same conditions.

6.4 Results

The XPS results show that only Al is oxidised. XPS peak shapes and positions are discussed in detail in Chapter 5. As the same position and shapes

were seen, for all 3 surfaces, these results will not be presented again. The Al 2p peak shape was improved slightly, having collected a broader data range by this time. The new Casa XPS lineshape used is DS(0.03,60)SGL(20). After fitting the XPS Al 2p peaks, the film thickness was calculated for each using the Strohmeier method. The oxygen exposure versus film thickness for each surface is plotted in Fig. 6.5. Using this chamber, the oxidation levels could not be increased to the high levels seen in the previous (0 0 1) data (Fig. 6.2). But, within this range the results clearly disagree with the preliminary results.

The data shows that the film thickness on the (0 0 1) surface is almost identical to the (0 1 0) surface. The (1 0 0) film is $\approx$ 25% thinner. All surfaces show a linear increase in film thickness as the oxidation dose increases exponentially.

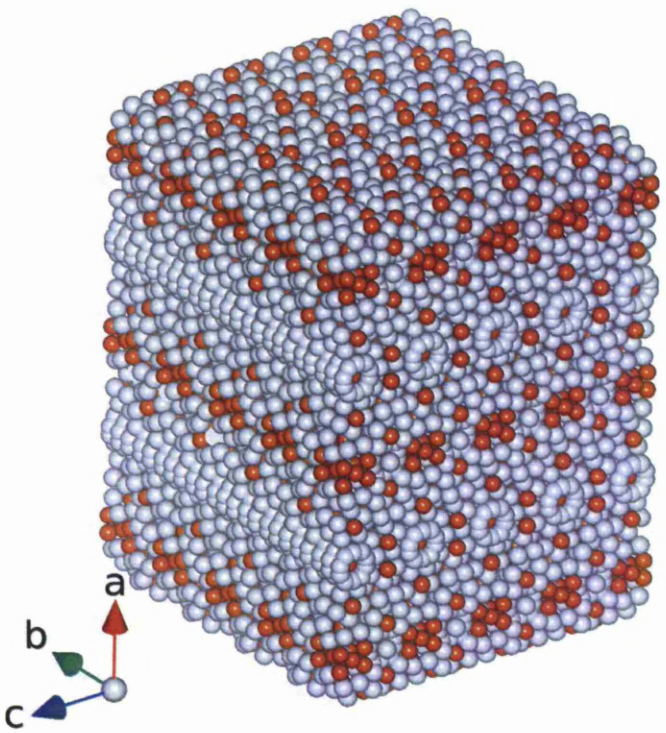

Figure 6.4: 3-D model the Al_4(Cr, Fe), built using multiple unit cells (4 x 4 x 2.5). Al atoms are light grey, Cr/Fe atoms are orange.

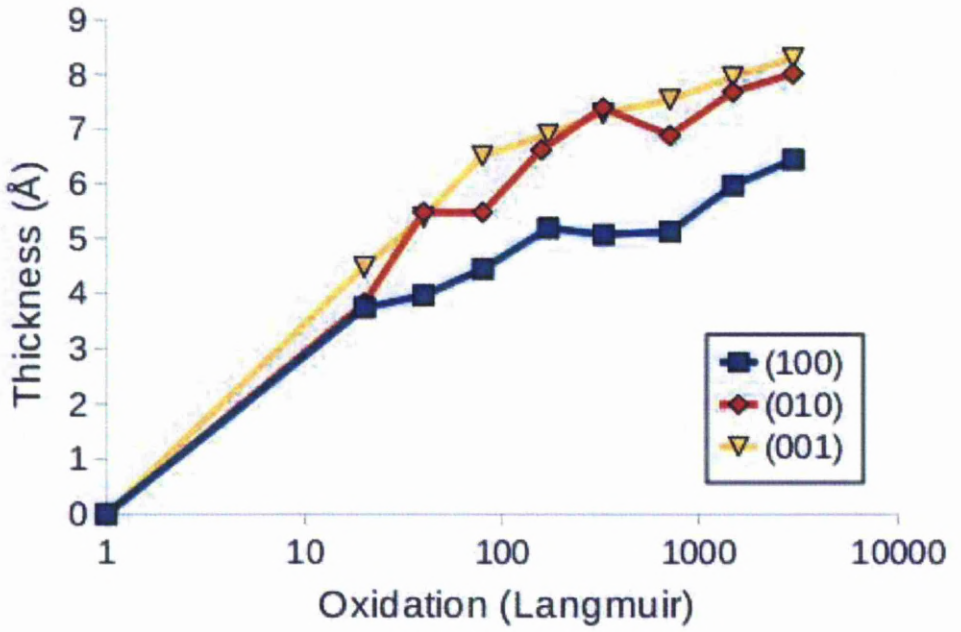

Figure 6.5: Oxygen exposure vs. Oxide film thickness, determined from XPS data, using the Strohmeier method on the Al 2p peak areas. XPS parameters: Pass energy = 10eV, Dwell time = 0.2s, Step size = -0.05eV

6.5 Discussion

Despite several attempts, the oxidation resistance of the (0 0 1) surface, seen in the preliminary run, could not be replicated. In fact, the new data (Fig. 6.5) shows that the oxide film grows at the same rate on both the (0 1 0) and (0 0 1) surfaces. This suggests that there is a problem with the preliminary data. This result means that the thin Cr rich layers within the approximant structure do not form oxidation resistant barriers. Although the (1 0 0) surface does show an increased oxygen resistance, the model does not suggest any structural reasons why this occurs, as there are no layers where the local Cr/Fe density is as high as for the (0 0 1) face.

For the (0 0 1) preliminary data the surface had been prepared differently, with a longer anneal time. The experiment was therefore repeated, with a 3 hour final anneal to replicate the same surface. The results, shown in Fig. 6.6, show that longer final anneal did not lead to a reduction in film thickness. It therefore seems likely that there is no difference between the oxidation rates of each surface, and the true film thickness is just the average

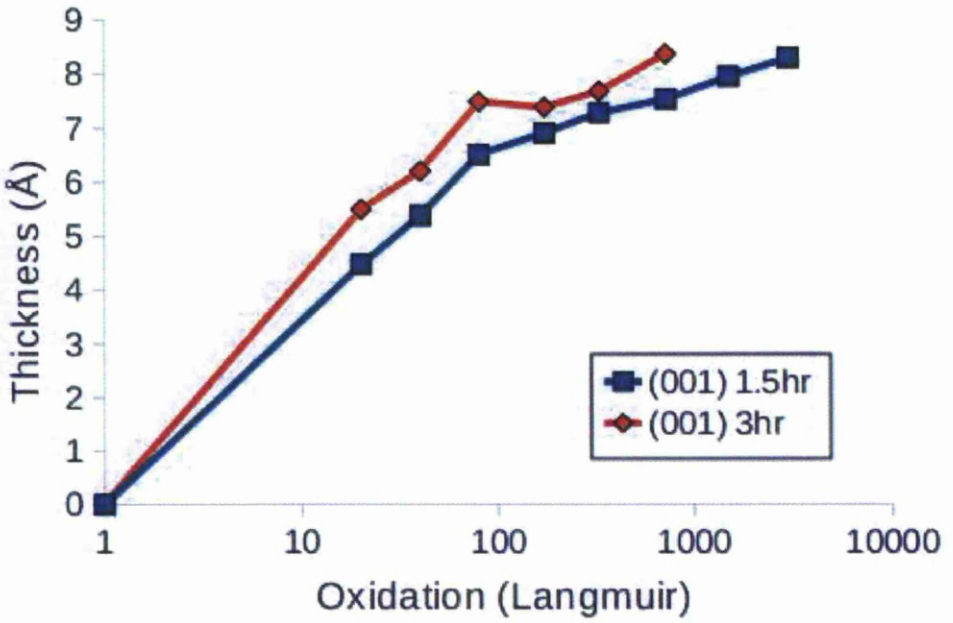

Figure 6.6: Oxygen exposure vs. Oxide film thickness, comparing oxide film growth rates after a 1.5 hour anneal, and a 3 hour anneal.

of these data sets. A best fit can be therefore be made to the data from all surfaces, shown in Fig. 6.7. Above 10 Langmuir, the film thickness increases linearly, as oxidation dose increases exponentially. The growth rate can be described with the formula used for the bestfit line, shown in Eq. 6.5, where d is the oxide thickness in Å, and L_{ox} is the oxygen dose in Langmuir.

$$d = 0.7 ln L_{ox} + 2 \tag{6.5}$$

6.6 Conclusion

The (0 1 0), (1 0 0) and (0 0 1) surfaces of the Al_4(Cr, Fe) quasicrystal approximant do not show any consistant difference in Al_2O_3 film thickness growth rates after exposure to O_2. The oxide film thickness increases linearly as oxygen exposure (in Langmuir) increases exponentially. The high Cr/Fe content layers seen in the model for the (0 0 1) surface did not increase the oxidation resistance. As this layer is only 2 atoms deep it is too thin to affect the overall oxidation rate. The Strohmeier method (Eq. 6.4) has proved to be the most successful method to determine the oxide thickness for this thin film.

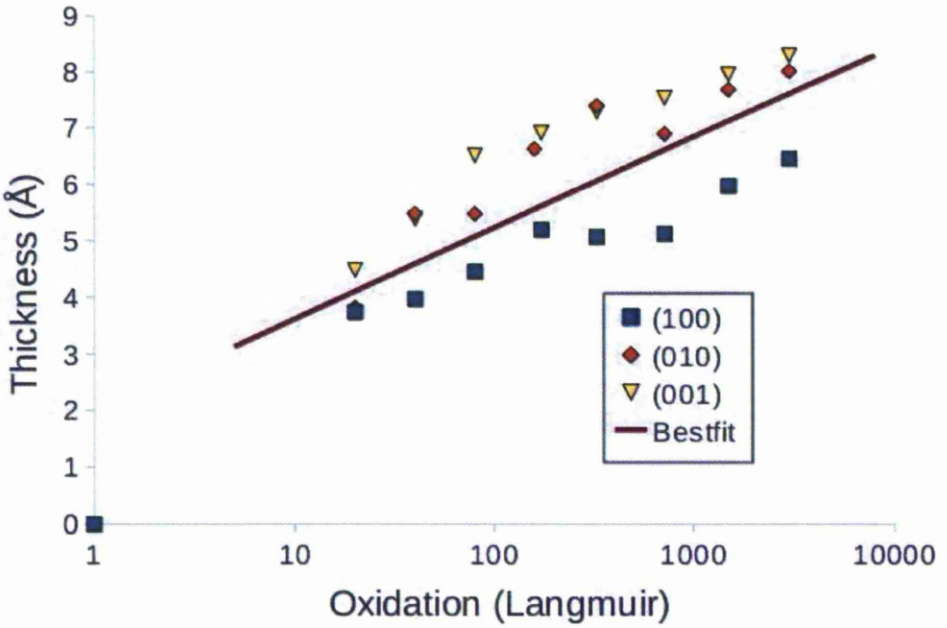

Figure 6.7: Oxygen exposure vs. Oxide film thickness, showing the bestfit to all data.

It is more accurate, being unaffected by equipment fluctuations, and requires less time to take the XPS data and perform the analysis. When Al is oxidised, Cr and Fe are either concentrated at the bulk termination underlying the oxide layer, or amalgamated into the Al_2O_3 film without oxidation. This would need MEIS data to determine conclusively.

Chapter 7

Nucleation and growth of a quasicrystalline Bi monolayer on 5-fold *i*-$Al_{70}Pd_{21}Mn_9$

7.1 Introduction

Quasicrystal surfaces have been studied extensively over the past decades, and flat surfaces can be prepared under UHV conditions with a step/terrace morphology. Several experimental and theoretical investigations have led to a consensus that apart from a small degree of relaxation, the surfaces represent bulk terminations [40, 97]. As these surfaces are therefore two dimensional aperiodic structures, they provide interesting templates for the investigation of epitaxial growth. Several experiments of this nature have been done on various quasicrystals, both icosahedral and decagonal, and various adsorbates [40, 97–99], finding single element clusters and monolayers. Experiments on *i*-Al-Pd-Mn, using low energy electron diffraction (LEED) and helium atom scattering (HAS), have shown that both Sb and Bi form ordered quasicrystalline monolayers [100]. It has also been shown with STM, that Si deposited on *i*-Al-Pd-Mn is ordered quasiperiodically at sub-monolayer coverages, and found to centre around truncated pseudo-Mackay clusters [101]. Another STM investigation has shown that Pb deposited on *i*-Al-Pd-Mn initially forms pentagonal clusters, with edge length 4.9 Å [102], at submonolayer coverage. The nucleation sites were not revealed. Further deposition leads to self-assembly of a complete quasicrystalline monolayer, through an interconnected network of these pentagons.

Theoretical calculations have also been published for Bi on Al-Pd-Mn. These could not be performed on a true model of the icosahedral surface,

which has an infinite unit cell, and would therefore require an infinite calculation time. Therefore, an approximant surface is chosen as a close representation to the surface structure, but with a finite calculation time. Krajčí and Hafner have performed *ab initio* DFT calculations of adsorption site energetics [103], and the adsorption of Bi onto these positions [103,104], using approximants to the *i*-Al-Pd-Mn quasicrystal. The 2/1, 3/2 and 5/3 approximants were simulated; periodic crystals containing 544, 2292 and 9700 atoms per unit cell respectively, and local structures similar to that of the quasicrystal. A Penrose P1 tiling of edge-length 7.76 Å was overlaid on the surface of the model as a guide to interpreting the model structure. This tiling consists of pentagons, rhombi, stars and boats [105] (Fig. 1.15). The binding energies for Bi atoms on specific adsorption sites on the surface were calculated and then used for the initial positions of Bi atoms to investigate the stability of a full Bi monolayer. The most favourable adsorption sites, in order of decreasing binding energy, were found to be at the centres of surface vacancies (-4.9eV) (which are contained within a subset of one orientation of the Penrose tiles, labelled 'bottom'); atop Mn atoms (-4.58eV) (again in the centres of a subset of the pentagonal tiles, labelled 'top'); the vertices of the P1 tiling (-4.37– -4.32 eV) and the mid-edge positions of the tiling (-3.92 eV). The number of surface vacancies and of Mn atoms was considered to be too small for the formation of a quasiperiodic framework, and therefore it was proposed that the vertices and mid-edge positions of the tiling form the skeleton of a possible stable quasiperiodic monolayer. Additional atoms form smaller pentagons inside both orientations of pentagonal tiles. By allowing relaxation of the atomic forces the stability of the proposed monolayer structure was tested and predicted to have 'pseudodecagonal symmetry'.

The aims of this experiment were to first prepare an atomically flat *i*-Al-Pd-Mn quasicrystal surface, and achieve atomic resolution, then to deposit Bi on this surface and study the growth mode using STM, to gain an insight into the growth mechanism for quasicrystalline monolayers. A crucial objective was to achieve atomic resolution on the quasicrystalline monolayer and the Bi adsorbate simultaneously.

7.2 Experimental methods

The sample, icosahedral quasicrystalline *i*-$Al_{70}Pd_{21}Mn_9$, was produced by the Ames group using the Bridgman method and cut to reveal the 5-fold surface. It is prepared by polishing with 6 μm, 1 μm and then 1/4 μm diamond paste. It is cleaned in an ultrasonic bath before insertion into the Omicron VT-STM UHV chamber, with base pressure 1×10^{-10} mbar. Then

up to 5 UHV preparation cycles, consisting of 45 minute sputtering with 3 KeV Ar^+ ions, and 4 hours annealing at 950°K using electron-beam heating, were required to achieve atomic resolution on the clean surface. Deposition was achieved by evaporating Bi from a Mo crucible, heated using an Omicron EFM-3 electron-beam evaporator, onto the sample at room temperature. The deposition rate was kept constant with a flux monitor reading of 120 nA, giving a deposition rate of approximately 1.8 ML per hour. Typical settings: filament current = 1.82A, high voltage = 362V, and emission current = 6.3mA. Coverage was estimated from STM images. The chamber pressure did not exceed 2.5×10^{-10} mbar during evaporation. STM data was taken at room temperature.

7.3 Results

After achieving atomic resolution, a clean surface with large terraces and a 5-fold quasicrystalline bulk surface termination was revealed on the STM data. Selected data showing the growth of the Bi layer is presented in Fig. 7.1. The initial growth begins with the formation of complete and incomplete pentagonal clusters, seen as the white protrusions in Fig. 7.1 (*a*). These pentagonal clusters all have the same orientation. The clusters were determined to be Bi by monitoring the surface by STM after each deposition. The Bi coverage here is calculated to be 0.13 ML (monolayer). One monolayer is equivalent to a complete single layer of atoms covering the surface. Once complete clusters were formed they did not change, indicating that they are stable. The distance between Bi atoms in each pentagon is measured by STM to be 4.9 $\pm$ 0.2 Å. The closest distance between the centres of Bi pentagons is 12.0 $\pm$ 0.2 Å. The underlying *i*-$Al_{70}Pd_{21}Mn_9$ surface is also well resolved, showing surface motifs such as dark stars and white flowers. This simultaneous resolution of both the Bi pentagons and the surface allows further analysis, discussed in Section 7.4. These features can be seen clearly in the colour enhanced image Fig. 7.2.

Upon further Bi deposition, growth continues via nucleation of these pentagonal clusters. Fig. 7.1 (*b*) shows the surface after 0.38 ML. Some resolution is lost, particularly from the underlying surface, due to the increased roughness at this higher coverage. However, the majority of the clusters can be identified complete and incomplete pentagons. This kind of growth is described as being in the *pure nucleation regime* [106], where additional deposition results in the formation of new nuclei and the island size does not change.

Above half a monolayer there is a change observed in the growth mode.

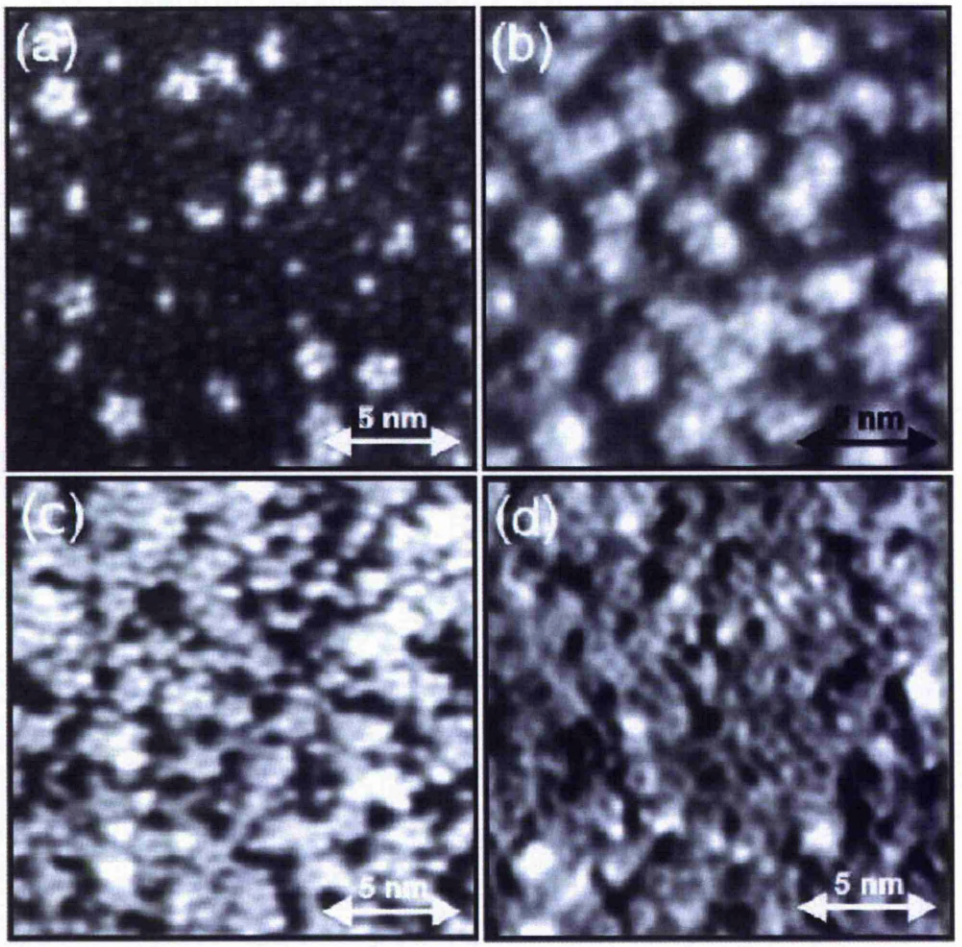

Figure 7.1: 18 x 18nm STM data showing the growth of Bi on *i*-Al-Pd-Mn after depositing: (*a*) 0.13 ML Bi; (*b*) 0.38 ML Bi; (*c*) 0.54 ML Bi; (*d*) 0.9 ML Bi. STM tunneling conditions: +1.03 V, $\approx$ 0.7% loop gain, scan speed 146.5 nms^{-1}, $\approx$ 0.9 nA feedback setpoint.

Fig. 7.1 (*c*) shows data from 0.54 ML coverage. Although individual pentagons can be distinguished, the clusters are beginning to interconnect, as Bi atoms attach onto them, joining up the space in between islands. This transition point is called the *saturation island density*, and is commonly reached at about 0.5 ML coverage [106]. It is the point at which the mean free path of the diffusing adatoms is equal to the mean island separation, therefore adatoms have a much higher probability of attaching themselves to existing

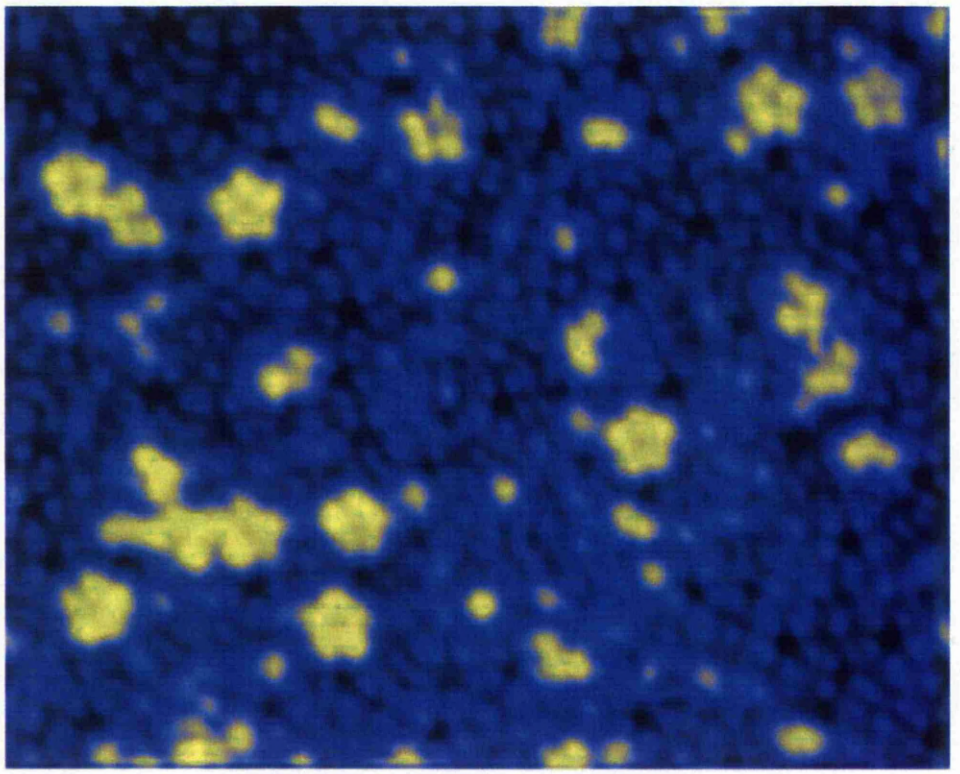

Figure 7.2: 18 x 13nm STM data after colour enhancement, showing 0.13 ML of Bi on *i*-Al-Pd-Mn. The Bi atoms are coloured yellow, and the Al-Pd-Mn surface is blue, darkening with depth. STM tunneling conditions: +1.03 V, 0.609% loop gain, scan speed 146.5 nms^{-1}, 0.915 nA feedback setpoint.

islands than creating new ones. In this case the transition can also be attributed to the fact that the majority of the preferred nucleation sites have already been taken at this coverage, leaving the space in between as the next favourable location for adatoms.

As more Bi is deposited, the STM resolution decreases further. After 0.9 ML, Fig. 7.1(d), ring-like structures can be seen. These are identified as the same pentagonal clusters, as they have the same dimensions, but the resolution is no longer good enough to distinguish the orientation and pentagonal shape. At 1 ML coverage no STM resolution was achieved at all, even though LEED measurements show a highly ordered quasiperiodic pattern. The lack of resolution is attributed to the increased surface roughness, indicated by a threefold increase in the r.m.s. z-corrugation on the STM, when compared to

the clean surface. Annealing this complete monolayer, to 580°K for 1 hour, improved the LEED pattern, consistent with the results from the previous HAS study [100]. However no better STM resolution could be achieved.

7.4 Analysis

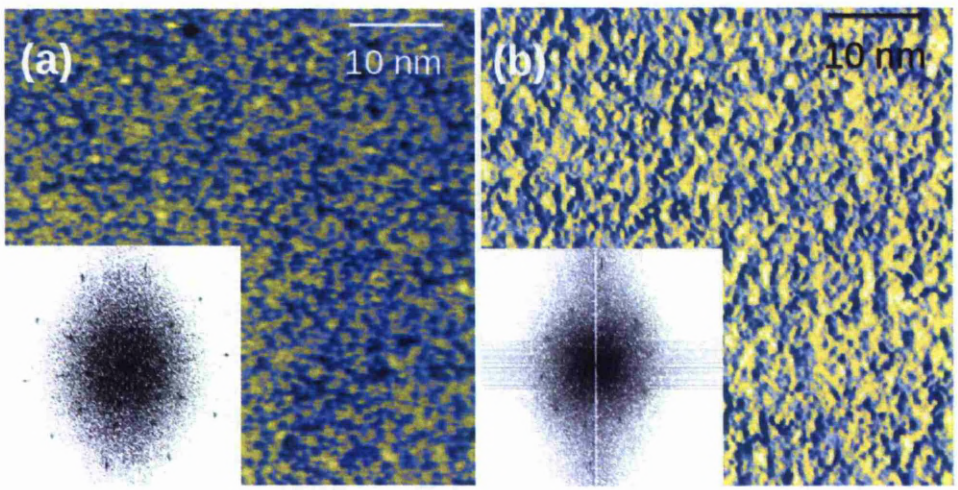

Figure 7.3: 50 nm x 50 nm STM data from Bi on *i*-Al-Pd-Mn, using the same colour enhancement as Fig. 7.2, with corresponding FFT's inset. (*a*) 0.38 ML Bi; (*b*) 0.9 ML Bi.

The small images in Fig. 7.1 are the best scale to see the surface detail, but the surface area is too small to produce a good FFT. The larger surface area shown in Fig. 7.3 provides more data to perform the calculation, but the clean surface structure is no longer resolved. Therefore the FFT corresponds to the symmetry of the Bi. At 0.38ML, Fig. 7.3 (*a*), growth is still in the pure nucleation regime, so all of the Bi is in the form of pentagonal clusters. The FFT shows a high degree of 10-fold symmetry. This means that the pentagonal Bi clusters are positioned on sites which themselves are quasiperiodically arranged. At 0.9ML, Fig. 7.3 (*b*), no order is visible in the STM image, but, although the spots are more diffuse than for the lower coverages, the FFT still shows a 10-spot ring, proving that the film is still quasiperiodically ordered.

To identify the nucleation site, the STM data is compared to the model of the 3/2 approximant surface used by Krajčí and Hafner [103]. In Fig.

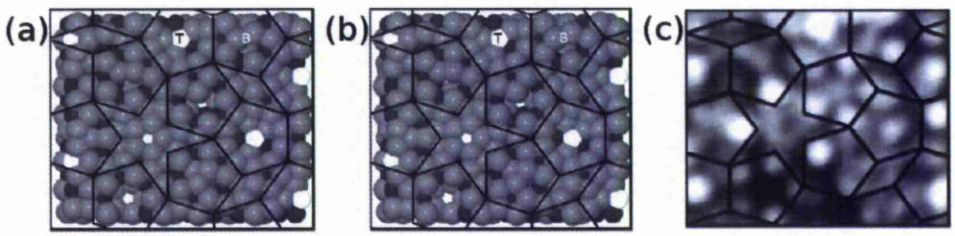

Figure 7.4: All images represent a 4 x 3.5 nm surface area. (*a*) The 3/2 approximant surface, from the DFT model [107], with a Penrose P1 tiling superimposed, of edge length 7.76 Å. Al atoms are shaded light grey, Pd atoms are dark grey, and Mn atoms are white. Bergman clusters are centered at the vertices of the tiling. Mackay clusters are centered in the centre of pentagonal tiles. The two possible orientations are labelled 'T' and 'B', for 'top' and 'bottom'. 'Top' pentagons contain a Mn atom centered in the surface plane, and are the centre of the white flower motifs. 'Bottom' pentagons sometimes contain 5-fold hollows, known as 'dark stars'. (*b*) Simulated STM image of the same *i*-Al-Pd-Mn surface region, reproduced from [108]. (*c*) A selected region from clean surface STM data, which closely matches the simulated STM data in (*b*).

7.4(a), a Penrose P1 tiling of edge-length 7.8 Å is superimposed onto a section of the 3/2 approximant surface. The bulk structure of the *i*-Al-Pd-Mn quasicrystal can be interpreted as being composed of pseudo-Mackay (M) and Bergman (B) clusters [109]. B clusters are centred on the vertices of the tiling, although not every vertex corresponds to such a cluster as the minimum distance between them in the bulk is 7.76 Å. The pentagons of the P1 tiling encompass the M clusters, which have a Mn atom at their centre. There are two different cuts through M clusters, each corresponding to the two different orientations of surface pentagons. Tiles labelled 'top' are cut with the Mn atom in the top layer, hence a Mn atom is present in the surface layer. Tiles labelled 'bottom' are cut higher up the cluster, leaving the central Mn atom 2.56 Å below the surface. Adjacent 'top' and 'bottom' pentagons always share an edge, with a distance between centres of 10.73 Å. Adjacent pentagonal tiles of the same orientation can only share a vertex; the distance between their centres is 12.62 Å.

To compare this model to the STM data, a simulated STM image of the same section of the 3/2 approximant model is shown in Fig. 7.4(b) [108]. It is simulated under constant current conditions, to match the STM data. The 'top' tiles are the centre of the 'white flower' motifs, The central Mn atom at the surface images brightly, although there is some variation in brightness

due to variation in magnetic state [108]. Some of the 'bottom' pentagons contain 'dark stars', though not all. Many include extra atoms above the central hollow, so a 'dark star' is not visible. These are from the first shell in the Mackay cluster, surrounding the central Mn atom (see Section 2.1, Fig. 2.1).

A small patch of our STM data which closely matches this chosen section, is presented in Fig. 7.4(c). It shows a 40 Å × 35 Å region of a clean surface STM image, with the same Penrose P1 tiling superimposed. Although there is some variation in detail, there is still a close correlation between many of the features in the real and simulated STM data. The Mn atoms at the centre of 'top' pentagons are seen as bright spots. 'Dark stars', with varying clarity, are always contained within 'bottom' pentagons.

Using this approach, the nucleation site can be identified. An STM image from a low Bi coverage is used, where both the deposited Bi and the underlying substrate is resolved. The same Penrose P1 tiling is then constructed over the image, using the resolved surface features to position the known 'top' and 'bottom' tiles, and the tile matching rules to continue the tiling in between. The results of this exercise are shown in Fig. 7.5. The locations identified as 'dark stars' are highlighted with a star motif and become 'bottom' tiles. These are easily positioned as they are clearly visible in the STM data. When the tiling is completed over a large area, all of the bright pentagonal Bi clusters are then found in 'top' tiles. Many are full pentagons, shown by the 5 dark spots drawn on to identify each atom. Some clusters are only partially grown, but the atom locations are in the same position within each tile. These partial clusters are the initial stages of pentagonal cluster formation. Additional Bi atoms would be able to fill in the absent positions, leading to the formation of complete pentagonal clusters with the same orientation. Only a few adatoms are found on other tiles. The minimal amount suggests that these are not preferred locations.

The relative frequencies of the pentagon, rhombus, star and boat tiles in the infinite Penrose P1 tiling are shown in Eq. 7.1 [110].

$$1 : \frac{1}{\tau^4} : \frac{2\tau - 1}{5\tau^5} : \frac{1}{\tau^5} \tag{7.1}$$

This corresponds to percentage occurrences of 72.4:14.6:4.0:9.0 respectively. In the tiling patch in Fig. 7.5, the corresponding percentage occurrences are 72.6:14.5:0.9:12.0. The close match in these relative frequencies indicates that this tiling patch is large enough to be representative of the surface structure. The number density of 'top' pentagons in an infinite Penrose tiling is ~36% [110]. This provides a enough nucleation sites to produce a quasiperiodic framework of pentagonal Bi clusters, leading to a quasiperiodic

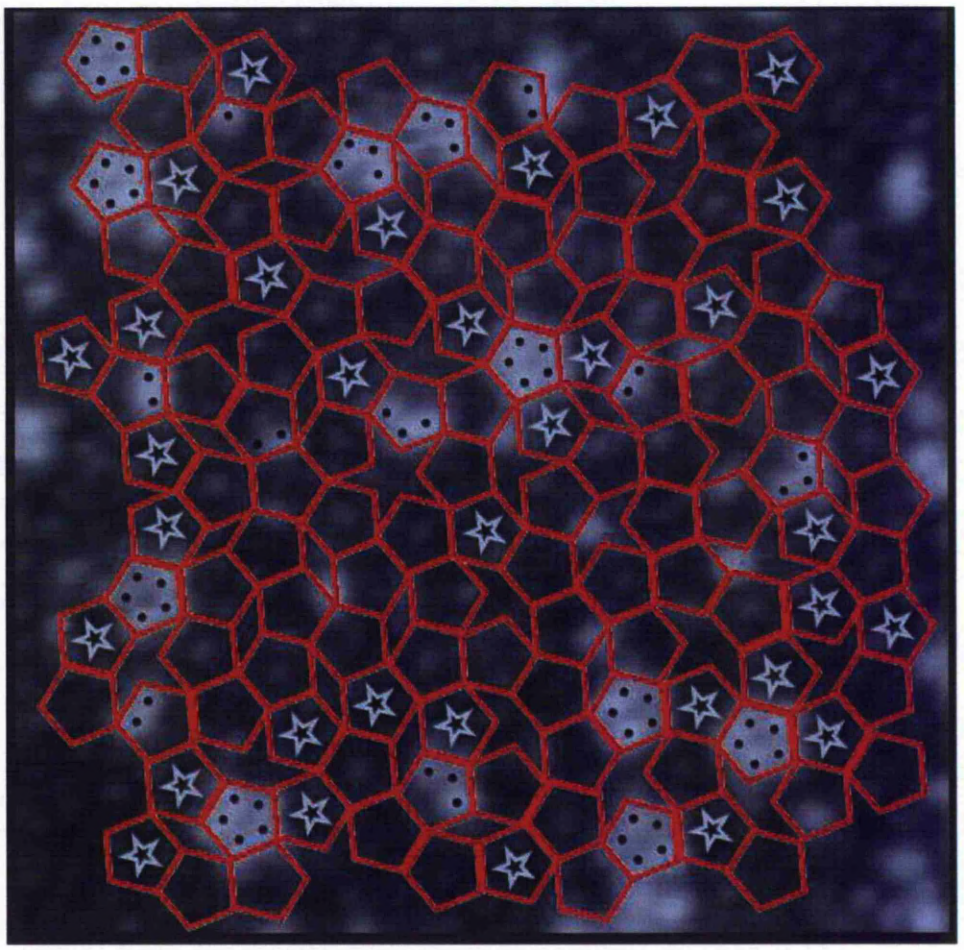

Figure 7.5: STM data showing 0.13 ML of Bi on i-Al-Pd-Mn. By achieving good resolution of both the Bi adatoms and the underlying surface, a Penrose P1 tiling can be superimposed. The same size is used, with edge length 7.8 Å. The tiling is positioned using the 'dark stars' to locate 'bottom' pentagons, indicated by a star motif. Bi clusters are found to nucleate only in the 'top' pentagonal tiles. Many are complete pentagonal clusters, but some are incomplete, indicated by the number of spots.

monolayer.

As the 'top' tiles have been identified as the nucleation site of the Bi pentagonal clusters, this can be applied back to the model used in Fig. 7.4 (a). The exact position of the Bi atoms is shown in Fig. 7.6. They nucleate

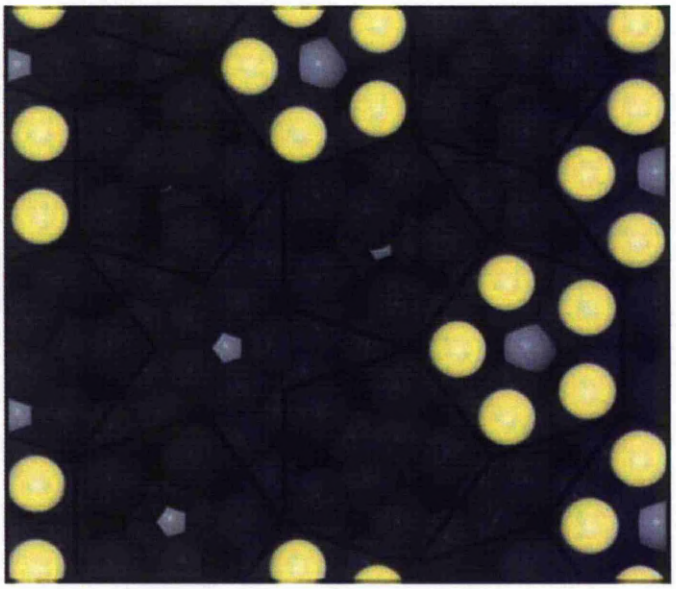

Figure 7.6: Surface model used in Fig. 7.4 (*a*) with the Bi pentagonal cluster nucleation sites superimposed. Bi atoms are shown in yellow, Al atoms dark grey, Pd atoms black, and Mn atoms light grey.

in the 3-fold hollows in between 3 Al atoms, or between 2 Al and 1 Pd atoms. This can be described as a quasi-three-fold adsorption site. Due to the random nature of an approximant structure the exact number of Pd atoms involved varies between tiles. The 5 Bi atoms making up the pentagonal cluster centre around the Mn atom in the surface plane, they sit above this central atom becoming part of the next shell of the Mackay cluster. They sit 1.2 ± 0.2 Å above the surface plane, as measured from the line profile analysis. This means that the distance between each Bi atom and the central Mn atom is $\sim$ 3.9 Å. The Mn atom obviously plays a role in the preference of this nucleation site, but this relatively large distance suggests that the influence of the Mn atom on the Bi atoms is felt indirectly through a substrate-mediated interaction. The Bi-Bi distance within each pentagon is 4.9 ± 0.1 Å. This is a factor τ^{-1} smaller than the edge-length of the tiling which is 7.76 Å.

7.5 Discussion

The nucleation site that has been identified from the STM data does not agree that with predicted by DFT calculations, discussed in Section 7.1.

Most surprisingly we did not find any Bi at low coverage in the location predicted to have the highest adsorption probability, above the 'dark stars' (-4.9eV). Indeed, none of the locations predicted were nucleation sites. The first reason for this discrepancy is that the DFT calculations only involve single Bi atoms sitting at locations. This neglects the additional stabilizing effect from the interatomic interactions between the Bi atoms within the pentagonal cluster. Secondly, the DFT calculations were performed at 0°K, whereas our experiment was at room temperature. Therefore the static atoms were not allowed enough energy to reorganise themselves, neglecting any possible reconstruction effects. A third reason could also be that the calculations were only performed on a small section of a 2/1 approximant. It may be that using a larger slab of a closer approximant, 3/2 or 5/3, would give a better prediction, though the large number of atoms would make the calculation time prohibitive.

The formation of pentagons rather than single atoms, and the high frequency of nucleation sites allows a quasiperiodic framework to grow. Based on the number of 'top' tiles, 36% of the surface can be covered in Bi pentagonal clusters with the same orientation. The low number of alternative nucleation sites observed in the STM data suggest that this happens close to 0.36 ML. Once this quasiperiodic framework of pentagonal Bi clusters is completed, additional Bi adatoms complete the monolayer by filling the gaps in between pentagons, at less energetically favourable sites, but the growing film keeps their symmetry. This leads to a quasiperiodic single monolayer, with predominantly 5-fold symmetry, in agreement with the LEED and HAS observations of Franke et al. for the full monolayer coverage [100]. Again, this is in disagreement with the DFT predictions for pseudodecagonal symmetry [103, 104].

The stability of the Bi pentagons is a crucial factor in the formation of this quasiperiodic monolayer. Studies involving Al deposited on Al-Cu-Fe [111], and C_{60} on Al-Pd-Mn [112], have found that single atoms/molecules nucleate at the 'dark star' positions. As predicted the number density of sites is too low to form a quasiperiodic framework. Si on Al-Pd-Mn is found to nucleate on 'top' tiles [101], but only single atoms rather than pentagons nucleate. Again, the number of sites is insufficient to induce the formation of a quasiperiodic monolayer.

7.6 Conclusion

The formation of a Bi monolayer deposited on the five-fold surface of *i*-$Al_{70}Pd_{21}Mn_9$, has been studied by STM (and since published [113]). Using

the model of an approximant structure to analyse the real STM data from the icosahedral quasicrystalline surface has proved a successful method. The finite unit cell size of approximants allows predictive structural calculations to be made, which would not be possible for infinite quasicrystalline structures. However their surfaces are sufficiently similar to have the same surface structures and properties. The identical surface motifs are particularly helpful as they are easily identified in STM images. A deeper understanding of the structure is gained by understanding the model, which can then be applied to understanding the structure of the quasicrystal in the surface region. In this way the Bi nucleation site has been identified.

Upon deposition of low sub-monolayer coverage, the epitaxial growth of 5 atom pentagonal clusters of Bi atoms with edge length 4.9 $\pm$ 0.3 Å is observed. The pentagons are self-assembled nanostructures. They have a common orientation leading to a film with five-fold symmetry. By inspection of images where both the underlying surface and the Bi atoms are resolved, the pentagonal clusters are found to nucleate on pseudo-Mackay clusters truncated such that a Mn atom lies centrally in the surface plane, identified as 'top' tiles. This position is the centre of the 'white flower' motif. The initial nucleation site is different to that proposed on the basis of recent density functional theory calculations [104]. The Bi film grows in the pure nucleation regime until the saturation island density is reached at $\sim$ 0.36ML. The density of these sites is sufficient to form a quasiperiodic framework. The remaining gaps in the over-layer are filled with individual Bi atoms, at less energetically favourable sites. The islands (pentagons) begin to coalesce and the film growth enters a pure growth regime, leading to the completion of a predominantly 5-fold quasiperiodic monolayer. The complete Bi monolayer cannot be resolved by STM.

Chapter 8

The structure and composition of Fe thin films deposited on the surface of 5-fold i-$Al_{70}Pd_{21}Mn_9$ studied by Medium Energy Ion Scattering

8.1 Introduction

The growth of thin films on quasicrystalline substrates is an area of considerable interest to researchers in this field. One example is the deposition of Fe onto i-$Al_{70}Pd_{21}Mn_9$. Previous studies show contradictory results. Weisskopf et al. used a combination of Auger electron spectroscopy (AES), low energy electron diffraction (LEED) and secondary-electron imaging (SEI) indicates that Fe-Al alloy formation occurs at the surface due to inter-diffusion. In addition, magneto-optical Kerr effect (MOKE) measurements show magnetic ordering in the grown film [2]. However, a more recent study by Wearing et al. using LEED, AES and scanning tunnelling microscopy (STM) indicated layer-by-layer growth of Fe and ruled out alloy formation [1]. Both studies indicate that a bcc-like structure occurs in the film. The aim of this study is to determine whether intermixing is taking place. Medium energy ion scattering (MEIS) is an ideal technique for further investigation of this system because of its unique ability to provide information simultaneously on the composition and structure as a function of depth.

8.2 Experimental methods

The sample was produced at Ames laboratory, using the Bridgman method [114], and was cut (spark-etched) perpendicular to a five-fold axis. It was then polished using 6, 1 and 0.25 μm diamond paste. Atomically flat surfaces with large flat terraces were obtained through cycles of 3 KeV Ar^+ sputtering (for 0.75 h) at room temperature followed by annealing for 4 h at a temperature of 905°K, for a total of 20 hours, at a base pressure of 1.5 x 10-10 mbar. The annealing temperature was monitored using an infrared pyrometer. Research grade high purity Fe (Goodfellow, Ermine Business Park Huntington, Cambridgeshire PE29 6WR, England) was sequentially deposited from a rod source using an Omicron EFM-3 electron beam evaporator with the sample at room temperature. Fe was deposited at a constant flux of 65nA, with typical settings: filament current = 2.15A, high voltage = 800V, and emission current = 10.7mA. Coverage was estimated from previous experiments, then calculated from the MEIS data.

The experiment was conducted at the MEIS facility at Daresbury Laboratory, which can accelerate helium or hydrogen ions from 50 KeV to 250 KeV. For this experiment a 100 KeV He^+ ion beam was used. The angle and energy of the scattered ions are determined using a toroidal electrostatic energy analyser with position-sensitive detector. The raw data is a 2D array of intensity as a function of energy and angle. The variation of backscattered ion intensity over the angular and energy range is shown by a false color map using the visible spectrum from violet to red to indicate increasing intensity.

The 2D data can be sectioned to produce a 1D angle spectrum (blocking pattern) or a 1D energy spectrum. The energy spectra are used to calculate compositional depth profiles. The 2D data can also be processed to 'gate' a range of energies that vary with angle, so that the signal from a specific element and/or layer can be isolated from other elements or layers. The blocking dips seen in these spectra can be attributed to known crystallographic orientations within the samples. The ratio of the intensity in blocking and non-blocking geometries (amplitude of the blocking dip) can be used as a relative measure of the degree of crystallinity in each layer [71].

The experimental station comprises four different chambers; for preparation, storage, analysis and fast entry, which are kept at ultra high vacuum. MEIS spectra were taken of the Al-Pd-Mn clean surface, after deposition of thin coverage of Fe, a thick coverage of Fe, and then after annealing the thick coverage to 300°C for 10 minutes. The 2D data was analysed using Midas. 1D energy spectra from these scans were then fitted using SIMNRA version 6.04, to enable compositional depth profiling. The thickness of these films was calculated, using the 1d energy spectra, to be 2.1ML (thin) and 10.3ML

(thick). 1ML is one monolayer of atoms. The Fe spectra was extracted from the data using a custom fitting routine (SuperMega Curve fit and Igor Pro), and the blocking dips from these spectra were then compared to a simulation from the expected structure, made using the Vegas code (Xvegas v132) [115].

8.3 Results and Analysis

The MEIS data, collected across all energies and scattering angles within the range, is presented as an intensity map. This 2D data is shown in Fig. 8.1. The diagonal bands change significantly as the film grows, and subtle changes are seen after annealling this film. To interpret these changes, 1D slices are taken from the 2D data.

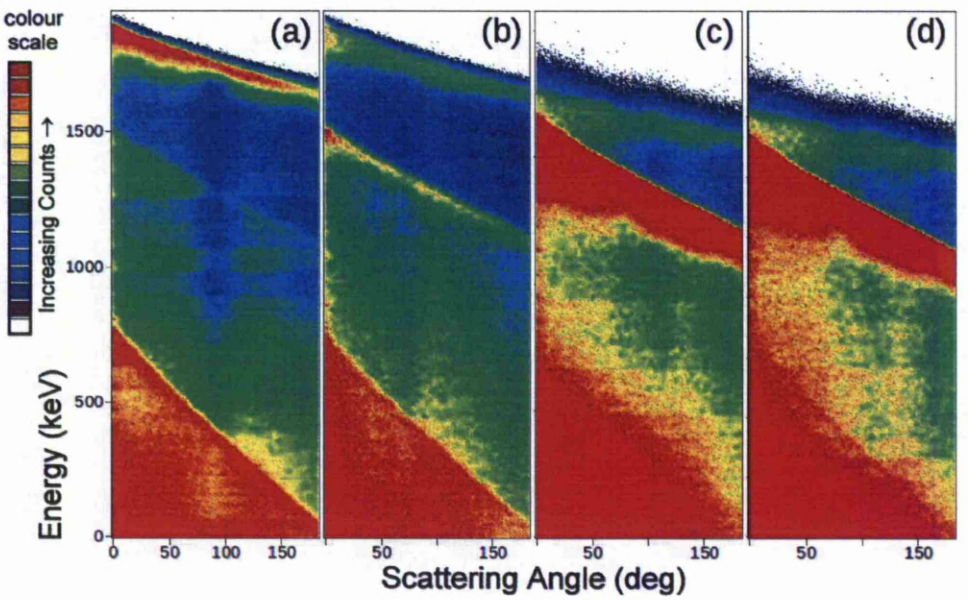

Figure 8.1: 2D MEIS data showing the growth of Fe on i-Al-Pd-Mn: (a) Clean surface i-Al-Pd-Mn; (b) 2ML thin film; (c); 10ML thick Film; (d); After annealing the 10ML film to 300°C for 10 minutes.

8.3.1 Energy Data

1D energy spectra, shown in Fig. 8.2 and Fig. 8.3, have been extracted from the 2D spectra, Fig.8.1. Table 8.1 shows the layer composition and thickness used to fit the 1D spectra in the model of the target sample, using the fitting

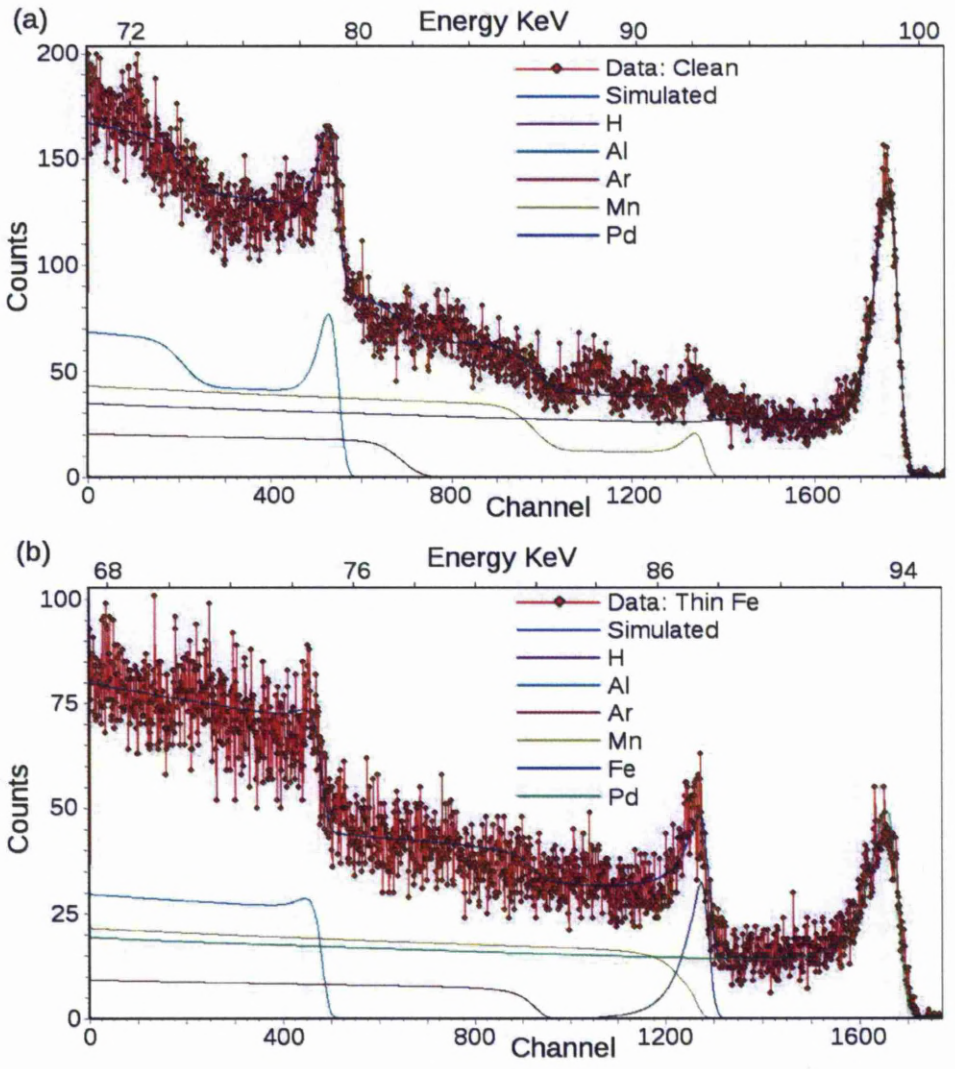

Figure 8.2: 1D Energy spectra extracted from the MEIS data, fitted using SIMNRA, showing the growth of Fe on i-Al-Pd-Mn: (a) Clean surface i-Al-Pd-Mn; (b) 2ML thin film.

software SIMNRA. The fit of the 5-fold i-Al-Pd-Mn clean surface data, Fig. 8.2(a), is consistent with previous MEIS results [116]. The surface region is Al rich compared to the bulk quasicrystal. For low Fe coverage, Fig. 8.2(b), an Fe-Al alloy is formed, but there is still Pd signal at the surface. This

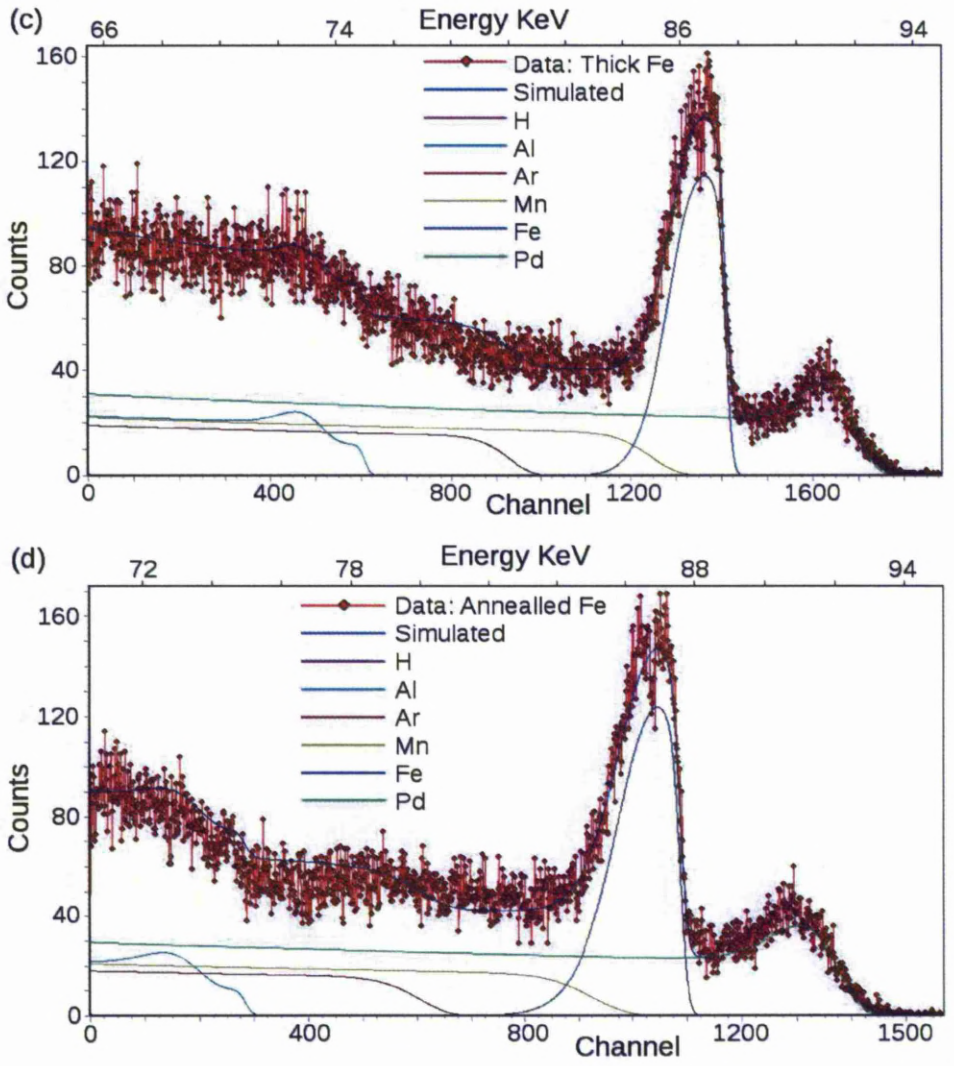

Figure 8.3: 1D Energy spectra extracted from the MEIS data, fitted using SIMNRA, showing the growth of Fe on *i*-Al-Pd-Mn: (*c*); 10ML thick Film; (*d*); After annealing the 10ML film to 300°C for 10 minutes.

shows that either the film is not continuous or that significant Pd has also diffused into the deposited layer. Since the data also indicates considerable roughening, an incomplete layer is a likely explanation. The SIMNRA analysis reveals a film thickness of 2.3 monolayers (MLE). For a thicker film, Fig.

8.3(c), the Pd signal is shifted down in energy consistent with a continuous film above it, although there is still considerable roughness. The composition of this film indicates an $AlFe_3$ alloy; this composition is consistent with magnetic ordering. The SIMNRA analysis gives a film thickness of 10 MLE. The annealed thick Fe coverage is shown in Fig. 8.3(d). The underlying i-Al-Pd-Mn surface is unchanged between (c) and (d). However, the Al-Fe film does show a shift in Fe towards the surface. Whereas (c) suggests a continuous $AlFe_3$ alloy, the annealed film (d) has a ratio in the outer layers of $AlFe_4$, and the underlying layers of the film are closer to $AlFe_2$. Annealing removes the Pd component in the bottom layer of the film, suggesting either Pd has diffused out, or the rough interface region has been smoothed out. However, (b),(c) and (d) all still indicate that there is some Al throughout the film, inconsistent with the pure Fe outer layers suggested by Wearing et al. [1]. A visual representation of the layers used in the model is shown in Fig. 8.4. No layers of pure Fe were found on any of the films studied, as introducing them to the model always reduced the goodness of fit to the data.

Taking an average through the surface layers and not including the Fe film layers, the Pd component in the quasicrystal surface region is 3.9%, 4.4%, then 8.3%, going from clean quasicrystal, to thin Fe coverage, then thick Fe. Similarly, the Mn increases from 12.6%, to 15.1%, then 18.4%. This shows that as Al diffuses into the film, it leaves Pd and Mn rich regions below the surface.

8.3.2 Angle Data

Angular data from the thin (2ML) film (Fig. 8.5) has no blocking dips, indicating that there is no long range order. Structural analysis of the MEIS angular data from the thick film indicates a 5-fold domain structure consistent with previous work. LEED results by both Wearing et al. [1] and Weisskopf et al. [2] show the initial loss of order upon deposition, followed by the appearance of a LEED pattern characteristic of 5 domains of (110) bcc Fe rotated 72° apart. STM data also revealed islands with a (110) bcc structure [1], rotated by 72° from each other, suggesting a strong influence of the 5-fold substrate in their alignment.

Fig. 8.6 shows a 1D slice of data from the thick (10ML) Fe film, specific to the Fe surface region. This is compared to a Vegas simulation of the film structure, using a model with five domains in equal amounts and 72° apart, of bcc-like structure at the interface, which is oriented with (110) type planes parallel to the five-fold quasicrystal surface. The structure is compressed vertically by 5.5%, from the typical lattice parameter of 2.97 Å. Although the amplitude of the blocking dips are not exactly the same, the position of

Table 8.1: Atomic Composition of layers, calculated using SIMNRA.

Layer	Al %	Pd %	Mn %	Fe %	Thickness 10^{15} atoms/cm^2	Thickness Å
(*a*) Clean Surface *i*-Al-Pd-Mn						
1	77.9	15.9	6.1	0	5.5	6.4
2	86.2	5.9	7.9	0	186	215
3	83.1	3.4	13.5	0	1000	1160
(*b*) Thin Fe Coating (2ML)						
1	34.9	15.2	0	49.8	3.7	4.3
2	81.0	11.1	7.9	0	5.3	6.1
3	80.5	4.3	15.2	0	1000	1160
(*c*) Thick Fe coating (10ML)						
1	25.7	0	0	74.3	15.8	18.4
2	25.2	2.8	0	72.0	2.3	2.6
3	78.2	16.2	5.6	0	6.7	7.8
4	73.2	8.3	18.5	0	1000	1160
(*d*) Annealed Thick Fe coating (10ML)						
1	21.6	0	0	78.4	14.8	17.2
2	34.4	0	0	65.6	3.2	3.7
3	78.0	16.1	5.9	0	7.6	8.8
4	73.2	8.3	18.5	0	1000	1160
Bulk	70	21	9	0		

the dips are similar. This indicates that although the film structure is similar to the ideal case, the real film is more disordered.

Fig. 8.7 shows a 1D slice of data from the thick (10ML) Fe film, specific to the Fe sub-surface region. This is compared to a Vegas simulation using a model with five domains in equal amounts and 72° apart, of bcc-like structure at the interface, which is oriented with (110) type planes parallel to the five-fold quasicrystal surface. However, the lattice parameter has been expanded by 2% to 3.03 Å, and the structure is much less ordered (40% disorder).

8.4 Discussion

The main objective of this MEIS study was to clarify the question of intermixing when iron is deposited on Al-Pd-Mn. This data shows that there is intermixing at both low and high coverage, agreeing with the work by Weis-

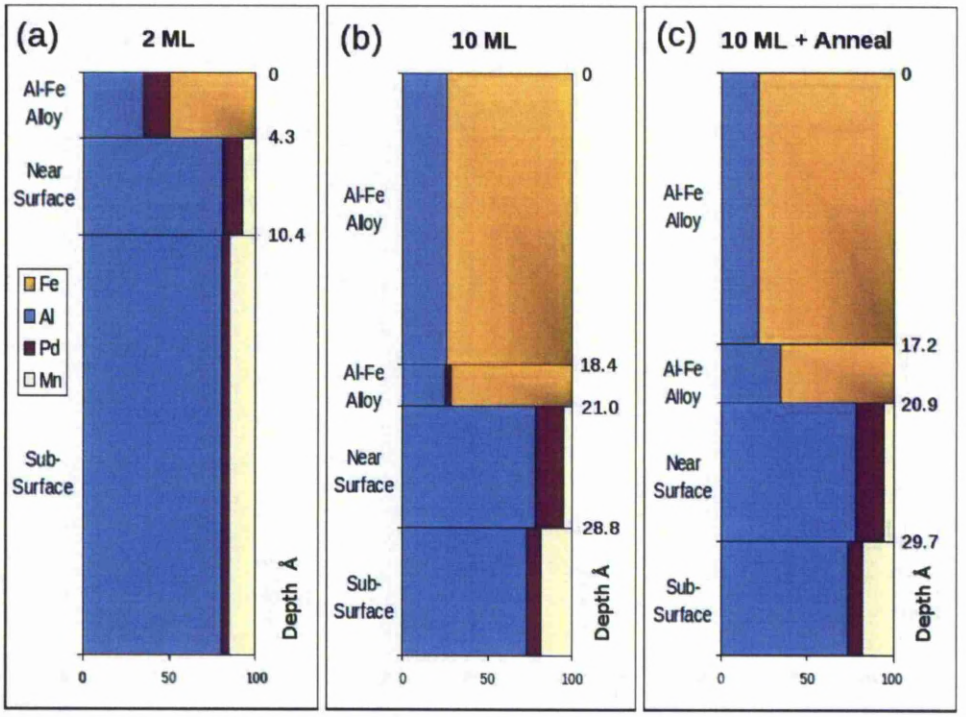

Figure 8.4: Visual representation of layer composition, from data in Table 8.1: (*a*) 2ML Fe thin film deposited on *i*-Al-Pd-Mn; (*b*) 10ML thick Film; (*c*) After annealing the 10ML film to 300°C for 10 minutes.

skopf et al. [2], despite the fact that the preparation conditions were chosen to match those of Wearing et al. [1]. This would have been an interesting result, as intermixing usually occurs in similar systems, such as Fe deposited onto Al (1 1 1) [117]. Wearing et al. suggested two possible reasons why their results may be different. Weisskopf et al. had an anneal temp of 700-800°K, and deposited Fe with the sample at 340°K. Wearing et al. annealed at 905°K, in order to create an atomically flat surface, and deposited at room temperature, decreasing the chance of inter-diffusion. Hence we used an anneal temperature of 905°K, and the Fe was deposited when the sample was at room temperature, but did not observe the same lack of intermixing.

The intermixing of Al and Fe in the surface layers seem to be continuous and fairly uniform throughout the thick surface alloy. The results from the SIMNRA fitting exercise on the data from the thick Fe coverage, show that the bottom layer of the Al-Fe alloy (Table 8.1, Fig. 8.4(*b*)) has roughly the same composition as the top layer. Introducing a pure Fe layer to the

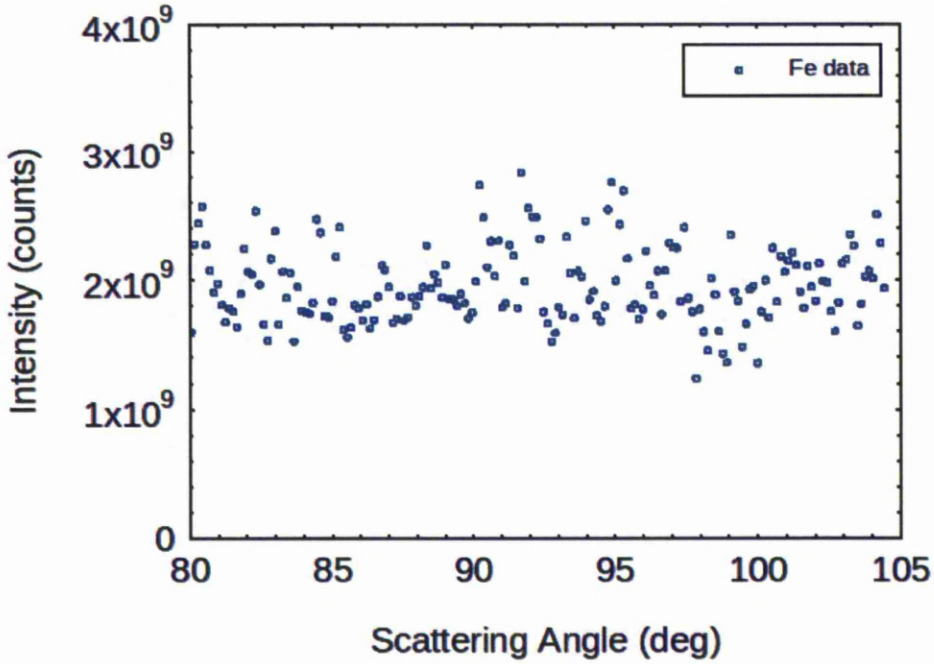

Figure 8.5: The angular data from the 2 MLE thin film indicates the film has no long range order.

model, even on top of this Al-Fe layer, resulted in a poor fit to the data, suggesting that pure Fe layers are not growing upon deposition, even up to 10 monolayers film thickness. The composition of this film indicates an $AlFe_3$ alloy, which is consistent with magnetic ordering [2]. Annealing this film (Table 8.1, Fig. 8.4(c)) induces diffusion of Fe towards the surface, and Al down into the film. Producing outer layers of $AlFe_4$, and the underlying layers of the film are more like $AlFe_2$

The composition results for the thin Fe coverage (Table 8.1, Fig. 8.4(a)) are not as clear. The layer used to represent the surface alloy has a strong Al and Pd component within the Fe film, giving a composition of $Al_{35}Fe_{50}Pd_{15}$. The Pd signal could be due to Pd diffusing into the film, but the high roughness of the underlying interface between the quasicrystal and the film allows another possibility. The way this roughness is simulated in the SIMNRA software does not account for completely separated islands within a layer. Rather than a Al-Pd-Fe alloy, this could be separated Al-Fe islands, with parts of the i-Al-Pd-Mn surface still exposed. This detailed model is beyond the capability of the fitting software, even with high roughness parameters,

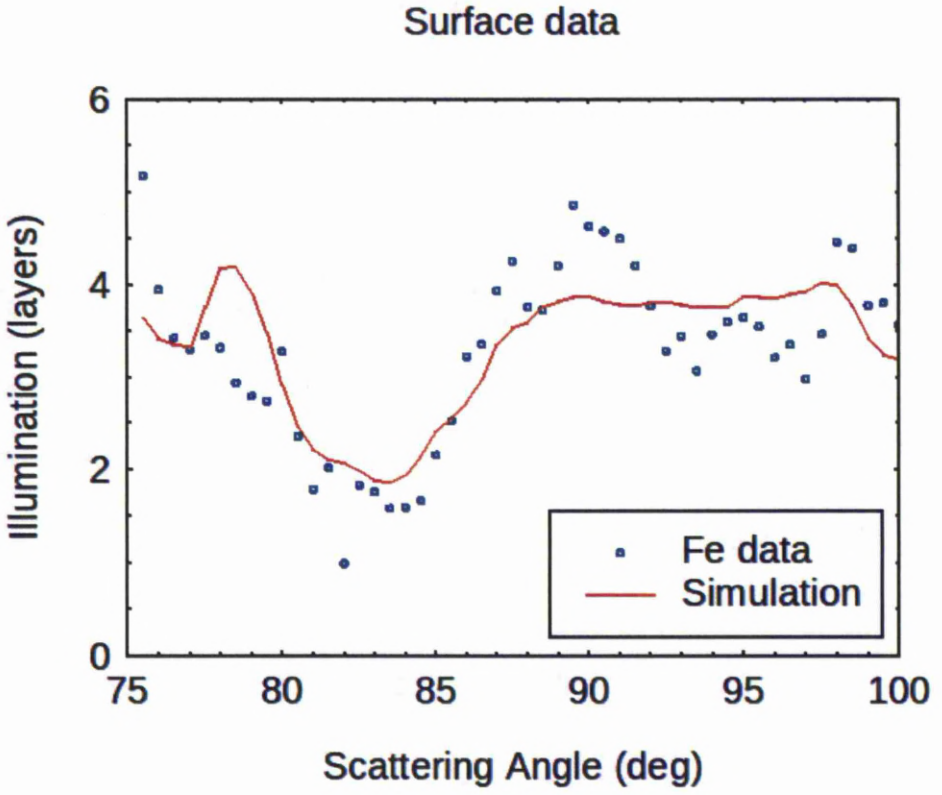

Figure 8.6: The Fe blocking pattern from the 10 MLE surface region (dotted line) is compared to a Vegas simulation (solid line) of 5 bcc-like domains rotated 72° from each other, with the (110) planes parallel to the surface, compressed vertically by 5.5%.

so the software simplifies this as one layer, by introducing a Pd signal into the layer. There would also be a Mn component in this layer, but this could not be seen in the data. The Mn peak is hard to distinguish from the Fe peak (Fig. 8.3(c)), as they both overlap, and the Mn peak is not very prominent. Also, Mn is only a minor component of the quasicrystal, just 6% near the surface, so the weak signal from the surface Mn is overshadowed by the strong signal from the high concentration of Fe in the surface layers. Therefore the Fe peak could also include indistinguishable counts from the Mn component.

While scattered Al-Fe islands seem likely, there is a problem with this explanation. The amount of Pd in the thin film is 15.2%. In the clean surface it is 15.9%, so it has only dropped by 4.4%. However, the proportion

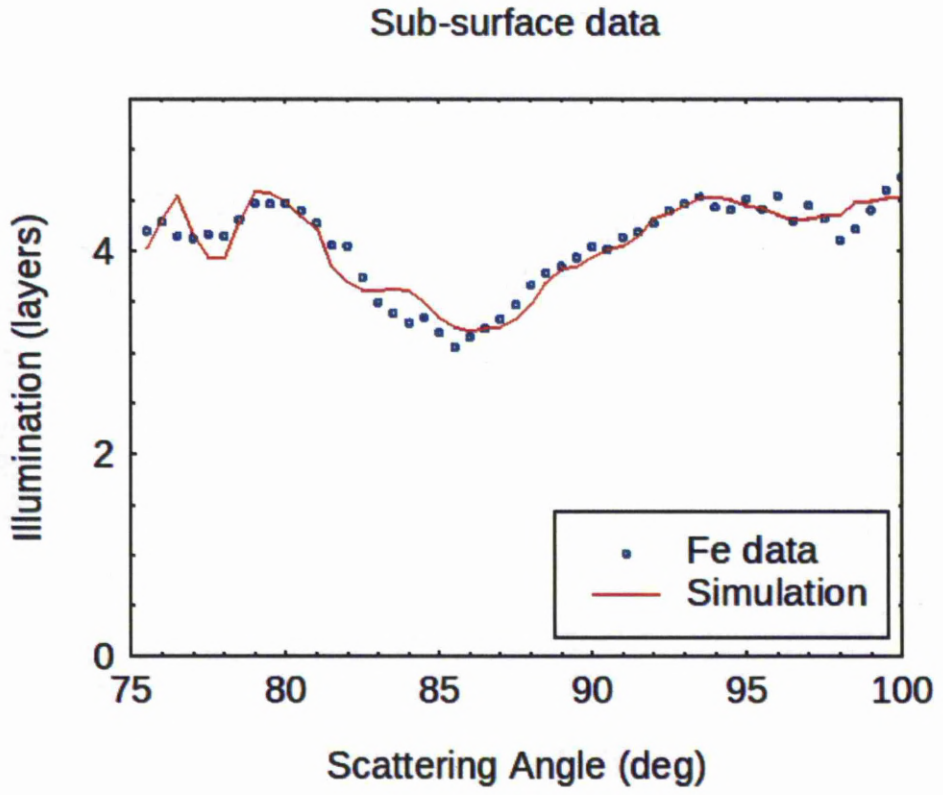

Figure 8.7: The Fe blocking pattern from the 10 MLE sub-surface region (dotted line) is compared to a Vegas simulation (solid line) of 5 bcc-like domains rotated 72° from each other, with the (110) planes parallel to the surface, with the lattice expanded by 2%.

of Al has dropped by over 50%. If all the Al signal was from underlying exposed Al-Pd-Mn, then we should also see a 50% drop in the amount of Pd. If some of the Al signal was from Al-Fe islands, then the Pd signal should drop even further, as much as four times smaller if it was all $AlFe_3$.

An alternative explanation which fits in with the percentage of atoms seen in the data, is that upon deposition, the Fe atoms do indeed intermix with the substrate quasicrystal. The composition observed suggests a direct substitution of Al with Fe atoms, as the total percentage of Al+Mn on the clean surface (84%) is very close to the percentage of Al+Fe+Mn (84.7%) in this thin film . As this composition is so similar, the Al-Fe-Pd-Mn film could have quasicrystal approximant structural components. However, the LEED

evidence does not support any long range order. This surface alloy would be $Al_{35}Fe_{44}Mn_6Pd_{15}$, if it is a uniform alloy, and it is assumed that some of the Fe signal is actually Mn, and that the ratio of Mn to Pd is the same as in the clean surface.

Hence the thin film, which has a disordered LEED pattern, could indeed be an Al-Mn-Pd-Fe alloy, with a composition approximating the Al-Pd-Mn quasicrystal. LEED results by both Wearing et al. [1] and Weisskopf et al. [2] show the initial loss of order upon deposition, followed by the appearance of a LEED pattern above 3ML, characteristic of 5 domains of (1 1 0) bcc Fe rotated 72° apart. They deduce the formation of multilayer islands from this. This is further confirmed by the Vegas comparison (Fig. 8.6, and Fig. 8.7). The simulation used to get a similar blocking pattern to the data uses 5 domains of (1 1 0) bcc Fe rotated 72° apart. This shows that the Al-Fe alloy is influenced by the 5-fold symmetry of the underlying substrate. This suggests that the alloy in the first layers isn't completely disordered, and may have some of the quasiperiodic symmetry from the bulk. The disorder seen in the LEED pattern may be due to increased roughness, suggesting the Al-Mn-Pd-Fe growth is not a smooth layer by layer process. This disorder may be further increased by many nucleations of small Al-Fe bcc islands mixed in with an Al-Mn-Pd-Fe alloy, which is probably retaining some 5 fold symmetry in local clusters. This type of pseudomorphic growth has been observed on similar systems. Co adsorbed on the ten-fold surface of *d*-Al-Ni-Co and the five-fold surface of *i*-Al-Pd-Mn, forms rows which are quasiperiodically ordered, but within the rows crystalline Co is observed [118]. Cu adsorption on *i*-Al-Pd-Mn exhibits similar pseudomorphic growth [119–121].

The data also shows that Fe deposition leads to an increase in Pd and Mn in the subsurface layers (table 8.1), as Al diffuses into the film. This can be seen in even the deepest layers. For the thick film, the underlying layers had doubled in Pd content; the Mn concentration had also increased by 50%. This reopens the case for Al-Fe island formation upon a partially exposed Al-Pd-Mn surface, for the thin Fe coverage. The increase in Pd concentration at the quasicrystal surface could be the reason why the Pd signal in the surface film is so high. If the Pd concentration doubles in the surface layer of the quasicrystal, then the proportions of atoms is consistent with Fe covering half the surface, and half the underlying surface exposed. There may also be some selective nucleation of non-Pd sites, leaving more Pd exposed.

8.5 Conclusion

The film structure for the thin Fe case could be one of several possibilities: separated Al-Fe islands upon exposed Pd rich quasicrystal, an $Al_{35}Fe_{50}Pd_{15}$ alloy with no Mn, or an $Al_{35}Fe_{44}Mn_6Pd_{15}$ alloy (with an estimated quantity of Mn). We cannot distinguish between these possibilities from the available data. The real surface is likely to be a complicated mix of many different structures, but the angle data indicates no long range order. Whilst this is inconclusive, it does rule out the possibility of the initial layer by layer growth of pure Fe; so this result is in disagreement with Wearing et al. [1]. However, this is in agreement with Weisskopf et al. [2], who find that, for low coverages, Fe diffuses into the bulk and destroys the quasicrystalline atomic order in the surface layers. While all studies agree on the thick film structure of 5 (110) bcc domains rotated by 72°, we find that the composition of $AlFe_3$ matches the findings of Weisskopf et al. Even in the thick film, we could not find any layers of pure Fe, as suggested by Wearing et al. Structural analysis of the angle data for the thick film indicates it is compressed vertically by 5.5% in the surface region, and expanded by 2% in the much less ordered sub-surface region.

Chapter 9

Summary and future directions

STM and LEED studies of Al_4(Cr,Fe) have shown that the clean surface structure of an approximant is very close to a bulk structure termination, as is the case for icosahedral quasicrystals. The surface is highly ordered, and the cluster based structure is revealed as rings of atoms on the STM data. X-ray diffraction data has proved a useful tool to help understand the surface STM data. By comparison of adjacent terraces, the inversion symmetry expected from the x-ray diffraction data, has been demonstrated. New preparation cycles have also been identified, reducing the preparation time by using sputter cycles with diminishing lengths.

STM and XPS has been used to study the oxidation of this approximant. The STM data indicates that the initial oxidation is highly ordered, forming rows of Al_2O_3. Oxygen preferentially adsorbs onto the surface of terraces, and step edges remain intact. The XPS data has shown that only Al is oxidized, while Cr and Fe remain unchanged.

Quantitative analysis of XPS data has shown the Strohmeier method to be a fast and accurate way of determining Al_2O_3 film thickness. Investigating the oxidation of the (0 1 0), (1 0 0) and (0 0 1) surfaces of the Al_4(Cr, Fe) quasicrystal approximant using this method has shown shown that the surfaces oxidise at the same rates, despite being very different structurally.

The formation of a Bi monolayer deposited on the five-fold surface of *i*-$Al_{70}Pd_{21}Mn_9$, has been studied by STM. Using the model of an approximant structure to analyse the real STM data from the icosahedral quasicrystalline surface has proved a successful method. The finite unit cell size of approximants allows predictive structural calculations to be made, which would not be possible for infinite quasicrystalline structures. However their surfaces are sufficiently similar to have the same surface structures and properties. The identical surface motifs are particularly helpful as they are easily identified in STM images. Atomic resolution has been achieved simultaneously on both

the partial Bi monolayer and the underlying quasicrystal surface. A deeper understanding of the structure is gained by understanding the model, which can then be applied to understanding the structure of the quasicrystal in the surface region. In this way the Bi nucleation site has been identified. The epitaxial growth of pentagonal clusters leeds to the formation of a quasiperiodic framework, and ultimately a quasiperiodic single element monolayer. The initial nucleation site is different to that proposed on the basis of recent density functional theory calculations. DFT calculations of the Al_4(Cr, Fe) (1 0 0) surface are underway. After the success of using DFT calculations to help interpret the Bi/Al-Pd-Mn system, this will enhance the understanding of the Al-Cr-Fe system.

MEIS data has provided detailed information on the composition and structure of Fe films grown on the quasicrystalline surface of *i*-Al-Pd-Mn. The data has revealed that initially a disordered film is formed on the surface, composed of Al, Fe, Pd, and possibly Mn. The angle data in this region indicates no long range order. As more Fe is deposited, an $AlFe_3$ film grows above this. The composition, measured up to the 10 ML thickness, is the same throughout this layer, and matches the findings of Weisskopf et al. [2]. The angle date from the region indicates a structure of 5 (110) bcc domains rotated by 72°, compressed vertically by 5.5% in the surface region, and expanded by 2% in the much less ordered sub-surface region. The MEIS data rules out the possibility of the initial layer by layer growth of pure Fe; so this result is in disagreement with Wearing et al. [1].

Chapter 10

List of Publications

10.1 Papers

"Nucleation and growth of a quasicrystalline monolayer: Bi adsorption on the ve-fold surface of *i*-Al-Pd-Mn."
J.A. Smerdon, J.K. Parle, L.H. Wearing, T.A. Lograsso, A.R. Ross, R. McGrath.
Phys. Rev. B, 78, 075407, **2008**

"Formation of a quasicrystalline Pb monolayer on the 10-fold surface of the decagonal AlNiCo quasicrystal."
J.A. Smerdon, L. Leung, J.K. Parle, C.J. Jenks, R. McGrath, V. Fourne, J. Ledieu.
Surface Science, 602 2496-2501 **2008**

"Surface study of the (1 0 0) and (0 1 0) faces of the quasicrystal approximant Al_4(cr,fe)."
J. A. Smerdon, J. T. Parle, R. McGrath, B. Bauer, and P. Gille.
Z. Kristallogr., 224, 1315, **2009**

"C_{60} adsorption on an aperiodically modulated Cu surface"
J.A. Smerdon, J.K. Parle, L.H. Wearing, L. Leung, T.A. Lograsso, A.R. Ross, R. McGrath.
J. Phys.: Conf. Ser. 226 012006 **2010**

"Ordering of adsorbed species on quasicrystal surfaces."
J. A. Smerdon; L. H. Wearing; J. K. Parle; L. Leung; H. R. Sharma; J. Ledieu; R. Mcgrath
Philosophical Magazine, 88:13, 2073 2082 **2008**

10.2 Presentations

"STM and XPS investigation of the Oxidation of the (1 0 0) surface of Al_4(Cr,Fe) quasicrystal approximant",
Complex Metallic Alloys Network of Excellence, VIL-D topical meeting, Berlin **2009**

10.3 Posters

"Surface Study of Al_4(Cr,Fe) Quasicrystal Approximant",
International Quasicrystal Conference (ICQ10) **2008**

"Epitaxial growth of a quasicrystalline bismouth monolayer on i-$Al_{70}Pd_{21}Mn_9$"
Interdisciplinary Surface Science Conference (ISSC17) **2009**
Aperiodic '09, Liverpool **2009**

"MEIS investigation of Fe thin film grown on i-$Al_{70}Pd_{21}Mn_9$"
Aperiodic '09, Liverpool **2009**

Bibliography

[1] L. H. Wearing, J. A. Smerdon, L. Leung, T. A. Lograsso, A. R. Ross, and R. McGrath. Iron deposition on the five-fold surface of the icosahedral al-pd-mn quasicrystal. *Surf. Sci.*, 601:3450–3455, 2007.

[2] R. Luscher Y. Weisskopf and M. Erbudak. Structural modifications upon deposition of fe on the icosahedral quasicrystal al-pd-mn. *Surf. Sci.*, 578:35–42, 2005.

[3] D. Shechtman, I. Blech, D. Gratias, and J. W. Cahn. Metallic phase with long-range orientational order and no translational symmetry. *Phys. Rev. Lett.*, 53:1951, 1984.

[4] International union of crystallography, report to the executive committee for 1991. *Acta Cryst.*, A(48):922, 1992.

[5] F.C. Frank and J.S. Kasper. Complex alloy structures regarded as sphere packings. i. definitions and basic principles. *Acta. Cryst.*, 11:184, 1958.

[6] F.C. Frank and J.S. Kasper. Complex alloy structures regarded as sphere packings. ii. analysis and classification of representative structures. *Acta. Cryst.*, 12:483, 1959.

[7] G. Friedel. *Lecons de cristallographie.* Libraire Scientifique, Paris.

[8] D. Levine and P. J. Steinhardt. Quasicrystals: A new class of ordered structures. *Phys. Rev. Lett.*, 53:2477–2480, 1984.

[9] A.L. Mackay. Crystallography and the penrose pattern. *Physica A*, 114A:609–613, 1982.

[10] Z. Papadopolos, G. Kasner, R. D. Diehl, J. Ledieu, E. J. Cox, N. V. Richardson, Q. Chen, T. A. Lograsso, A. R. Ross, and R. McGrath. Bulk termination of the quasicrystalline five-fold surface of $al_{70}pd_{21}mn_9$. *Phys. Rev. B*, 66:184207, 2002.

[11] V. R. Dhanak H. R. Sharma K. Young T. A. Lograsso A. R. Ross R. McGrath J. A. Smerdon, N. Cross. Structure and reactivity of bi allotropes on the fivefold icosahedral alpdmn quasicrystal surface. *Journ. Phys. Cond. Matt.*, 22:345002, 2010.

[12] L. Danzer. Three-dimensional analogs of the planar penrose tilings and quasicrystals. *Discrete Math.*, 76:1–7, 1989.

[13] P. Sainfort and B. Dubost. The t2 compound: A stable quasicrystal in the system al-li-cu-(mg). *Journal Phys. France*, 47:321–330, 1986.

[14] A. P. Tsai. A stable quasicrystal in al-cu-fe system. *Jpn. J Appl. Phys.*, 26:L1505–7, 1987.

[15] A.P. Tsai, A. Inoue, Y. Yokoyama, and T. Masumoto. Stable icosahedral alpdmn and alpdre alloys. *Mater. Trans. JIM*, 31:98–103, 1990.

[16] J. Q. Guo. Stable icosahedral quasicrystals in the cdmgre (re = rare earth element) systems. *Jpn. J Appl. Phys.*, 39:L770, 2000.

[17] A.P. Tsai. Highly ordered structure of icosahedral quasicrystals in zn-mg-re systems. *Phil. Mag. Lett.*, 70:169–175, 1994.

[18] K. F. Kelton. Ti/zr-based quasicrystals-formation, structure and hydrogen storage properties,. *Mater. Research Society Samposium Proceedings (Edited by J.-M. Dubois, P. A. Thiel, A. P. Tsai, and KUrban)*, 553:471–481, 1999.

[19] D. Chen. New type of two-dimensional quasicrystal with twelvefold rotational symmetry. *Phys. Rev. Lett*, 60:1645, 1988.

[20] L. Bendersky. Quasicrystal with one-dimensional translational symmetry and a tenfold rotation axis. *Phys. Rev. Lett.*, 55(14):1461–1463, 1985.

[21] T. Ishimasa. New ordered state between crystalline and amorphous in nicr particles. *Phys. Rev. Lett.*, 55:511–513, 1985.

[22] J. Q. Guo, E. Abe, and A. P. Tsai. Stable icosahedral quasicrystals in binary cd-ca and cd-yb systems. *Physical Review B*, 62(22):14605–14608, 2000.

[23] V. Elser. Crystal and quasicrystal structures in al-mn-si alloys. *Phys. Rev. Lett.*, 55:2883, 1985.

[24] K. Hiraga. in quasicrystals. the state of the art. (edited by d. p. divincenzo and p. j. steinhardt). *World Scientific (Singapore, New Jersey, London, Hong Kong)*, pages 95–110, 1991.

[25] I. Kanazawa. Positron-annihilation study of icosahedral alpdmn alloys. *Phys. Rev. Lett.*, 79:2269, 1997.

[26] M. Quiquandon, Y. Calvayrac, A. Quivy, F. Faudot, and D. Gratias. Quasicrystals, preparation, properties and applications. *Mat. Res. Soc. Symp. Proc.*, 553:95, 1999.

[27] Z. Papadopolos, P. Kramer, G. Kasner, and D.E. Brgler. Quasicrystals. *Mat. Res. Soc. Symp. Proc.*, 553:231, 1999.

[28] C. Janot. Atomic clusters, local isomorphosm, and recurrently localized states in quasicrystals. *J. Phys.: Cond. Matter*, 9:1493–1508, 1997.

[29] V. Elser. Random tiling structure of icosahedral quasicrystals. *Phil. Mag. B*, 73:641, 1996.

[30] M. Boudard, M. de Boussieu, C. Janot, G. Heger, C. Beeli, H. U. Nissen, H. Vincent, R Ibberson, M. Audier, and J. M. Dubois. Bulk structure of alpdmn. *J. Phys.: Condensed Matter*, 4:10149, 1992.

[31] C. Janot. Quasicrystals as a hierarchy of clusters. *Phys. Rev. Lett.*, 72:1674, 1994.

[32] Ph. Ebert, M. Feuerbacher, N. Tamura, M. Wollgarten, and K. Urban. Evidence for a cluster-based structure of alpdmn single quasicrystals. *Phys. Rev. Lett.*, 77:3827–3830, 1996.

[33] H. M. Cataldo. Stability of a hard-sphere binary quasicrystal. *Philosophical Magazine B*, 79(10):1603–1613, 1999.

[34] N. Wang. Twodimensional quasicrystal with eightfold rotational symmetry. *Phys. Rev. Lett.*, 59:1010–1013, 1987.

[35] P. J. Steinhardt, H. C. Jeong, K. Saitoh, M. Tanaka, E. Abe, and A. P. Tsai. Experimental verification of the quasi-unit-cell model of quasicrystal structure. *Nature*, 396(6706):55–57, 1998.

[36] E. Abe, K. Saitoh, H. Takakura, A. P. Tsai, P. J. Steinhardt, and H. C. Jeong. Quasi-unit-cell model for an al-ni-co ideal quasicrystal based on clusters with broken tenfold symmetry. *Phys. Rev. Lett.*, 84:4609–4612, 2000.

[37] H.C. Jeong and P.J. Steinhardt. Constructing penrose-like tilings from a single prototile and the implications for quasicrystals. *Phys. Rev. B*, 55:3520, 1997.

[38] L. X. He. One-dimensional quasicrystal in rapidly solidified alloys. *Phys. Rev. Lett.*, 61:1116, 1988.

[39] K. Urban and M. Feuerbacher. Structurally complex alloy phases. *J. Non-Crystalline Solids*, 334-335:143–150, 2004.

[40] H. R. Sharma, M. Shimoda, and A. P. Tsai. Quasicrystal surfaces: structure and growth of atomic overlayers. *Adv. Phys.*, 56:403–464, 2007.

[41] A. Kallel. *Compt. Rend. Acad. Sci. Paris*, 268B:455, 1969.

[42] J.N. Pratt. The intermetallic compounds in the alloys of aluminium and silicon with chromium, manganese, iron, cobalt and nickel. *J. Inst. Metals*, 80:449, 1951.

[43] Martin Palm. The al-cr-fe system-phases and phase equilibria in the al-rich corner. *J. Alloys Compd.*, 252:192–200, 1997.

[44] A. Ziani. Transformation of the quasicrystalline phase al-cr-fe induced by rapid solidification. *J. Mater. Sci.*, 30, 1995.

[45] J. Ghanbaja V. Demange and J. M. Dubois. Electron microscopy study of approximant phases in the alcrfe system. *Phil. Mag.*, 86(3-5):469–474, 2006.

[46] D W Deng. Crystal structure of the orthorhombic al_4(cr,fe) approximant of the al-cr-fe decagonal quasicrystal. *JOURNAL OF PHYSICS CONDENSED MATTER*, 16:2283–2296, 2004.

[47] H X Sui. Structural model of the orthorhombic non-fibonacci approximant in the al12fe2cr alloy. *Acta Crystallographica B*, 53:587, 1997.

[48] H. X. Sui, X. Z. Liao, and K. H. Kuo. A non-fibonacci type of orthorhombic decagonal approximant. *Phil. Mag. Lett.*, 71:139–145, 1995.

[49] Z M Mo. Structure of (nu)-al80.61cr10.71fe8.68, a giant hexagonal approximant of a quasicrystal determined by a combination of electron microscopy and x-ray diffraction. *Acta Crystallographica B*, 56:392, 2000.

[50] G. Kreiner and H. Fraanzen. The crystal structure of λ-al_4mn. *J. Alloys Compd.*, 261:83, 1997.

[51] C. Dong. *Phil. Mag. A*, 73:1519, 1996.

[52] S. Ebalard. Approximants to the icosahedral and decagonal phases in the alcucr system. *J. Mater. Res.*, 6:1641, 1991.

[53] AJ Bradley and P Jones. An x-ray investigation of the copper-aluminium alloys. *J. Inst. Metals*, 51:131–162, 1933.

[54] J.K. Brandon. γ-brasses with i and p cells. *Acta Crystallographica*, B33:527–537, 1977.

[55] M.H. Booth. γ-brasses with f cells. *Acta Crystallographica B*, 33:30, 1977.

[56] M. Bostrom. *Solid State Chem.*, 153:398, 2000.

[57] W.B. Pearson J.K. Brandon and P.W. Riley. γ-brasses with r cells. *Acta Crystallographica*, B33:1088–1095, 1977.

[58] W. B. Pearson J.K. Brandon, P. C. Chieh and P. W. Riley. An error parameter analysis of tetrahedral configurations in γ-brass structures. *Acta Crystallographia*, A31:236–240, 1975.

[59] L. Arnberg. *Acta Crystallographia A*, 31:S98, 1975.

[60] V. Demange. About gamma-brass phases in the al-cr-fe system and their relationships to quasicrystals and approximants. *Phil. Mag.*, 85(12):1261–1272, 2005.

[61] V. Demange. New approximant phases in al-cr-fe. *Mat. Sci. Eng. A*, 79:294–296, 2000.

[62] A.R. Kortan, R.S. Becker, F.A. Thiel, and H.S. Chen. Real-space atomic structure of a two-dimensional decagonal quasicrystal. *Phys. Rev. Lett.*, 64:200, 1990.

[63] C. J. Jenks, J. W. Burnett, D. W. Delaney, T. A. Lograsso, and P. A. Thiel. Effect of sputtering gas on the surface composition of an al-pd-mn quasicrystal. *Appl. Surf. Sci.*, 157(1-2):23–28, 2000.

[64] M. Gierer, M. A. Van Hove, A. I. Goldman, Z. Shen, S. L. Chang, C. J. Jenks, C. M. Zhang, and P. A. Thiel. Structural analysis of the fivefold symmetric surface of the al70pd21mn9 quasicrystal by low energy electron diffraction. *Phys. Rev. Lett.*, 78(3):467–470, 1997.

[65] K. Pussi, D. E. Reid, N. Ferralis, R. McGrath, T. A. Lograsso, A. R. Ross, and R. D. Diehl. Low-energy electron diffraction (leed) study of an aperiodic thin film of cu on 5-fold *i*-al-pd-mn. *Phil. Mag.*, 88:2103–2110, 2008.

[66] N. Fairly. *CasaXPS© Version 2.3.14.* Casa Software Ltd, www.casaxps.com, 1999-2009.

[67] D.A. Shirley. High-resolution x-ray photoemission spectrum of the valence bands of gold. *Phys. Rev. B*, 5:12:4709–4714, 1972.

[68] M. Sunjic S. Doniac. Many-electron singularity in x-ray photoemission and x-ray line spectra from metals. *J. Phys. C*, 3(2):285, 1970.

[69] N. Fairley and A. Carrick. *The Casa Cookbook Pt 1.* Acolyte Science, Cheshire, 2005.

[70] D.P. Woodruff P. Bailey, T.C.Q. Noakes. *Surface Science*, 426:358–372, 1999.

[71] T. C. Q. Noakes, P. Bailey, P. K. Hucknall, K. Donovan, and M. A. Howson. Au/fe thin-film magnetic multilayer materials: A layer-specific structural analysis using medium-energy ion scattering. *PHYS. REV. B*, 58(8):4934–4941, 1998.

[72] C. B. Shoemaker, D. A. Keszler, and D. P. Shoemaker. Structure of μ-mnal$_4$ with composition close to that of quasicrystal phases. *Acta Crystallogr. B*, 45:13–20, 1989.

[73] S. L. Chang, J. W. Anderegg, and P. A. Thiel. Surface oxidation of an al-pd-mn quasicrystal, characterized by x-ray photoelectron spectroscopy. *Journal of Non-Crystalline Solids*, 195:95–101, 1996.

[74] V. Demange, J. W. Anderegg, J. Ghanbaja, F. Machizaud, D. J. Sordelet, M. Besser, P. A. Thiel, and J. M. Dubois. surface oxidation of al-cr-fe alloys by xps. *Appl. Surf. Sci.*, 173:327–338, 2001.

[75] J. A. Smerdon, J. T. Parle, R. McGrath, B. Bauer, and P. Gille. Surface study of the (100) and (010) faces of the quasicrystal approximant al4(cr,fe). *Z. Kristallogr.*, 224:13–15, 2009.

[76] J.F. Moulder, W.F. Stickle, P.E. Sobol, and K.D. Bomben. *Handbook of X-ray Photoelectron Spectroscopy.* Perkin Elmer, Eden Prairie, 1992.

[77] D.P. Woodruff C.F. McConville, D.L. Seymour and S. Bao. Synchrotron radiation core level photoemission investigation of the initial stages of oxidation of al (1 1 1). *Surface Sci.*, 188(1-2).

[78] R.Z. Bachrach A. Bianconi and S. A. Flodstrom. Oxygen chemisorption on al: Unoccupied extrinsic surface resonances and site-structure determination by surface soft-x-ray absorption. *Phys. Rev. B*, 19:38793888, 1979.

[79] G Beamson MR Alexander, GE Thompson. Characterization of the oxide/hydroxide surface of aluminium using x-ray photoelectron spectroscopy: a procedure for curve fitting the o 1s core level. *Surf. Interface Anal.*, 29:468–477, 2000.

[80] D. Mercier, J.C. Rouchaud, and M.G. Barthes-Labrousse. Interaction of amines with native aluminium oxide layers in non-aqueous environment: Application to the understanding of the formation of epoxy-amine/metal interphases. *Applied Surf. Science*, 254:6495–6503, 2008.

[81] D. Veys, P. Weisbecker, B. Domenichini, S. Weber, V. Fournee, and J. M. Dubois. Chemical surface ageing in ambient conditions of an alfecr approximant phase. *J. Phys.: Condens. Matter*, 19:376207, 2007.

[82] D. Briggs and M.P. Seah (Eds.). *Practical Surface Analysis Volume 1: Auger and X-ray Photoelectron Spectroscopy.* J Wiley, London, 1990.

[83] Y. S. Wang, P. J. Thomas, and P. OBrien. Optical properties of zno nanocrystals doped with cd, mg, mn, and fe ions. *Journ. Phys. Chem. Lett. B*, 110:21412–21415, 2006.

[84] B. Raton and R. Lide (Ed.). *Handbook of Chemistry and Physics, 78th Edition.* CRC Press, FL.

[85] T. Campbell. Dynamics of oxidation of aluminum nanoclusters using variable charge molecular-dynamics simulations on parallel computers. *Physical Review Letters*, 82:4866, 1999.

[86] G. Paglia. Determination of the structure of -alumina using empirical and first principles calculations combined with supporting experiments. *Curtin University of Technology, Perth*, 2004.

[87] R. E. Bedworth N.B. Pilling. *The Oxidation of Metals at High Temperatures.* J. Inst. Met, 1923.

[88] *ASM Handbook Vol.13 Corrosion.* ASM International, 1987.

[89] Robert W.; Flemings Merton C.; Ilschner Bernhard; Kramer Edward J.; Mahajan Subhash (Editors) Buschow, K.H. Jrgen; Cahn. *Encyclopedia of Materials - Science and Technology.* Elsevier, Oxford, UK, 2001.

[90] US Dept. of Labor. Occupational exposure to hexavalent chromium. *OSHA Federal Register*, 71:10099–10385, 2006.

[91] C. A.; Martinez M. A.; Stoner G. E. Buchheit, R. G.; Drewien. Chromate -free corrosion resistant conversion coatings for aluminum alloys, minutes of the fourth annual workshop on chromate replacements in light metal finishing. *Sandia National Laboratories Technical Report*, pages 125–7, 2006.

[92] J. Anthony. *New surface treatment for aluminum, 158(23).* Iron Age.

[93] J. Edwards. *Coating and Surface Treatment Systems for Metals.* Finishing Publications Ltd. and ASM International, 1997.

[94] B.R. Strohmeier. An esca method for determining the oxide thickness on aluminum-alloys. *Surf. Interface Anal.*, 15:51, 1990.

[95] P Gille B Bauer, B Pedersen. Al_4(cr, fe): single crystal growth by the czochralski method and structural investigation with neutrons at frm ii. *Zeitschrift fr Kristallographie*, 224:109–111, 2009.

[96] K. Momma and F. Izumi. Iucr newslett. *Commission on Crystallogr. Comput.*, No. 7:106–119, 2006.

[97] V. Fournée and P. A. Thiel. New phenomena in epitaxial growth: solid films on quasicrystalline substrates. *J. Phys. D: Appl. Phys.*, 38:R83–R106, 2004.

[98] R. McGrath, J. Ledieu, E. J. Cox, and R. D. Diehl. Quasicrystal surfaces: structure and potential as templates. *J. Phys.: Condensed Matter*, 14:R119–R144, 2002.

[99] J. A. Smerdon, L. H. Wearing, J. K. Parle, L. Leung, H. R. Sharma, J. Ledieu, and R. McGrath. Ordering of adsorbed species on quasicrystal surfaces. *Philosophical Magazine*, 88:13:2073–2082, 2008.

[100] K. J. Franke, H. R. Sharma, W. Theis, P. Gille, P. Ebert, and K. H. Rieder. Quasicrystalline epitaxial single element monolayers on icosahedral al-pd-mn and decagonal al-ni-co quasicrystal surfaces. *Phys. Rev. Lett.*, 89(15):156104, 2002.

[101] J. Ledieu, P. Unsworth, T. A. Lograsso, A. R. Ross, and R. McGrath. Ordering of si atoms on the fivefold al-pd-mn quasicrystal surface. *Phys. Rev. B*, 73:012204, 2006.

[102] J. Ledieu, L. Leung, L. H. Wearing, R. McGrath, T. A. Lograsso, D. Wu, and V. Fournée. Self-assembly, structure, and electronic properties of a quasiperiodic lead monolayer. *Phys. Rev. B.*, 77:073409, 2008.

[103] M. Krajčí and J. Hafner. Structure, stability and electronic properties of the i-alpdmn quasicrystalline surface. *Phys. Rev. B*, 71:054202, 2005.

[104] M. Krajčí and J. Hafner. Ab-inito study of a quasiperiodic bi monolayer on a fivefold i-alpdmn surface. *Phil. Mag.*, 86:825–830, 2006.

[105] R. Penrose. The role of aesthetics in pure and applied mathematical research. *Bull. Inst. Math. Appl.*, 10:266, 1974.

[106] H. Brune. Microscopic view of epitaxial metal growth: nucleation and aggregation. *Surface Science Reports*, 31:121–229, 1998.

[107] M. Krajčí and J. Hafner. Ab initio study of quasiperiodic monolayers on a fivefold i-alpdmn surface. *Phys. Rev. B*, 71:184207, 2005.

[108] M. Krajčí, J. Hafner, J. Ledieu, and R. McGrath. Surface vacancies at the fivefold icosahedral al-pd-mn quasicrystal surface: A comparison of ab initio calculated and experimental stm images. *Phys. Rev. B*, 73:024202, 2006.

[109] D. Gratias, F. Puyraimond, M. Quiquandon, and A. Katz. Atomic clusters in icosahedral f-type quasicrystals. *Phys. Rev. B*, 63:024202, 2000.

[110] M. Baake, P. Kramer, M. Schlottmann, and D. Zeidler. Planar patterns with fivefold symmetry as sections of periodic structures in 4-space. *Int. J. Mod. Phys.*, B4:2217–2268, 1990.

[111] T. Cai, J. Ledieu, R. McGrath, V. Fournée, T. Lograsso, A. Ross, and P. Thiel. Pseudomorphic starfish: nucleation of extrinsic metal atoms on a quasicrystalline substrate. *Surf. Sci.*, 526(1-2):115–120, 2003.

[112] J. Ledieu, C. A. Muryn, G. Thornton, R. D. Diehl, T. A. Lograsso, D. W. Delaney, and R. McGrath. C60 adsorption on the quasicrystalline surface of al70pd21mn9. *Surf. Sci.*, 472(1-2):89–96, 2001.

[113] J. A. Smerdon, J. K. Parle, L. H. Wearing, T. A. Lograsso, A. R. Ross, and R. McGrath. Nucleation and growth of a quasicrystalline monolayer: Bi adsorption on the ve-fold surface of *i*-al-pd-mn. *Phys. Rev. B*, 78:075407, 2008.

[114] R. A. Laudise. *The Growth of Single Crystals.* Solid State Physical Electronics Series. Prentice-Hall, Hemel Hempstead, 1970.

[115] R.M. Tromp J.F. Frenken, J.F. van der Veen. *Nuclear Instruments and Methods in Physics Research B*, 17:334, 1986.

[116] T. C. Q. Noakes, P. Bailey, C. F. McConville, C. R. Parkinson, M. Draxler, J.A. Smerdon, J. Ledieu, R. McGrath, A. R. Ross, and T. A. Lograsso. Compositional and structural changes in *i*-alpdmn quasicrystals induced by sputtering and annealing: A medium energy ion scattering study. *Surf. Sci.*, 583:139–150, 2005.

[117] N. R. Shivaparan, V. Krasemann, V. Shutthanandan, and R. J. Smith. Room temperature growth of thin fe films on al(0 0 1) and al(1 1 0) surfaces. *Surface Science*, 365:78–86, 1996.

[118] J Smerdon, J Ledieu, J.T. Hoeft, D.E. Reid, L.H. Wearing, R.D. Diehl, T.A. Lograsso, A.R. Ross, and R. McGrath. Adsorption of cobalt on the five-fold surface of alpdmn and the 10-fold surface of al-ni-co. *Philos. Mag.*, 86:841–848, 2006.

[119] J. Ledieu, J. T. Hoeft, D. Reid, J. Smerdon, R. D. Diehl, T. A. Lograsso, A. R. Ross, and R. McGrath. Pseudomorphic growth of a quasiperiodic copper thin film on a quasicrystal surface. *Phys. Rev. Lett.*, 92:135507, 2004.

[120] J. Ledieu, J. T. Hoeft, D. Reid, J. Smerdon, R. D. Diehl, T. A. Lograsso, A. R. Ross, and R. McGrath. Copper adsorption on the five-fold alpdmn surface. *Phys. Rev. B*, 72:035420, 2005.

[121] J. A. Smerdon, J. Ledieu, R. McGrath, T. C. Q. Noakes, P. Bailey, M. Drexler, C. F. McConville, T. A. Lograsso, and A. R. Ross. Characterization of aperiodic and periodic thin cu films formed on the five-fold surface of $i\text{-}al_{70}pd_{21}mn_9$ using medium-energy ion scattering spectroscopy. *Phys. Rev. B*, 74:035429, 2006.